

AD-A275 249

2



93-1171

①

CSDL-T-1180

**LUNAR GRAVITATIONAL FIELD ESTIMATION  
AND THE EFFECTS OF MISMODELING  
UPON LUNAR SATELLITE ORBIT PREDICTION**

by

John H. Davis

June 1993

Master of Science Thesis  
Massachusetts Institute of Technology

DTIC  
ELECTE  
FEB 2 1994  
S C D

Approved for public release;  
distribution unlimited.

NASA-JSC 8/24/93

94 2 01 1 6



160PG

94-03345



The Charles Stark Draper Laboratory, Inc.  
555 Technology Square, Cambridge, Massachusetts 02139-3563

# LUNAR GRAVITATIONAL FIELD ESTIMATION AND THE EFFECTS OF MISMODELING UPON LUNAR SATELLITE ORBIT PREDICTION

by

JOHN H. DAVIS

S.B., Aeronautics and Astronautics, Massachusetts Institute of Technology  
Cambridge, Massachusetts (1987)

Submitted to the Department of Aeronautics and Astronautics  
in Partial Fulfillment of the Requirements for the Degree of

MASTER OF SCIENCE in AERONAUTICS AND ASTRONAUTICS

at the

MASSACHUSETTS INSTITUTE OF TECHNOLOGY

June 1993

© John H. Davis, 1993. All Rights Reserved

Signature of Author

*John H. Davis*

Department of Aeronautics and Astronautics  
7 May 1993

Certified by

*Michael E. Ash*

Dr. Michael E. Ash  
Principal Member Technical Staff, The Charles Stark Draper Laboratory, Inc.  
Thesis Supervisor

Certified by

*Richard H. Battin*

Professor Richard H. Battin  
Department of Aeronautics and Astronautics  
Thesis Advisor

Accepted by

*Harold Y. Wachman*

Professor Harold Y. Wachman  
Chairman, Department Graduate Committee

Accession For	
NTIS CRA&I	<input checked="checked" type="checkbox"/>
DTIC TAB	<input type="checkbox"/>
Unannounced	<input type="checkbox"/>
Justification	
By	
Distribution /	
Availability Codes	
Dist	Avail and / or Special
A1	

DTIC QUALITY INSPECTED 2



# REPORT DOCUMENTATION PAGE

Form Approved  
OMB No. 0704-0188

Public reporting burden for this collection of information is estimated to average 1 hour per response, including the time for reviewing instructions, searching existing data sources, gathering and maintaining the data needed, and completing and reviewing the collection of information. Send comments regarding this burden estimate or any other aspect of this collection of information, including suggestions for reducing the burden, to Washington Headquarters Services, Directorate for Information Operations and Reports, 1215 Jefferson Davis Highway, Suite 1204, Arlington, VA 22202-4302, and to the Office of Management and Budget, Paperwork Reduction Project (0704-0188), Washington, DC 20503.

1. AGENCY USE ONLY (Leave blank)

2. REPORT DATE

Jun 1993

3. REPORT TYPE AND DATES COVERED

THESIS/DISSERTATION

4. TITLE AND SUBTITLE

Lunar Gravitational Field Estimation and the effects of mis modeling upon Lunar Satellite Orbit Prediction

5. FUNDING NUMBERS

6. AUTHOR(S)

John H. DAVIS

7. PERFORMING ORGANIZATION NAME(S) AND ADDRESS(ES)

AFIT Student Attending: Mass Inst of Tech

8. PERFORMING ORGANIZATION REPORT NUMBER

AFIT/CI/CIA-

93-1171

9. SPONSORING/MONITORING AGENCY NAME(S) AND ADDRESS(ES)

DEPARTMENT OF THE AIR FORCE  
AFIT/CI  
2950 P STREET  
WRIGHT-PATTERSON AFB OH 45433-7765

10. SPONSORING/MONITORING AGENCY REPORT NUMBER

11. SUPPLEMENTARY NOTES

12a. DISTRIBUTION/AVAILABILITY STATEMENT

Approved for Public Release IAW 190-1  
Distribution Unlimited  
MICHAEL M. BRICKER, SMSgt, USAF  
Chief Administration

12b. DISTRIBUTION CODE

13. ABSTRACT (Maximum 200 words)

14. SUBJECT TERMS

15. NUMBER OF PAGES

171

16. PRICE CODE

17. SECURITY CLASSIFICATION OF REPORT

18. SECURITY CLASSIFICATION OF THIS PAGE

19. SECURITY CLASSIFICATION OF ABSTRACT

20. LIMITATION OF ABSTRACT

# **LUNAR GRAVITATIONAL FIELD ESTIMATION AND THE EFFECTS OF MISMODELING UPON LUNAR SATELLITE ORBIT PREDICTION**

by

**JOHN H. DAVIS**

Submitted to the Department of Aeronautics and Astronautics  
on May 7, 1993

in partial fulfillment of the requirements for the degree of  
Master of Science in Aeronautics and Astronautics

## **ABSTRACT**

Lunar spherical harmonic gravity coefficients are estimated from simulated observations of a near-circular low altitude polar orbiter disturbed by lunar mascons. Lunar gravity sensing missions using earth-based near-side observations with and without satellite-based far-side observations are simulated and least squares maximum likelihood estimates are developed for spherical harmonic expansion fit models. Simulations and parameter estimations are performed by a modified version of the Smithsonian Astrophysical Observatory's Planetary Ephemeris Program.

Two different lunar spacecraft mission phases are simulated to evaluate the estimated fit models. Results for predicting state covariances one orbit ahead are presented along with the state errors resulting from the mismodeled gravity field. The position errors from planning a lunar landing maneuver with a mismodeled gravity field are also presented. These simulations clearly demonstrate the need to include observations of satellite motion over the far side in estimating the lunar gravity field. The simulations also illustrate that the eighth degree and order expansions used in the simulated fits were unable to adequately model lunar mascons.

Thesis Supervisor: Dr. Michael E. Ash  
Principal Member Technical Staff  
The Charles Stark Draper Laboratory, Inc.

Thesis Advisor: Professor Richard H. Battin  
Adjunct Professor of Aeronautics and Astronautics



## Acknowledgements

Primary thanks go to Dr. Michael E. Ash for indoctrinating me into the capabilities of the Planetary Ephemeris Program and for helping me with this research. Secondly, I would like to thank Professor Battin for sharing his enthusiasm for astrodynamics and its history, as well as for instructing me in the mathematics involved. In addition, I would like to thank Tim Brand for helping to define and fund this project and for helping me to 'stay the course.' I would also like to thank Stan Sheppard for reviewing the manuscript, furnishing excellent critiques, and offering timely words of encouragement.

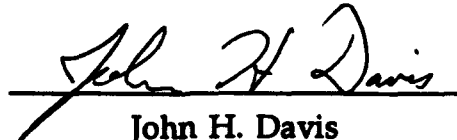
Additionally, I would like to thank the U.S. Air Force for providing me the opportunity to return to M.I.T. and the Draper Laboratory for making it possible. From the lab, Ken Spratlin and Tony Bogner's patience and assistance with the Sun network helped me get through some very long and memory-intensive computer runs. I would also like to thank all of the other Draper Fellows who have helped in one way or another, and have made the experience enjoyable: Matt, Debbie, Tony, Brad, Marc, Lisa, Jeff, Wendy, and the rest of the gang waiting for a Sun to become available.

More thanks go out to my family for their support through all my endeavours. I would like to express my gratitude to my mother for being the "wind beneath my wings" for so long. A special thanks to my brother Bill for bringing me back to earth when I'm dreaming of space. Last, first, and throughout, for having the confidence I sometimes lacked, for offering encouragement, and for being my partner on an even bigger challenge, I would like to especially thank my loving and understanding wife, PAM.

**This thesis was researched and written at the Charles Stark Draper Laboratory under NASA Contract NAS9 - 18426.**

**Publication of this thesis does not constitute approval by the Charles Stark Draper Laboratory, the United States Air Force, or the National Aeronautics and Space Administration of the findings or conclusions contained herein. It is published for the exchange and stimulation of ideas.**

**I hereby assign my copyright of this thesis to the Charles Stark Draper Laboratory, Inc., of Cambridge, Massachusetts.**

A handwritten signature in cursive script, reading "John H. Davis", is written over a horizontal line.

**John H. Davis**

**May 7, 1993**

**Permission is hereby granted by the Charles Stark Draper Laboratory, Inc. to the Massachusetts Institute of Technology to reproduce and to distribute copies of this thesis document in whole or in part.**



# Table of Contents

<b>Abstract.....</b>	<b>3</b>
<b>Acknowledgements.....</b>	<b>5</b>
<b>Table of Contents .....</b>	<b>7</b>
<b>List of Illustrations.....</b>	<b>12</b>
<b>List of Tables.....</b>	<b>13</b>
<b>List of Symbols.....</b>	<b>15</b>
<b>Chapter One Introduction and Summary.....</b>	<b>19</b>
1.1 Background .....	19
1.2 Motivation .....	20
1.3 Initial Lunar Gravitational Sensing Method.....	22
1.4 Proposed Lunar Gravitational Sensing Methods .....	23
1.5 Simulation Tools.....	26
1.6 Methodology.....	27
1.7 Summary of Results.....	29

<b>Chapter Two Gravity Field Models.....</b>	<b>31</b>
2.1 LaPlace's Equation and the External Gravitational Field.....	31
2.2 Spherical Harmonic Expansion for the Gravitational Potential.....	33
2.2.1 Relation between Spherical Harmonics and Moments of Inertia.....	37
2.2.2 Limitations of the Spherical Harmonic Expansion.....	38
2.3 Localized Surface-Layer Gravitational Field Models .....	40
2.3.1 Point Mass Model .....	40
2.3.2 Surface Disk Model.....	41
2.3.3 Gravity Dipole Model .....	43
<b>Chapter Three Orbit Propagation .....</b>	<b>45</b>
3.1 Numerical Integration Techniques .....	45
3.2 Units and Coordinate Systems.....	47
3.3 Equations of Satellite Motion.....	49
3.3.1 Effect of Lunar Gravitational Harmonics.....	50
3.3.2 Effect of Other Gravitational Body Harmonics .....	51
3.3.3 Effect of Mass Concentrations .....	52
3.4 Partial Derivatives of the Satellite Motion Differential Equation.....	53
3.4.1 Effect of Lunar Spherical Harmonics on the Partial Derivatives.....	54
3.4.2 Effect of Earth Spherical Harmonics on the Partial Derivatives.....	58
3.4.3 Effect of Mass Concentrations upon the Partial Derivatives.....	59
3.4.4 Effects of Initial Conditions on the Partial Derivatives.....	59
3.4.5 Checking Partial Derivatives by the Difference Method.....	60

<b>Chapter Four Satellite Observations.....</b>	<b>61</b>
4.1 Observation Simulation and Processing .....	61
4.2 Observation Methods.....	63
4.2.1 Earth-Based Observations .....	64
4.2.2 Satellite-Based Observations .....	64
4.2.3 Bent Pipe Observations.....	65
4.2.4 Observation Interruptions.....	66
4.3 Observation Types .....	67
4.3.1 Azimuth-Elevation Observations.....	67
4.3.2 Right Ascension-Declination Observations.....	69
4.3.3 Meridian Crossing-Elevation Angle Observations .....	70
4.3.4 Satellite Look Angle Observations.....	71
4.3.5 Interferometry Observations.....	72
4.3.6 Range Observations.....	73
4.3.7 Range Rate Observations .....	74
4.4 Partial Derivatives of Satellite Observations.....	76
<b>Chapter Five Parameter Estimation and Prediction of Uncertainty.....</b>	<b>79</b>
5.1 Parameter Estimation .....	79
5.1.1 Observation Vector as a Random Variable.....	79
5.1.2 Maximum Likelihood Estimation.....	81
5.1.3 Weighted Least Squares Estimation .....	83
5.1.4 Choice of Estimation Method .....	84
5.1.5 Incorporation of A Priori Information .....	85
5.1.6 Solution to the Normal Equations .....	86
5.1.7 Other Estimation Techniques .....	87
5.2 Statistical Prediction of Uncertainty .....	88
5.3 Prediction Uncertainty Due to Mismodeling.....	92

<b>Chapter Six Orbit Fitting and Gravity Estimation .....</b>	<b>93</b>
6.1 Methodology .....	93
6.2 Fifth Degree Harmonic Truth and Fit Model Test Case.....	95
6.2.1 Scenario One: No Occultation, Range and Range Rate .....	99
6.2.2 Scenario Two: No Occultation, Range Rate.....	100
6.2.3 Scenario Three: Occultation, Range and Range Rate..	100
6.2.4 Scenario Four: Occultation, Range Rate .....	101
6.2.5 Scenario Five: Occultation, Range and Range Rate with Biases.....	101
6.3 Earth-Based Doppler Observable Mascon Test Cases .....	101
6.3.1 Scenario One: Limb Mascons .....	103
6.3.2 Scenario Two: Face Mascons .....	104
6.4 Truth Model Development.....	105
6.5 Single Orbiter, Earth-Based Doppler Sensing Scheme.....	108
6.5.1 Single Orbiter "Truth" Model Observations.....	108
6.5.2 Eighth Degree and Order Fit.....	109
6.5.3 Twelfth Degree and Order Fit.....	110
6.6 Tenth Degree Harmonic Truth and Fit Model Test Case.....	112
6.7 Dual Orbiter, Bent Pipe Doppler Sensing Scheme.....	114
6.7.1 Dual Orbiter "Truth" Model Observations .....	116
6.7.2 Eighth Degree and Order Fit.....	116
<b>Chapter Seven Lunar Gravity Field Estimation Analyses.....</b>	<b>121</b>
7.1 Analysis Techniques .....	121
7.2 Global Lunar Radial Acceleration Analysis.....	122
7.2.1 Limb / Face Mascon Analysis.....	123
7.2.2 Analysis of the Eighth Degree and Order Fits.....	124

7.3 Single Orbit State Uncertainty Prediction Analysis.....	124
7.3.1 State Uncertainty Prediction.....	126
7.3.2 State Errors Between "True" and Estimated Gravity Models.....	127
7.4 Lunar Deorbit Maneuver Error Analysis .....	132
7.5 Gravity Coefficient Parameter Correlation Analysis .....	135
 Chapter Eight Conclusions .....	 141
8.1 Summary of Results.....	141
8.2 Recommendations for Future Research.....	145
 Appendix A Evaluation of Legendre Polynomials and Normalized Legendre Functions.....	 147
A.1 Legendre Polynomials.....	147
A.2 Normalized Legendre Functions.....	148
 Appendix B List of Constants.....	 151
 Appendix C Inertial Coordinate Transformations.....	 153
C.1 Transformation Between Moon Fixed and Inertial Frames.....	153
C.2 Transformation Between Earth Fixed and Inertial Frames.....	156
 Appendix D Lunar Gravitational "Truth" Model.....	 159
 Appendix E Tables of Spherical Harmonic Coefficients.....	 163
 References.....	 169

## List of Illustrations

Figure	Page
1.3-1 Lunar Orbiter Earth-Moon Geometry .....	22
1.4-1 Dual Orbiter Sensing Method .....	24
1.4-2 Co-orbital Sensing Method.....	25
2.1-1 Distributed Mass acting upon a Point Mass $m$ .....	32
2.2-1 Spherical Coordinate System .....	34
2.2.2-1 Zonal, Tesseral, and Sectorial Harmonic Patterns.....	38
2.3.2-1 Prolate and Oblate Spheroids .....	42
2.3.3-1 Surface Gravity Dipole.....	44
4.3.1-1 Azimuth-Elevation Angle Vectors in the Meridian Plane....	68
4.3.1-2 Azimuth-Elevation Angles and the Tangent Plane.....	68
4.3.2-1 Right Ascension and Declination Angles .....	70
4.3.3-1 Elevation Angle at Meridian Crossing.....	70
4.3.4-1 Satellite-Based Look Angles .....	71
4.3.5-1 Long Baseline Interferometry Measurement Geometry.....	72
4.3.6-1 Simulated Two-Way Ranging Measurement.....	74
4.3.7-1 Waves Radiated from a Stationary and Moving Source .....	75
6.1-1 Flow Diagram for Gravity Sensing Mission Simulations .....	94
7.3.1-1 Single Orbiter Estimated Gravity Field State Uncertainties ....	128
7.3.1-2 Dual Orbiter Estimated Gravity Field State Uncertainties.....	129
7.3.2-1 Single Orbiter Estimated Gravity Field State Errors.....	130
7.3.2-2 Dual Orbiter Estimated Gravity Field State Errors.....	131
7.4-1 Lunar Deorbit Mission.....	133
7.5-1 Parameter Correlation Distributions for Several Observation Methods.....	138
7.5-2 Tesseral 8,6 and Sectorial 6,6 Zero Line Patterns.....	139

## List of Tables

Table	Page
2.2.2-1 Spherical Harmonic and Surface Mass Density Surface Resolution Comparison.....	39
6.2-1 Satellite Initial Conditions for 5 x 5 Spherical Harmonic Test Case.....	96
6.2-2 5 x 5 Spherical Harmonic Truth Model Coefficients.....	97
6.2-3 Perturbed Satellite Initial Conditions for Estimation Model..	98
6.3-1 Mascon Test Case - Mascon Placement.....	102
6.3.1-1 Limb Mascon Orbital Initial Condition Estimates.....	104
6.3.2-1 Face Mascon Orbital Initial Condition Estimates.....	105
6.4-1 "Truth" Model Major Mass Anomalies .....	107
6.5.1-1 Satellite Initial Conditions for "Truth" Model Observations	109
6.5.2-1 8 x 8 Single Orbiter Initial Condition Estimates.....	110
6.5.3-1 12 x 12 Fit Initial Guesses for Satellite Initial Conditions .....	111
6.5.3-2 12 x 12 Spherical Harmonic Fit Progression.....	111
6.6-1 10 x 10 Spherical Harmonic Fit Progression.....	113
6.7-1 Elliptical Satellite Initial Conditions for "Truth" Model Observations .....	115
6.7.2-1 8 x 8 Spherical Harmonic Fit Progression,.....	117
6.7.2-2 Circular Orbiter Initial Condition Estimates.....	118
6.7.2-3 Elliptical Orbiter Initial Condition Estimates .....	119
7.3-1 Low Inclination, Low Altitude Evaluation Orbit .....	125
7.4-1 Low Inclination, Lunar Landing Parking Orbit.....	134
D-1 5 x 5 Spherical Harmonic Coefficient Portion of Truth Model [12].....	159
D-2 Lunar Near-Side Mascons at 1638 km Radius [47].....	160
D-3 Lunar Far-Side Mascons at 1638 km Radius .....	161

<b>Table</b>	<b>Page</b>
E-1 Limb Mascon Fit Model Coefficients.....	164
E-2 Face Mascon Fit Model Coefficients.....	165
E-3 8 x 8 Single Orbiter Earth-based Doppler Fit Model Coefficients.....	166
E-4 Additional Coefficients for the 10 x 10 Spherical Harmonic Expansion [27] .....	167
E-5 8 x 8 Dual Orbiter Bent Pipe Doppler Fit Model Coefficients..	168



## List of Symbols

$a$	=	semi-major axis
$c$	=	speed of light
$d$	=	separation distance, gravity dipoles or observation sites
$\bar{D}$	=	gravity dipole strength
$e$	=	eccentricity ( $0 \leq e < 1$ )
$f$	=	frequency
$H_i$	=	effect of harmonics in the gravitational field of body $i$
$i$	=	inclination
$K$	=	effect of mass concentrations
$M_0$	=	initial mean anomaly
$M_i$	=	mass of body $i$
$\hat{n}$	=	unit normal to a surface
$N_i$	=	upper limit of quantity $i$ in a series expansion
$O$	=	higher order terms
$p(\bar{z}; \bar{\alpha})$	=	probability density of $\bar{z}$ as a function of the parameters $\bar{\alpha}$ .
$\hat{p}$	=	unit vector in pitch axis or pole of central body
$p$	=	probability density, likelihood function
$\bar{q}$	=	observation signal path, line-of-sight
$q$	=	rational transponder frequency translation
$Q$	=	scalar cost function
$r_i$	=	radius of mascon or site $i$
$r_{ij}$	=	distance between body $i$ and $j$
$\hat{r}$	=	unit vector in the roll axis
$R_{ij}$	=	rotation transformation matrix from $j$ frame to $i$ frame
$R_i$	=	column vector of the rotation transformation matrix
$R$	=	range observable
$\dot{R}$	=	range rate observable
$T_i$	=	tesseral series expansion in partial derivatives of motion
$U$	=	gravitational potential

$\bar{U}$	=	position vector in selenographic Cartesian coordinates
$\bar{X}^*$	=	augmented state vector in inertial Cartesian coordinates
$\bar{X}_{ij}$	=	position vector of body i relative to body j (inertial coord.)
$\dot{\bar{X}}$	=	velocity vector in inertial coordinates
$\hat{y}$	=	unit vector in the yaw axis
$\bar{z}$	=	measurement vector
$Z$	=	zonal series expansion in partial derivatives of motion
$\bar{\alpha}$	=	vector of estimation parameters (orbital initial conditions, gravitational harmonic coefficients, ...)
$\bar{\alpha}_0$	=	vector of initial guesses of parameters $\bar{\alpha}$
$\Delta\bar{\alpha}$	=	vector of adjustment to the parameters $\bar{\alpha}$
$\bar{\alpha}$	=	estimate of parameter $\alpha$ , a priori estimate
$\hat{\bar{\alpha}}$	=	maximum likelihood estimate of the parameters $\bar{\alpha}$
$\bar{\beta}$	=	measurement biases, parameters affecting an observation
$\epsilon_0$	=	obliquity of the ecliptic
$\epsilon_{ij}$	=	correlation between $i^{\text{th}}$ and $j^{\text{th}}$ elements of $\hat{\bar{\alpha}}$
$\zeta$	=	generalized third Cartesian coordinate, negative log-likelihood function
$\eta$	=	generalized second Cartesian coordinate
$\theta_i$	=	east longitude of site or mascon i
$\bar{\theta}$	=	measurement error vector
$\Theta$	=	covariance matrix of measurement error vector
$\mu$	=	expected value, mean
$\xi$	=	generalized first Cartesian coordinate
$\Xi$	=	covariance matrix of satellite state
$\sigma_i$	=	standard deviation of $i^{\text{th}}$ element in $\Theta$ or $\Sigma$
$\Sigma$	=	covariance matrix of estimated parameters
$\tilde{\Sigma}$	=	covariance matrix of a priori parameter estimates
$v$	=	mass fraction of all mascons to lunar mass
$\phi_i$	=	latitude, regular or geodetic, of site or mascon i
$\chi$	=	distance ratio between the lunar maximum radius and the lunar satellite radius
$\Psi_i$	=	effect of central body attractions of body i
$\omega$	=	argument of perilune
$\Omega$	=	right ascension of the ascending node

### ***Operators***

$E\{\}$	=	expectation operator
$\exp[]$	=	exponential operator
$\ln[]$	=	natural logarithm operator
$\text{unit}[]$	=	unit magnitude operator on vector
$  $	=	determinant of a matrix, magnitude of a vector
$\bullet$	=	dot product operator
$\times$	=	cross product operator

### ***Subscripts***

$b$	=	lunar satellite
$c$	=	earth-moon barycenter
$c.m.$	=	center of mass
$CT$	=	cross track direction
$DR$	=	down range direction
$e$	=	earth
$g$	=	gravitational parameters
$I$	=	inertial frame
$k$	=	mascon
$l$	=	moon
$L$	=	local vertical, local horizontal frame
$m$	=	order (Legendre functions and tesseral coefficients)
$n$	=	degree (Legendre functions and harmonic coefficients)
$p$	=	planet
$r$	=	receive time
$r.s.$	=	receiving site
$s$	=	sun, source (signal), or send time
$s.s.$	=	sending site
$t$	=	tesseral harmonics, or transpond/reflection time
$t.s.$	=	transponding or reflection site
$VT$	=	vertical direction
$z$	=	zonal harmonics
$0$	=	initial time
$i$	=	$i^{\text{th}}$ element of a vector, $i^{\text{th}}$ column vector of a matrix
$ij$	=	$ij^{\text{th}}$ element of a matrix

### ***Superscripts***

<b>R</b>	=	<b>position</b>
<b>T</b>	=	<b>transpose operator</b>
<b>V</b>	=	<b>velocity</b>
<b>-1</b>	=	<b>inverse</b>
<b>-</b>	=	<b>vector</b>
<b>^</b>	=	<b>vector of unit length</b>
<b>-</b>	=	<b>normalized harmonic coefficient</b>
<b>.</b>	=	<b>first derivative with respect to time</b>
<b>'</b>	=	<b>first derivative with respect to an argument</b>
<b>"</b>	=	<b>second derivative with respect to an argument</b>

### ***Acronyms***

<b>CT</b>	=	<b>Coordinate Time</b>
<b>DSN</b>	=	<b>Deep Space Network</b>
<b>GPS</b>	=	<b>Global Positioning System</b>
<b>GSFC</b>	=	<b>Goddard Space Flight Center</b>
<b>IAU</b>	=	<b>International Astronomical Union</b>
<b>JD</b>	=	<b>Julian Date</b>
<b>JPL</b>	=	<b>Jet Propulsion Laboratory</b>
<b>NASA</b>	=	<b>National Aeronautics and Space Administration</b>
<b>PDI</b>	=	<b>Powered Descent Initiation</b>
<b>PEP</b>	=	<b>Planetary Ephemeris Program</b>
<b>PEP-D</b>	=	<b>Draper modified Planetary Ephemeris Program</b>
<b>rms</b>	=	<b>root mean square (square root of the mean of squared values)</b>
<b>rss</b>	=	<b>root sum square (square root of the sum of squared values)</b>
<b>SAO</b>	=	<b>Smithsonian Astrophysical Observatory</b>
<b>UTC</b>	=	<b>Universal Coordinated Time (Universal Temps Coordinée from the Bureau International de l'Heure in France)</b>

## **Chapter One**

# **Introduction and Summary**

### **1.1 Background**

On July 20, 1989, the 20<sup>th</sup> anniversary of the first Apollo moon landing, President George Bush challenged the nation to undertake an ambitious course of human space exploration. After establishing a manned presence in earth orbit with the Space Station Freedom in the 1990's, the President proposed that the U.S. return to the moon, and return to stay. From this lunar basing point, the U.S. could continue human exploration of our solar system by undertaking a manned mission to Mars.

The establishment of a lunar base will result in significant lunar traffic to build, supply, and resupply this facility. This increased traffic will require a lunar navigation system. As the nation prepares its return to the moon, it will have to decide whether this navigation system should be earth-based, vehicle-based or lunar-based.

Our initial voyages to the moon primarily depended upon earth-based navigation systems, although the manned missions had some on-board capability. An earth-based method could be adopted for future lunar travel, but NASA's Deep Space Network (DSN) tracking is manpower intensive, costly, and is not suitable for high traffic rates. Additionally, earth-based navigation can only track vehicles on the lunar near side. Adopting an earth-based navigation system would be an impractical stepping stone for human exploration of Mars and the solar system.

A vehicle-based navigation system could be developed to support future lunar traffic. Vehicle-based navigation has become practical because of

advances in inertial navigation equipment and on-board computing capabilities. Inertial navigation would be limited by our knowledge of the cis-lunar environment, principally our knowledge of the moon's gravity field.

The limitations of earth-based navigation and the high accuracy requirements of certain mission phases (principally landing) may require the development of a lunar-based navigation system. A simple lunar navigation system similar to the earth's Global Positioning System (GPS) would handle high traffic rates and would provide accurate lunar far-side navigation. If high lunar traffic rates are achieved, then a lunar-based system could provide a higher accuracy system alternative to vehicle-based navigation.

Many low-altitude mission phases will require accurate knowledge of the moon's gravitational field, especially its far-side characteristics. Spherical harmonic models are typically used to model the gravitational field near celestial bodies. Finite expansion spherical harmonic models, however, do not accurately model the low altitude gravity field of the moon. This is because the moon's gravitational field contains significant anomalies, discovered in the late 1960's by scientists at NASA's Jet Propulsion Laboratory (JPL) [35], making such models inefficient. From earth-based lunar tracking data, the scientists developed a lunar gravity model. This model was then compared to topographical images of the moon and revealed mass concentrations around the ringed maria. These mass concentrations or "mascons" exhibit very high frequency gravitational behavior and therefore require a very high number of terms in the spherical harmonic expansion to model this behavior. Since their discovery, scientists have postulated different models to account for the lunar mascon phenomenon, since expanding the spherical harmonic model to high degree and order was computationally impractical. Chapter Two surveys the spherical harmonic and several other gravitational field modeling techniques in more detail.

### **1.2 Motivation**

Since the real lunar gravitational field is difficult to accurately model, this thesis will study the implications of modeling errors. An inaccurate model of the lunar gravity field will result in the growth of navigation errors.

Mismodeled acceleration forces result in both velocity and position errors. Since gravitational acceleration is a function of position, position errors will lead to increased acceleration errors, further increasing the velocity and position errors. This error propagation may or may not be critical depending upon the magnitude of the errors, the navigation system's ability to measure them, and the mission phase accuracy requirements.

Specifically, an inaccurate gravity model will significantly affect any landing maneuvers with strict accuracy requirements. Unmanned cargo missions to resupply a lunar base will be particularly vulnerable to errors from a mismodeled gravity field. Since there is no appreciable lunar atmosphere, gravity forces dominate a vehicle's descent to the moon's surface. Since the force of gravity is inversely proportional to the square of distance, navigation errors due to a mismodeled gravity field increase as the vehicle descends to the surface. Avoiding unacceptable landing errors will depend upon an accurate determination of the lunar gravity field.

The scientific community is also interested in developing a more precise model of the lunar gravity field. A better model can improve knowledge of the moon's composition and internal structure. Models of different elements, their densities, and their distribution within the moon's interior could be developed to match the observed gravitational field. Gravitational models may also help to determine the selenological thermal and tectonic history. The discovery of lunar mascons has also led to scientific speculation about how mass concentrations formed in these shallow seas. The scientific community hopes that a better understanding of the gravitational field around the ringed maria and other lunar surface features will help to determine the origin of these features [2, 35].

The purpose of this thesis is to determine the feasibility of using a spherical harmonic lunar gravitational model, based on observations of a near-circular polar satellite, to predict low altitude lunar orbits globally. Rather than attempting to develop a more precise lunar gravitational field model, this thesis investigates measurement types and satellite orbits that can be used to develop gravity field models. Each measurement type will have advantages and disadvantages in terms of cost, schedule, and accuracy. This thesis investigates each different method's ability to estimate a lunar

gravitational potential model and the model's accuracy in predicting future lunar orbits. By analyzing the capabilities of different sensing methods, this investigation will allow NASA to plan unmanned lunar precursor missions to extract the best lunar gravity field information.

### **1.3 Initial Lunar Gravitational Sensing Method**

Current lunar gravitation field models are based upon earth-based tracking data from the Lunar Orbiter program of the 1960's (Figure 1.3-1). These unmanned Apollo precursor missions provided photographic imaging and gravitational mapping of the moon. Apollo lunar navigation was based upon Lunar Orbiter's gravity field mapping. In addition to the Lunar Orbiter missions, tracking data from Apollo missions and some Soviet lunar missions are included in current gravity field models [3, 12, 19, 33, 41, 47].

Lunar Orbiter gravitational mapping missions utilized Doppler measurements of radio tracking signals. Lunar Orbiter spacecraft were tracked by NASA's Deep Space Network (DSN) across the near side of the moon [36]. A DSN tracking station sent a continuous wave S-Band frequency to the spacecraft. The spacecraft received this Doppler-shifted signal and re-transmitted it to earth. The tracking station received this signal, Doppler-shifted once again in frequency. The tracking station used this signal to calculate the relative velocity between the spacecraft and tracking station. The relative velocity observed was then combined with position tracking data to estimate the lunar gravity field using methods similar to those discussed in Chapter Five.

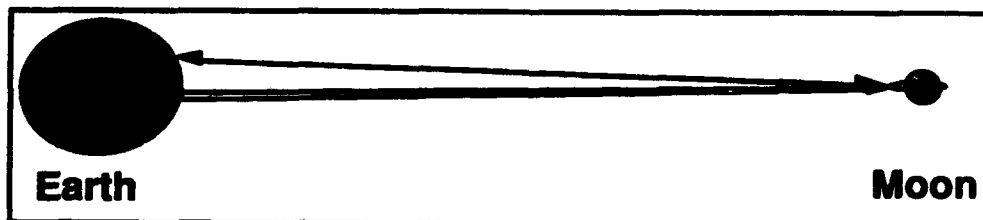


Figure 1.3-1: Lunar Orbiter Earth-Moon Geometry

Current lunar gravitation field model accuracy is limited by the amount of lunar orbital tracking data available. The Lunar Orbiter and Apollo missions were mostly low inclination missions. Since most missions



flew about the lunar equator, derived gravity field models emphasize the effects of anomalies near the equator. Only a fraction of the moon's surface was covered by these missions [32], and therefore gravity field data is lacking for lunar polar regions. Additionally, this earth-based gravity mapping method was limited to observations of near-side lunar spacecraft passes. Gravitational disturbances on the far side were only determined by their integrated effects on satellite position and velocity from the end of one near-side pass to the beginning of the next pass. Thus current lunar gravitational field models do not provide very meaningful information about the lunar far side.

#### **1.4 Proposed Lunar Gravitational Sensing Methods**

Any future lunar gravitational field sensing system will have to greatly improve our knowledge of the moon's gravitational field to justify the mission's cost. To achieve this improvement in accuracy, the system will have to address the current model's limitations. The motion of an orbiting body should be sensed without any orbital maneuvering which disturbs the estimation solution.<sup>1</sup> Thus it is desirable to select orbits which are stable for at least one lunar orbit to avoid re-boost maneuvering. A high inclination, preferably polar, lunar orbiter would allow observations of satellite accelerations over the moon's entire surface as the moon rotates under the orbital plane. A dual orbiter sensing scheme would be better because it would allow lunar far-side accelerations to be observed. Better still would be a sensing scheme observing the motion of several satellites in different inclinations than those available in Apollo-era lunar missions.

NASA is considering two different sensing schemes. NASA's Jet Propulsion Laboratory has proposed a dual orbiter scheme which uses radio-based Doppler observations to sense the moon's gravitational field effects [40]. NASA's Goddard Space Flight Center has proposed a co-orbital scheme which

---

<sup>1</sup> Gravitational accelerations experienced by an orbiter are not measured directly. Methods to measure the accelerations due to gravity therefore use external observations of a body's motion.

## LUNAR GRAVITATIONAL FIELD ESTIMATION AND SATELLITE ORBIT PREDICTION

uses a laser-based system which makes both ranging and Doppler observations [2].

The dual orbiter sensing scheme uses a low altitude, circular polar satellite and a high apolune polar elliptical satellite (Figure 1.4-1). The elliptical satellite orbit is positioned so that apolune initially occurs on the far side of the moon. This increases the duration of lunar far-side viewing. The orbit is also skewed such that apolune is outside of the earth occultation zone which increases the time that the elliptical satellite is within the line of sight of earth tracking stations. From these orbits the relative velocity between the two spacecraft can be measured using either the bent pipe or the satellite bounce methods described below.

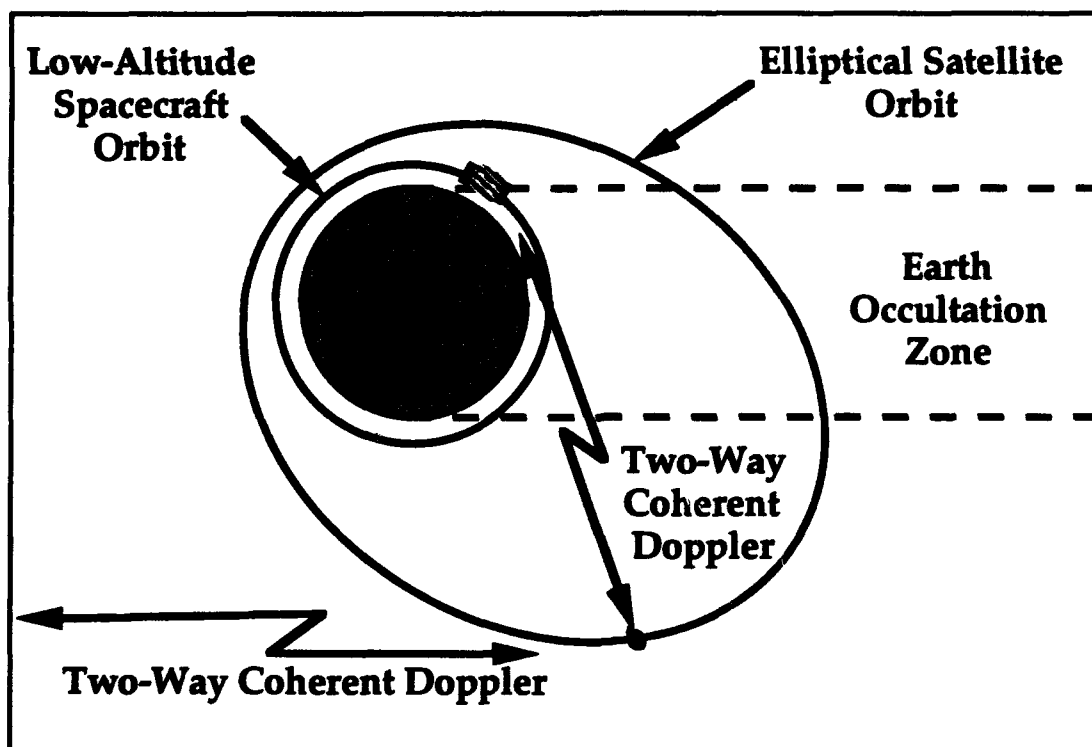


Figure 1.4-1: Dual Orbiter Sensing Method

The bent pipe method uses a four-way coherent Doppler scheme in which a high frequency is generated by an atomic clock at a DSN tracking site and transmitted to the elliptical "viewing" satellite. The "viewing" satellite uses the Doppler-shifted received signal to generate a lower frequency signal which it transmits to the circular "gravity sensing" spacecraft. This spacecraft receives the Doppler-shifted signal and re-transmits it to the "viewing" satellite. The "viewing" satellite modulates the received Doppler-shifted

frequency signal from the "sensing" spacecraft onto the frequency signal received from the tracking station and transmits this signal back to earth. The signal received by the tracking station is then processed to retrieve both the relative velocities between the tracking station and "viewing" satellite and between the "viewing" and "gravity sensing" satellites.

The satellite bounce method uses a two-way coherent Doppler scheme between the two spacecraft. The circular "gravity sensing" satellite generates a continuous wave frequency signal for transmission to the elliptical "viewing" satellite. This satellite shifts the signal's frequency for transmission back to the first one. The receiving spacecraft extracts the Doppler shift from the signal, records it and transmits it to earth when in view of an earth tracking station. Coherent Doppler links between earth tracking stations and either satellite are used to aid in the estimation of the lunar gravitational field.

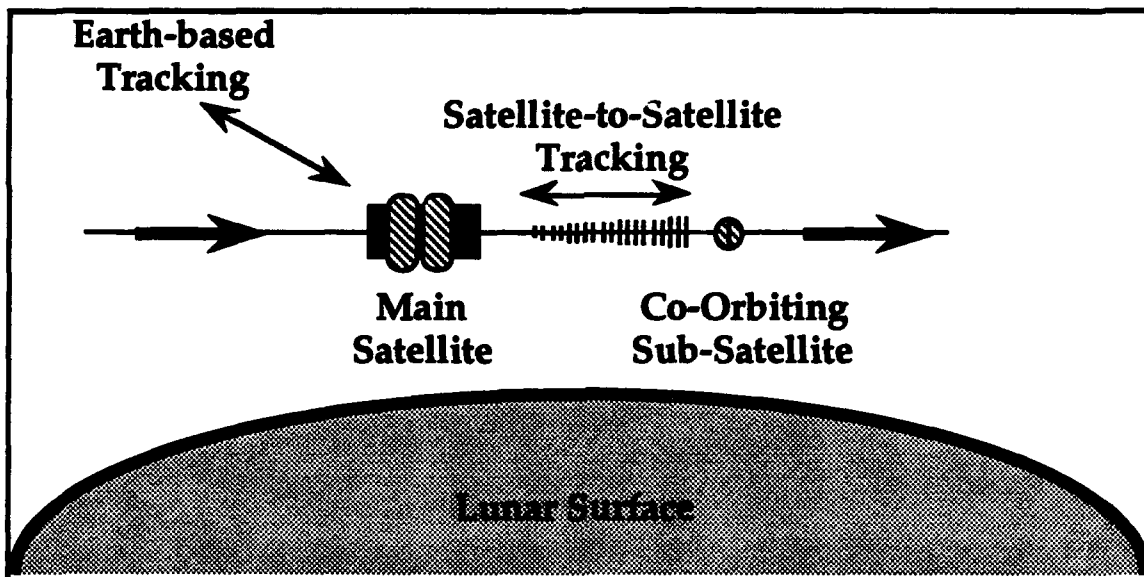


Figure 1.4-2: Co-orbital Sensing Method

NASA's Goddard Space Flight Center has proposed a co-orbital scheme in which a satellite in a circular polar orbit ejects a subsatellite in the same orbit (Figure 1.4-2). Both spacecraft are affected by lunar gravitational perturbations, so both are "sensing" vehicles and a laser system measures their relative motion. The satellite contains the sensing equipment and the subsatellite is a passive reflector for the satellite's emitted laser beams. The satellite's laser transmits a light beam toward the subsatellite. This beam reflects off of the subsatellite back to the satellite. A high accuracy ranging

## LUNAR GRAVITATIONAL FIELD ESTIMATION AND SATELLITE ORBIT PREDICTION

measurement between the satellite and subsatellite is made by determining the travel time of a transmitted sub-carrier pulse signal. Lesser accuracy Doppler relative velocity measurements are made from the frequency shifting of the transmitted laser signal. Observation data is stored and transmitted to earth at regular intervals.

### **1.5 Simulation Tools**

The primary tool used to accomplish the goals of this thesis is the Planetary Ephemeris Program (PEP), a FORTRAN computer program obtained from the Smithsonian Astrophysical Observatory (SAO) and executed on Sun workstations at the Charles Stark Draper Laboratory. The Smithsonian version of PEP has most of the capabilities needed for the analyses of this thesis. Modifications, coded at Draper Laboratory, have augmented its capabilities for this thesis research. In addition, auxiliary software has been developed to analyze lunar orbits, the observation schemes, navigation uncertainties, and estimated lunar gravitational fields.

Given the description of a body's gravitational field, PEP can numerically integrate a satellite's motion about that body. For this thesis, PEP was modified to accommodate a point mass (mascon) gravity model in addition to the spherical harmonic model. The techniques used in PEP for numerically integrating the differential equations of motion for a lunar satellite are described in Chapter Three. This chapter also describes the methods PEP uses to calculate the partial derivatives of the motion with respect to orbital initial conditions, gravity harmonic coefficients, and other parameters. The mascon gravity model modifications coded in PEP are also covered in Chapter Three.

The Planetary Ephemeris Program (PEP) can also process the astronomical observations generated by the various lunar gravitational sensing methods. The many different types of observations that can be processed in PEP are described in Chapter Four. This chapter also discusses how PEP generates simulated observations with a truth model (mascon and

spherical harmonic expansion) and then estimates theoretical values of the observations for another model (spherical harmonic expansion) to fit those "truth model" observations. Least squares maximum likelihood estimation and prediction uncertainty propagation techniques are described in Chapter Five. For this thesis, noise has not been included in the satellite dynamics. Kalman filter and system identification techniques may be needed when processing real observations, because of the noise due to radiation pressure, gas leakage, and other unmodeled forces. These estimation techniques are also described in Chapter Five.

## **1.6 Methodology**

The focus of this thesis is the estimation of a lunar gravity field model based on various measurement types and/or orbital geometries. Each unique measurement type and orbital geometry combination will be referred to as a sensing scheme. The standard earth-based orbiter state sensing scheme and the proposed dual orbiter bent pipe scheme are analyzed in-depth. Additionally, the co-orbital laser ranging scheme, a non-coplanar bent pipe scheme, and an earth-based interferometric observation scheme are investigated to determine whether any of these schemes can reduce the parameter correlation's observed during gravitational parameter estimation.

Since the true lunar gravitational field is not precisely known, a "truth" model was developed and used for this investigation, as discussed in Section 6.4. This "truth" model combines Bills and Ferrari's  $16 \times 16$  lunar harmonic model [12] up to degree and order five, along with 78 point masses distributed below the lunar surface to simulate the behavior of mass concentrations. This truth model was used to simulate observations for the various sensing schemes.

For each sensing scheme, the coefficients in spherical harmonic fit models of degree and order 8 and 12 were estimated to optimally represent the "true" gravity field model by fitting to the "truth" model observations. Using first guesses for the fit model coefficients and satellite initial osculating orbital elements, the equations of motion and the equations for the partial

## LUNAR GRAVITATIONAL FIELD ESTIMATION AND SATELLITE ORBIT PREDICTION

derivatives of the motion with respect to these quantities were numerically integrated. From these numerical integrations, theoretical values of the observations were determined. The observation residuals (difference between the "truth" model observations and fit model's theoretical observation values) and the observation partial derivatives were computed and used to obtain parameter adjustments to the first guesses for the fit model coefficients and satellite initial osculating orbital elements. This process was then repeated until either the method converged upon a solution or no solution could be determined. Chapter Six discusses the implementation of the estimation process for various sensing methods and certain test cases.

The estimated lunar gravitational field models were analyzed to determine their accuracy relative to the "truth". Navigation errors propagated in one lunar revolution were used to determine the estimated gravitational field model's accuracy. Two types of lunar orbits were analyzed: a 15° inclination, 100 km altitude, near-circular orbit and a lunar landing from a 5° inclination, 200 km near-circular parking orbit. These orbits were propagated using both the "truth" and estimated models. The analysis of the estimated gravitational field models is discussed in detail in Chapter Seven. In addition, this chapter discusses the attempts made to break the high parameter correlations which were discovered during the estimation process.

For the near-circular orbit, the position and velocity errors between the "truth" and estimated gravity fields were used to quantify the estimated model's accuracy and thus the sensing method's capability. The gravitational parameter covariance matrix, determined during the estimation process, was used with the estimated field's orbit propagation with partial derivatives to predict position and velocity uncertainties. These predicted uncertainties were then compared to the true state errors between the two models' orbits. In real gravity field missions, the true gravity field will not be available for comparison with the estimate, so it is useful to understand the relation between these two analyses.

For the lunar landing maneuver, the estimated gravity field model was used to determine the deorbit burn and the selenographic position for Powered Descent Initiation (PDI). The spacecraft's circular parking orbit was numerically integrated until the appropriate time for the deorbit burn. The

spacecraft's velocity at burn time was then adjusted to simulate the deorbit maneuver and the spacecraft's elliptical transfer orbit was then integrated. The spacecraft's position upon reaching the powered descent stage of the mission was then determined. The "true" PDI point was then compared to the estimated model target PDI point to determine the model's accuracy for planning lunar landing maneuvers.

### **1.7 Summary of Results**

The analyses of the  $8 \times 8$  estimated fit models clearly demonstrated that lunar far-side observations are required in the accurate estimation of the lunar gravity field. For both the lunar landing maneuver and the satellite state uncertainty prediction, the observation technique which included lunar far-side observations in addition to earth-based near-side observations produced a much more accurate lunar gravity fit model. This estimated model planned a lunar deorbit maneuver 4.3 times more accurately than the model based on earth-based observations alone. The earth-based observation fit model also predicted state uncertainties four times larger than its counterpart. The earth- and satellite-based fit model produced state errors for the single orbit that were again roughly a quarter of the earth-based fit model's errors.

The lunar navigation analyses also demonstrate that the eighth degree and order spherical harmonic expansion fit models were unable to adequately model the lunar mascons included in the lunar gravitational "truth" model. In the best case, the  $8 \times 8$  fit model predicted single orbit ahead uncertainties of close to three quarters of a kilometer in position and one meter per second in velocity. The orbit's actual state errors were closer to three kilometers in position and two and a half meters per second in velocity. Additionally, the best fit model produced a fifty-six kilometer position error for the lunar deorbit maneuver. These results are discussed in further detail in Chapter Eight, which also recommends several subjects related to this thesis which deserve further study.

# LUNAR GRAVITATIONAL FIELD ESTIMATION AND SATELLITE ORBIT PREDICTION



## Chapter Two

# Gravity Field Models

### 2.1 LaPlace's Equation and the External Gravitational Field

According to Newton's law of gravitation, two particles attract each other with a force, acting along the line joining them, which is proportional to the product of their masses and inversely proportional to the square of the distance between them [10, p. 95]. From this law, the gravitational force of a body of mass  $m_2$  acting upon a body of mass  $m_1$  can be mathematically represented by the formula:

$$\bar{F} = \frac{Gm_1m_2}{|\bar{r}_2 - \bar{r}_1|^3} (\bar{r}_2 - \bar{r}_1) \quad (2.1-1)$$

where  $G$  is the universal gravitational constant, and  $\bar{r}_1$  and  $\bar{r}_2$  are the position vectors of bodies one and two respectively.

Unfortunately, this formula is only appropriate if the two bodies are point masses, or behave as them. Such is the case for spherical bodies if density is a function of radius from the center only. The point mass model also provides an accurate representation of the gravitational attraction for widely separated bodies. In the limit of large distances, gravitational bodies tend to look like point masses so that mass distribution becomes unimportant.

For many practical applications, the attracting body cannot be modeled as a point mass and a different mathematical model must be developed. For the case in which the attracted body is small compared to the attracting body and the attracting body is an arbitrary distribution of mass with a finite

dimension, the force on a mass  $m$  located at position vector  $\vec{r}$  in Figure 2.1-1 produced by an element of mass  $dM$  with position vector  $\vec{R}$  is

$$d\vec{F}(\vec{r}) = -G m dM \frac{(\vec{r} - \vec{R})}{|\vec{r} - \vec{R}|^3} \quad (2.1-2)$$

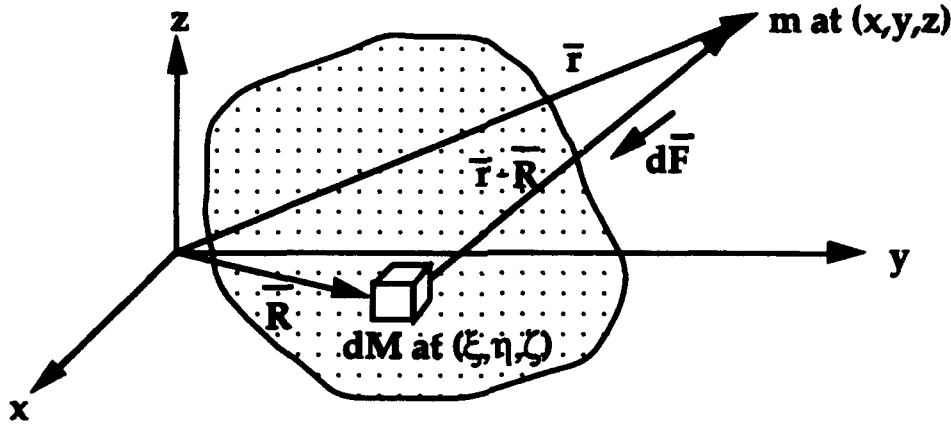


Figure 2.1-1: Distributed Mass acting upon a Point Mass  $m$

Integration over the entire volume of the distributed body will produce the gravitational force on the mass  $m$  of the attracting body of total mass  $M$ . This force can then be represented by a scalar potential  $U$ , such that the gravitational force on a body located outside of the attracting body may be obtained as the gradient of the scalar potential, or

$$\vec{F}(\vec{r}) = -m \vec{\nabla} U(\vec{r}). \quad (2.1-3)$$

There is a sign convention discrepancy between some of the references used and PEP documentation [8]. According to Kaula [24], physicists define the gradient of the potential field as in Equation (2.1-3), whereas astronomers define the same gradient with a change in sign. The formulas in this thesis follow the former convention to agree with PEP documentation and software coding modifications explained herein.

The scalar gravitational potential  $U$  can be written in terms of the rectangular coordinate system of Figure 2.1-1 and the mass density  $\rho$  as [14]

$$\begin{aligned} U(\vec{r}) &= -G \iiint \frac{dM}{|\vec{r} - \vec{R}|} \\ &= -G \iiint \frac{\rho(\xi, \eta, \zeta)}{[(x - \xi)^2 + (y - \eta)^2 + (z - \zeta)^2]^{1/2}} d\xi d\eta d\zeta \end{aligned} \quad (2.1-4)$$

The Laplacian of the scalar potential  $U$  in rectangular coordinates is

$$\nabla^2 U = \frac{\partial^2 U}{\partial x^2} + \frac{\partial^2 U}{\partial y^2} + \frac{\partial^2 U}{\partial z^2} \quad (2.1-5)$$

Taking the required partial derivatives of the potential  $U$  from (2.1-4) yields

$$\nabla^2 U = -GM \left[ \frac{-3}{\left[ (x-\xi)^2 + (y-\eta)^2 + (z-\zeta)^2 \right]^{3/2}} + 3 \frac{\left[ (x-\xi)^2 + (y-\eta)^2 + (z-\zeta)^2 \right]}{\left[ (x-\xi)^2 + (y-\eta)^2 + (z-\zeta)^2 \right]^{5/2}} \right] \quad (2.1-6)$$

Since the bracketed terms cancel, this reduces to

$$\nabla^2 U \equiv 0 \quad (2.1-7)$$

This relationship is known as Laplace's equation and applies at all points outside of the distributed attracting mass. Its solutions are called harmonic functions. Any scalar function,  $U$ , which satisfies Laplace's equation and the far-field boundary condition that the potential approaches 0 as  $1/r$  can be used to describe the gravitational field about some distributed mass. If  $U$  is defined with sufficient flexibility, i.e. an infinite number of orthogonal terms with undefined constant coefficients, then  $U$  can be tailored to describe the gravitational field outside of any arbitrarily distributed mass. The above method of deriving (2.1.7) is based upon the method used by Kaula [24], Battin [10], and Comfort [14].

## 2.2 Spherical Harmonic Expansion for the Gravitational Potential

The most common gravitational potential model is the spherical harmonic expansion. This expansion can be derived by solving Laplace's equation in spherical harmonic coordinates. First, the rectangular coordinate system of Figure 2.1-1 is converted to spherical coordinates through the transformation below, which is depicted in Figure 2.2-1. If the center of the distributed mass is selected as the origin of this coordinate system, the expansion is simplified.

$$\left. \begin{aligned} x &= r \cos \theta \cos \phi \\ y &= r \sin \theta \cos \phi \\ z &= r \sin \phi \end{aligned} \right\} \begin{aligned} 0 &\leq r < \infty \\ 0 &\leq \theta < 2\pi \\ -\pi/2 &\leq \phi < \pi/2 \end{aligned} \quad (2.2-1)$$

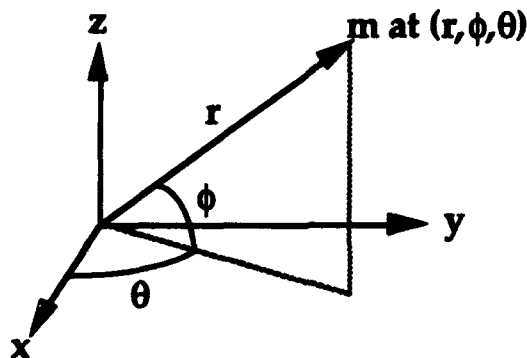


Figure 2.2-1: Spherical Coordinate System

In spherical coordinates, Laplace's equation becomes [24]

$$r^2 \nabla^2 U = \frac{\partial}{\partial r} \left( r^2 \frac{\partial U}{\partial r} \right) + \frac{1}{\cos \phi} \frac{\partial}{\partial \phi} \left( \cos \phi \frac{\partial U}{\partial \phi} \right) + \frac{1}{\cos^2 \phi} \frac{\partial^2 U}{\partial \theta^2} \equiv 0 \quad (2.2-2)$$

One common method of deriving the solution to  $U$  in spherical coordinates is through the method of separation of variables, maintaining the boundary condition on  $r$ . This method can be found in Kaula [24] or Comfort [14] and leads to the solution

$$U(r, \phi, \theta) = \sum_{n=0}^{\infty} \frac{-1}{r^{n+1}} \sum_{m=0}^n P_{nm}(\sin \phi) [C_{nm} \cos m\theta + S_{nm} \sin m\theta] \quad (2.2-3)$$

where  $C_{nm}$  and  $S_{nm}$  are constant coefficients and  $P_{nm}$  are the generalized Legendre functions of degree  $n$  and order  $m$ . Equation (2.2-3) is the complete real solution of Laplace's equation in spherical coordinates. There are other solutions which are physically inadmissible since they cause the potential to become infinite at  $\phi = \pi/2, 3\pi/2$ . These solutions involve the associated Legendre functions of the second kind. Another method of deriving the solution to  $U$  is to expand the denominator of (2.1-4) in Legendre functions. This is the procedure carried out by Battin [10] and Croopnick [18].

Equation (2.2-3) is the generalized solution of Laplace's equation and must be modified for the gravitational case. Laplace's equation holds true everywhere outside the surface of the gravitational body. The harmonic

expansion, however, is convergent only from  $\rho_l$  to  $\infty$  in the radial direction, where  $\rho_l$  is the body's (lunar) maximum radius, usually the equatorial radius. Furthermore,  $\rho_l$  can be used to non-dimensionalize the  $C_{nm}$  and  $S_{nm}$  coefficients as shown in Equation (2.2-4). Secondly,  $U$  is multiplied by the gravitational constant and the total mass of the attracting body to satisfy Equation (2.1-3). The  $n=0, m=0$  term is the point mass approximation for the attracting body and can be separated from the summation for ease of computation. The  $S_{nm}$  coefficient is meaningless for  $m=0$  because  $\sin(m\theta)$  is always zero. Separating the  $m=0$  terms simplifies the summation. The  $P_{n0}(\sin\phi)$  Legendre functions then become the standard  $P_n(\sin\phi)$  Legendre polynomials. When the  $m=0$  terms are separated, the  $C_{n0}$  terms are commonly replaced by  $J_n$  terms, where  $J_n = -C_{n0}$ . After the previous modifications, the spherical harmonic gravitational potential,  $U$ , becomes

$$U(r, \phi, \theta) = \frac{-GM}{r} \left\{ 1 - \sum_{n=1}^{\infty} J_n \left( \frac{\rho_l}{r} \right)^n P_n(\sin \phi) + \sum_{n=1}^{\infty} \left( \frac{\rho_l}{r} \right)^n \sum_{m=1}^n P_{nm}(\sin \phi) [C_{nm} \cos m\theta + S_{nm} \sin m\theta] \right\} \quad (2.2-4)$$

Additionally, if the attracting body's center of mass is the origin of the coordinate system, then the first degree terms are identically zero [22],

$$J_1 = 0, C_{11} = 0, S_{11} = 0 \quad (2.2-5)$$

and the summation limits can begin with the second degree terms.

When dealing with large degree models, it is common to normalize the Legendre functions, and therefore adjust the tesseral coefficients as well. The Legendre functions are normalized to satisfy the equation

$$\begin{cases} \iint (\bar{P}_{nm}(\sin \phi) \cos m\theta)^2 d\theta d\phi = 4\pi \\ \iint (\bar{P}_{nm}(\sin \phi) \sin m\theta)^2 d\theta d\phi = 4\pi \end{cases} \quad \begin{cases} 0 \leq \theta < 2\pi \\ -\pi/2 \leq \phi < \pi/2 \end{cases} \quad (2.2-6)$$

This leads to the following relationship between the unnormalized and normalized Legendre functions and the inverse relationship between the unnormalized and normalized coefficients:

$$\begin{aligned}\bar{P}_n &= \sqrt{2n+1} P_n & (m=0) \\ \bar{P}_{nm} &= \sqrt{\frac{2(2n+1)(n-m)!}{(n+m)!}} P_{nm} & (m>0)\end{aligned}\quad (2.2-7)$$

$$\begin{aligned}\bar{J}_n &= \frac{1}{\sqrt{2n+1}} J_n & (m=0) \\ \begin{bmatrix} \bar{C}_{nm} \\ \bar{S}_{nm} \end{bmatrix} &= \sqrt{\frac{(n+m)!}{2(2n+1)(n-m)!}} \begin{bmatrix} C_{nm} \\ S_{nm} \end{bmatrix} & (m>0)\end{aligned}\quad (2.2-8)$$

The Planetary Ephemeris Program (PEP) was modified to allow normalized Legendre functions to be used for higher degree harmonic models. Normalized coefficients are better conditioned for PEP's floating point parameter estimation algorithms, especially for higher degree models. Appendix A discusses the Legendre polynomials, the generalized Legendre functions and the recursive formulas developed for their implementation. Although use of the normalized Legendre functions was considered necessary for this thesis, this scaling was not considered necessary for the Legendre polynomials. Because of this inconsistency in scaling, the equations coded in the software use normalized tesseral coefficients and unnormalized zonal coefficients.

After accounting for the above-mentioned modifications, the spherical harmonic potential equation (2.2-4) becomes

$$U(r, \phi, \theta) = \frac{-GM}{r} \left\{ 1 - \sum_{n=2}^{\infty} J_n \left( \frac{\rho_l}{r} \right)^n P_n(\sin \phi) + \sum_{n=2}^{\infty} \left( \frac{\rho_l}{r} \right)^n \sum_{m=1}^n [\bar{C}_{nm} \cos m\theta + \bar{S}_{nm} \sin m\theta] \bar{P}_{nm}(\sin \phi) \right\} \quad (2.2-9)$$

The Planetary Ephemeris Program uses this equation with finite summation upper limits. The coding in PEP separates the central body term from the harmonic summations.

### 2.2.1 Relation between Spherical Harmonics and Moments of Inertia

The moments of inertia about a solid body are closely related to the gravitational potential for a distributed mass. An expansion of Equation (2.1-4) for the gravitational potential contains the terms for the moments of inertia.

$$\begin{aligned}
 I_{\xi\xi} &= \iiint_{\text{body}} (\eta^2 + \zeta^2) dm & I_{\xi\eta} &= \iiint_{\text{body}} \xi\eta dm \\
 I_{\eta\eta} &= \iiint_{\text{body}} (\xi^2 + \zeta^2) dm & I_{\xi\zeta} &= \iiint_{\text{body}} \xi\zeta dm \\
 I_{\zeta\zeta} &= \iiint_{\text{body}} (\xi^2 + \eta^2) dm & I_{\eta\zeta} &= \iiint_{\text{body}} \eta\zeta dm
 \end{aligned} \tag{2.2.1-1}$$

Equations (2.2.1-1) are valid for any arbitrary rectangular coordinate system  $(\xi, \eta, \zeta)$  originating at the body's center of mass. The spherical harmonic potential function  $U$  was developed from the  $(r, \phi, \theta)$  coordinate system of Figure 2.2-1 which corresponds to the  $(x, y, z)$  rectangular coordinate system of Figure 2.1-1. Converting the moments of inertia to this  $(x, y, z)$  system, the second degree coefficients in the gravitational potential function satisfy the following relations [24, 30, 32, 44].

$$\begin{aligned}
 C_{20} &= \frac{\frac{1}{2}(I_{xx} + I_{yy}) - I_{zz}}{\rho_1^2 M} & C_{22} &= \frac{I_{yy} - I_{xx}}{4\rho_1^2 M} \\
 C_{21} &= \frac{I_{xz}}{\rho_1^2 M} & S_{21} &= \frac{I_{yz}}{\rho_1^2 M} & S_{22} &= \frac{I_{xy}}{2\rho_1^2 M}
 \end{aligned} \tag{2.2.1-2}$$

Since the lunar moments of inertia can be obtained by observing the physical librations of the moon, the second degree coefficients can be determined without sending spacecraft to the moon. If the  $(x, y, z)$  axes are principle axes, the products of inertia will be zero, resulting in

$$C_{21} = 0, S_{21} = 0, S_{22} = 0 \tag{2.2.1-3}$$

In the lunar case, the principle axes coincide with the  $x$  axis pointing towards the earth and the  $z$  axis pointing along the axis of rotation. Unfortunately, equations (2.2.1-3) do not hold exactly with the inertial reference frame used by PEP in this thesis. Since the lunar moments of

inertia can be experimentally determined from earth, it is possible to simultaneously process lunar rotation observations with satellite observations such as those simulated in this theses. In this manner, equations (2.2.1-3) and the non-zero equations in (2.2.1-2) could be assumed to hold exactly. Processing lunar laser corner reflector observations [13, 17] would provide estimates of the second degree coefficients with a very high degree of confidence and the lunar satellite observations could be simultaneously processed for estimates of the higher degree coefficients.

### 2.2.2 Limitations of the Spherical Harmonic Expansion

Although the spherical harmonic expansion is frequently used to describe the gravitational potential of a distributed mass, it is not an efficient model for all uses. Since the model is based upon spherical coordinates, it produces an uneven resolution of coverage from the equator to the poles. This uneven resolution can lead to modeling inefficiencies.

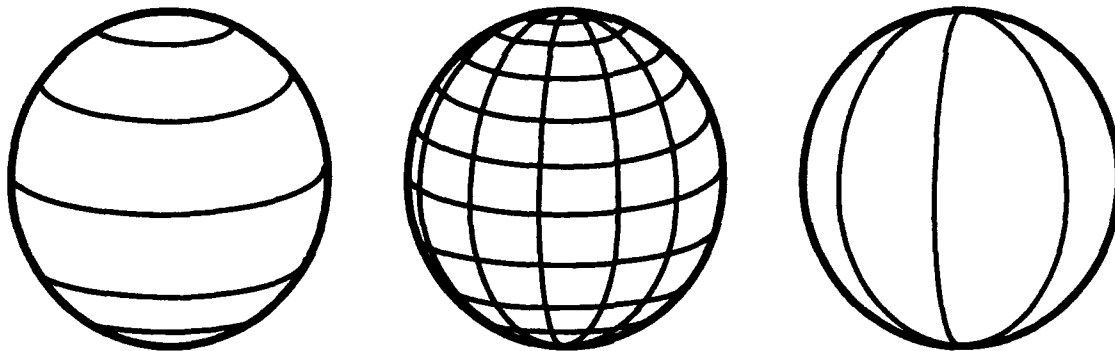


Figure 2.2.2-1: Zonal, Tesseral, and Sectorial Harmonic Patterns

The spherical harmonic model breaks the sphere up into zonal, tesseral, and sectorial patches (Figure 2.2.2-1). The patches are separated by lines where the terms are identically zero. On one side of the line, the term will be positive and on the other it will be negative. The zonal,  $J_n$ , terms, are independent of longitude,  $\theta$ , and dissect the globe of interest into  $n+1$  bands along lines of latitude. The tesseral terms,  $C_{nm}$  and  $S_{nm}$ , dissect the globe of interest into patches of both latitude and longitude. A tesseral term will have  $n-m+1$  sections of latitude and  $2m$  sections along lines of longitude. The sectorial terms,  $C_{nn}$  and  $S_{nn}$ , are independent of latitude,  $\phi$ , and dissect the globe of interest into slices, like sections of an orange.



Defining a spherical harmonic gravitational model with a specific resolution at the equator provides an overly fine longitudinal resolution at the poles. Obviously, finer surface resolutions require higher degree models. The number of harmonic coefficients, however, grows as the square of the degree, so increasing the degree of a model is not an insignificant task. A more efficient model, in terms of coefficients required to define a desired surface resolution, would use equal size mass density patches over the surface of the body. Table 2.2.2-1 lists the degree and order of spherical harmonic models and the number of surface mass density patches required to get various lunar surface angular resolutions for the gravitational potential. The table ignores the difficult patch layout problem and resultant inefficiencies, so that the number of  $n^\circ \times n^\circ$  surface mass density patches is the patch area in steradians ( $n^2\pi^2/180^2$ ) divided into the number of steradians in a sphere ( $4\pi$ ).

Table 2.2.2-1: Spherical Harmonic and Surface Mass Density Surface Resolution Comparison

Resolution			Spherical Harmonics		Surface Layer
Degrees	Km	Traverse Time (100 km Alt)	Degree & Order	# of Coefficients	# of Patches
22.5	683	442 s	16 X 16	285	82
11.25	341	221 s	30 X 30	957	326
3.297	100	65 s	109 X 109	12,096	3,795
1.648	50	32 s	218 X 218	47,957	15,190
1.000	33	20 s	360 X 360	130,317	41,253

Table 2.2.2-1 lists the travel time to cross a patch of given size, since this factor is important in determining the resolution obtainable by observing a low-altitude orbiter. For estimation purposes, there should be at least two observations (or measurements) within the time it takes to fly over a given patch. Therefore, with 60 second Doppler count intervals of a satellite in a 100 km altitude orbit, a spherical harmonic expansion of degree and order 30 is theoretically possible; more than three observations are obtained per surface patch. Unfortunately, this rule of thumb does not account for smaller spherical harmonic patches at the poles or the lack of observations during lunar occultations.

As the table shows, a surface mass density model provides an economy in the number of coefficients estimated, and might be a preferred approach for

modeling or estimating the lunar gravitational field. The simulations of this thesis, however, were done with the spherical harmonic model since a surface mass density model has not been validated for PEP. Nonetheless, some of these other modeling techniques are discussed here for completeness.

### **2.3 Localized Surface-Layer Gravitational Field Models**

Since lunar mascons act as localized gravitational disturbances, their modeling requires a fine degree of resolution to capture their high frequency content. A very high degree spherical harmonic model is required to model this behavior, which requires the estimation of a very large number of coefficients. As shown in the previous section, a more efficient method of modeling this behavior may be obtained through models focusing on the local, rather than global, behavior. In an attempt to recreate their high harmonic frequency behavior, mascons have been modeled by point masses, lens shaped mass concentrations, and gravity dipoles. In some instances, these mascon models have been used to model the entire lunar gravitational field, and in other cases, they have been combined with low degree spherical harmonic expansions.

#### **2.3.1 Point Mass Model**

The point mass model can be used to represent the behavior of an individual mascon. The gravitational force due to a point mass, Equation (2.1-1), results from taking the gradient of the following potential.

$$U(\vec{r}_1) = \frac{-Gm_2}{|\vec{r}_1 - \vec{r}_2|} \quad (2.3.1-1)$$

Multiple mascons can be modeled by summing the potential contribution of each individual point mass. The resulting potential model for n-1 point masses becomes

$$U(\bar{r}_1) = - \sum_{i=2}^n \frac{Gm_i}{|\bar{r}_1 - \bar{r}_i|} \quad (2.3.1-2)$$

Typically, these point masses are distributed about known mascon locations. To recreate mascon behavior, the location, mass and depth of the point masses are adjusted to fit observations. Point masses are positioned below the lunar surface to avoid singular conditions which would result as the separation distance approaches zero. To globally model the moon's gravitational field with point masses, the model should constrain the total mass and center of mass of the system to known values.

### 2.3.2 Surface Disk Model

Because point mass models did not satisfactorily fit lunar orbit observations, scientists turned to more sophisticated surface layer representations. Scientists at the Aerospace Corporation [47] and the Jet Propulsion Laboratory [4] replaced the point mass model with a surface disk or lens shaped model. This model is derived from the potential of an ellipsoid of uniform density which is given by Equation (2.1-4) with the boundary of the ellipsoid used for the limits of integration. The density function of (2.1-4) is assumed to be constant and integrates to the mass of the body. The boundary condition of an ellipsoid is

$$\frac{x^2}{a^2} + \frac{y^2}{b^2} + \frac{z^2}{c^2} = 1 \quad (2.3.2-1)$$

where  $a$ ,  $b$ , and  $c$  are the dimensions of the ellipsoid along the principal axes  $x$ ,  $y$  and  $z$ . The surface disk or lens model uses the specialized case of an oblate spheroid. Figure 2.3.2-1 shows a prolate spheroid ( $a=b<c$ ) and an oblate spheroid ( $a=b>c$ ). The gravitational attraction for a point outside an oblate spheroid of uniform density is [34]

$$\frac{F_x}{x} = \frac{F_y}{y} = -\frac{3Gm}{2a^3e^3} \left[ \frac{-e}{\sqrt{1+k}} \sqrt{\frac{1+k+e^2}{1+k}} + \sin^{-1} \left( \frac{e}{\sqrt{1+k}} \right) \right] \quad (2.3.2-2a)$$

$$\frac{F_z}{z} = \frac{3Gm}{a^3 e^3} \left[ \frac{ae}{\sqrt{c^2 + a^2 k}} - \tan^{-1} \left( \frac{ae}{\sqrt{(c^2 + a^2 k)}} \right) \right] \quad (2.3.2-2b)$$

where  $e$  is the spheroid's eccentricity, so that  $c^2 = a^2(1 - e^2)$ , and the variable  $k$  is a positive solution to the quadratic equation

$$a^2 k^2 + (a^2 - (x^2 + y^2 + z^2))k - z^2 = 0 \quad (2.3.2-3)$$

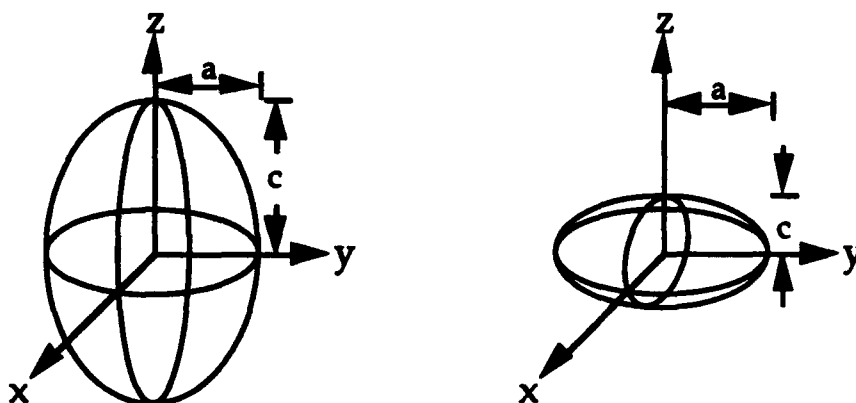


Figure 2.3.2-1: Prolate and Oblate Spheroids

As the thickness,  $c$ , of the spheroid approaches zero, the gravitational attraction of the disk is obtained. The resulting forces are then [47]

$$\begin{aligned} \frac{F_x}{x} = \frac{F_y}{y} &= -\frac{3Gm}{2a^3} \left[ -\frac{\sqrt{k}}{(1+k)} + \sin^{-1} \left( \frac{1}{\sqrt{1+k}} \right) \right] \\ \frac{F_z}{z} &= \frac{3Gm}{a^3} \left[ \frac{1}{\sqrt{k}} - \sin^{-1} \left( \frac{1}{\sqrt{1+k}} \right) \right] \end{aligned} \quad (2.3.2-4)$$

The mass of the disk is  $m$ ,  $a$  is its radius, and the  $x$ ,  $y$ , and  $z$  coordinates are as in Figure 2.3.2-1. In the limit as the disk's radius,  $a$ , approaches zero, the disk shaped model approaches the point mass model.

The Aerospace Corporation scientists used 600 surface disks of 50 km radii covering the lunar surface to model its gravitational field [47]. At JPL, they used 117 lens-shaped mass concentrations placed about 50 km below the lunar surface to model the gravitational field [5]. In the JPL model, the lens-shaped mass concentrations augmented the moon's central body attraction. Both models employed positive and negative mass disks in order to recreate

the observations from lunar satellites. Naturally, negative (repulsive) mass surface disks are not physically realizable, but they do model situations where a lunar surface feature is significantly less dense than its surroundings.

Both of these surface disk models provided better correlation to lunar observations than previous models. Unfortunately, they did not constrain the lunar center of mass. When the models were converted to spherical harmonic models,  $J_1$ ,  $C_{11}$  and  $S_{11}$  coefficients were required. Additionally, both models assumed a priori knowledge of the mass concentration locations and placed them about the moon's surface (or just below it) on a grid pattern. If such a priori knowledge were not used, the estimation process would require five terms to describe each surface disk: radius from the moon's center, latitude, longitude, strength (mass), and disk radius. A better model would have allowed the concentration's location to vary and would have constrained the center of mass. This, however, would have involved too many variables for the model to converge with the given lunar orbiter data.

### 2.3.3 Gravity Dipole Model

A gravity dipole model has also been proposed to account for the effect of anomalous mass concentrations upon low orbiting bodies [18]. A gravitational dipole consists of a mass  $+m$  separated from a fictitious mass  $-m$  by a distance  $d$  (Figure 2.3.3-1). In the limit as  $d$  approaches zero,  $m$  is assumed to get larger so that the product  $md$  remains constant. The strength of the dipole,  $D$ , is the result of the following limit

$$\bar{n} \lim_{d \rightarrow 0} m(\bar{r}') d = \bar{D}(\bar{r}') \quad (2.3.3-1)$$

Gravitational dipoles have never been shown to physically exist, but a distribution of these dipoles can be useful for modeling the lunar gravity field.

The gravitational potential due to a gravity dipole may be written as

$$U(\bar{r}) = -G \iiint \frac{D(\bar{r}') \cos \theta}{|\bar{r} - \bar{r}'|^2} ds \quad (2.3.3-2)$$

where  $ds$  is a patch of the surface and the other elements are pictured in Figure 2.3.3-1.

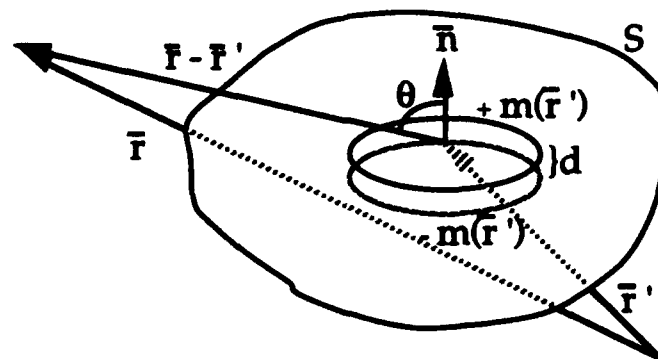


Figure 2.3.3-1: Surface Gravity Dipole

Gravity dipoles can be useful modeling tools because of their unique properties. The most useful property is that they produce a discontinuity in the tangential component of the gravitational field when traversing the dipole layer. The gravitational field normal to the dipole layer, however, remains continuous as the layer is crossed. This allows gravity dipoles to model unexplained out of plane accelerations. Using a ring of mass and gravity dipoles in a continuous line distribution around the lunar equator; Croopnick [18] successfully modeled actual disturbing accelerations beneath a low altitude orbiter. The dipoles were oriented normal to the equatorial plane, so that they were used to account for out-of-plane disturbing accelerations. The mass ring, meanwhile, accounted for the radial and tangential (in plane) components of the disturbing accelerations.

## Chapter Three

# Orbit Propagation

### 3.1 Numerical Integration Techniques

Two classes of perturbation methods are used in celestial mechanics to determine precise spacecraft orbits. General perturbations generalize the expressions for two-body motion to include disturbing effects of other bodies using infinite trigonometric series expansions and integrate these series term by term. Special perturbations use numerical methods for deriving the disturbed orbit by direct integration of the rectangular coordinates or a set of osculating orbital elements [10].

Orbit propagation in PEP is performed using the numerical methods of special perturbations. Numerical orbit determination techniques are preferred because of the ease of implementation and the accuracy of solutions. The growing capabilities and increasing speeds of modern digital computers have significantly increased this method's accuracy and utility. Using Cowell's method, PEP integrates the equations of motion in rectangular coordinates fixed in inertial space. Section 3.2 discusses the units and coordinate frames used in this study's analyses. The equations of motion and the equations for the partial derivatives of motion with respect to gravity harmonic coefficients and initial osculating orbital elements, as used in PEP, are covered in Sections 3.3 and 3.4.

Two of PEP's numerical integration techniques were used for this study: the Adams-Moulton and Nordsieck methods. The Adams-Moulton constant step size integration technique with 11<sup>th</sup> differences was used for the propagation of near-circular lunar orbits [15]. This technique uses predictor-corrector techniques to accurately extrapolate forward in time a satellite's

## LUNAR GRAVITATIONAL FIELD ESTIMATION AND SATELLITE ORBIT PREDICTION

position and velocity. Its integration step size should be smaller than  $1/100^{\text{th}}$  of the satellite's orbital period to ensure numerical stability. An even smaller step size must be used to accurately sample higher degree gravitational harmonics. A very conservative rule of thumb is to use a step size of  $1/(100n)$  of an orbital period to simulate an  $n \times n$  degree and order spherical harmonic model. In PEP the step size is  $2^m$  days, where  $m$  is a negative number. A two hour lunar orbit using an  $m = -10$  step size will have over 170 steps per orbit, ensuring numerical stability. An  $m = -14$  step size for the same orbit will have over 1,365 steps per orbit, which should adequately model a  $13 \times 13$  spherical harmonic gravity model.

Elliptical orbits were propagated by the Nordsieck fifth degree variable step size technique [38]. Since the technique is self starting, it is used to start the Adams-Moulton method. This technique predicts the orbit ahead using a fifth degree polynomial whose coefficients are approximations to derivatives of the function being integrated. The integration output file therefore contains the satellite position, velocity, acceleration, and jerk [8]. The variable step size uses a smaller step near periapse, where quantities change more rapidly. For highly elliptical orbits, this is a more efficient integration technique, since constant step size methods propagate the entire orbit with the smallest required step size.

Despite the integration step size used, integration quantities are written to an output file using a different step size. This output step size is generally two times the integration step size. For low frequency orbital disturbances, less frequent output step sizes can be used. A satellite's position and/or velocity are determined at specific observation times by interpolating from the satellite's integration output file. Everett eighth difference interpolation is performed on constant step size integration files. This method fits a ninth degree polynomial through the ten output times surrounding the observation time. Hermite interpolation is performed on variable step size integration files. This method uses a fifth degree polynomial agreeing with position, velocity, and acceleration at the two output times surrounding the observation time [8].



### **3.2 Units and Coordinate Systems**

The numerical integration methods of special perturbations require that units of time and the gravitational constant are precisely defined. The time unit in PEP is the coordinate time day defined in terms of atomic time in Appendix B. The distance unit is the Astronomical Unit (AU), defined by setting the square root of the gravitational constant times the mass of the sun to the Gaussian value (see Appendix B).

Numerical integration of the satellite equations of motion are performed in an inertial Cartesian coordinate system. PEP's current inertial coordinate system is based upon the mean equinox and equator of the earth of 1950.0, or Julian Date 2,433,282.423. This coordinate system uses the earth's rotation axis at this time as the z axis, with the x axis along the 1950.0 mean equinox pointing towards the constellation Aries, and the y axis completing a right-handed coordinate system. The transformations between this coordinate system and those fixed in the moon and earth are discussed in Appendix C.

For lunar satellite propagations, the origin of this coordinate system is placed at the moon's center of mass. The coordinates of perturbing bodies during an integration are determined from the coordinates of the earth-moon barycenter relative to the sun, of the moon relative to the earth, and of planets relative to the sun calculated by interpolation from an n-body file supplied from the Smithsonian Astrophysical Observatory (SAO). This n-body file is based upon the SAO's fit to observational data. The moon's coordinates are based upon formulas from Brown's lunar theory.

To analyze the PEP propagated orbits, auxiliary software was written to transform the inertial integration Cartesian coordinates into a selenographic coordinate system. The selenographic coordinate system is also centered at the lunar center of mass, but its z axis is the lunar rotation axis, the x axis points toward the earth, and the y axis completes the right hand coordinate system (see Appendix C.1). One auxiliary software program computes selenographic orbital elements and satellite ground tracks from an inertial integration file. Initial conditions for lunar orbits were chosen in the selenographic coordinate system. The orbital angles ( $i$ ,  $\Omega$ ,  $\omega$ ) were then transformed to the inertial integration coordinate frame in a second auxiliary

## LUNAR GRAVITATIONAL FIELD ESTIMATION AND SATELLITE ORBIT PREDICTION

software program using the transpose of the transformation matrix used in the first program.

For this thesis, inertial Cartesian coordinate frame positions will be referred to as  $\bar{X}$ , and in selenographic Cartesian coordinates as  $\bar{U}$ , where the two are related by the transformation matrix  $R(t)$  as follows (Appendix C.1)

$$\bar{X} = \begin{bmatrix} x \\ y \\ z \end{bmatrix} \quad \bar{U} = \begin{bmatrix} u \\ v \\ w \end{bmatrix} \quad (3.2-1)$$

$$\bar{U} = R(t) \bar{X} = \begin{bmatrix} R_{11} & R_{12} & R_{13} \\ R_{21} & R_{22} & R_{23} \\ R_{31} & R_{32} & R_{33} \end{bmatrix} \bar{X} = \begin{bmatrix} \bar{R}_1^T \\ \bar{R}_2^T \\ \bar{R}_3^T \end{bmatrix} \bar{X} \quad (3.2-2)$$

Additionally, the selenographic Cartesian coordinates are related to the selenographic spherical coordinates  $(r, \phi, \theta)$  by the relationship

$$\begin{bmatrix} u \\ v \\ w \end{bmatrix} = \begin{bmatrix} r \cos \theta \cos \phi \\ r \sin \theta \cos \phi \\ r \sin \phi \end{bmatrix} \quad (3.2-3)$$

so that the inertial coordinate frame can be related to the selenographic spherical coordinates used in the spherical harmonic expansion by the relations

$$r = |\bar{X}| = (\bar{X}^T \bar{X})^{1/2} = |\bar{U}| \quad (3.2-4)$$

$$\sin \phi = \frac{1}{r} (\bar{R}_3^T \bar{X}) \quad \cos \phi = \sqrt{1 - \sin^2 \phi} \quad (3.2-5)$$

$$\cos \theta = \frac{1}{r \cos \phi} (\bar{R}_1^T \bar{X}) \quad \sin \theta = \frac{1}{r \cos \phi} (\bar{R}_2^T \bar{X}) \quad (3.2-6)$$

These transformations are used in PEP's internal transformation routines, in the two auxiliary software programs, and in the partial derivatives of satellite motion equations covered in Section 3.4.

### 3.3 Equations of Satellite Motion

Because of the nature of the equations of motion for a satellite, PEP integrates an augmented state vector,

$$\bar{X}_{bl}^* = \begin{bmatrix} \bar{X}_{bl} \\ \dot{\bar{X}}_{bl} \end{bmatrix} \quad (3.3-1)$$

where  $\bar{X}_{bl}$  is the position of body b (satellite) with respect to body l (the moon) defined by (3.2-1) and  $\dot{\bar{X}}_{bl}$  is its time derivative:

$$\dot{\bar{X}}_{bl} = \frac{d\bar{X}_{bl}}{dt} = [\dot{x} \quad \dot{y} \quad \dot{z}]^T \quad (3.3-2)$$

For the following equations,  $\bar{X}$ ,  $\dot{\bar{X}}$ , and  $\bar{X}^*$  will all be used, although the reader should realize that "state" refers to the augmented state vector,  $\bar{X}^*$ .

The equations of motion for a lunar satellite relative to the moon may be written as:

$$\frac{d^2 \bar{X}_{bl}}{dt^2} = -GM_l \frac{\bar{X}_{bl}}{r_{bl}^3} + \bar{H}_l + \bar{\Psi} + \bar{H}_e + \text{other forces} \quad (3.3-3)$$

with the initial condition at  $t=t_0$

$$\bar{X}_{bl}^* = \bar{X}_{bl0}^* \quad (3.3-4)$$

In this thesis, the "other forces" (radiation pressure, gas leaking, thruster firing) are ignored, but can be included when fitting to real observations. In Equation (3.3-3), the  $H_l$  and  $H_e$  terms are the effects of gravitational harmonics (zonal and tesseral) for the moon and earth respectively, and the  $\Psi$  term is the point mass perturbing accelerations of other bodies upon the spacecraft and the subscripts e, s, and p refer to the earth, sun and planets.

$$\bar{\Psi} = \sum_{i=e,s,p} GM_i \left[ \frac{\bar{X}_{ib}}{r_{ib}^3} - \frac{\bar{X}_{il}}{r_{il}^3} \right] \quad (3.3-5)$$

For the simulations run, the earth and sun perturbing attractions were included. The effect of all other bodies was considered negligible for these simulations.

### 3.3.1 Effect of Lunar Gravitational Harmonics

The acceleration on a satellite due to the gravitational potential  $U$  of the moon is obtained by taking the gradient of the potential (2.1-3). Since Equation (3.3-3) already accounts for the central body attraction, the effect of the remaining harmonics is derived from (2.2-9) without the central body term. The resulting acceleration is

$$\bar{H}_1 = \frac{GM_1}{r_{bl}^2} \left\{ \sum_{n=2}^{N_z} J_n \chi^n \left[ P_n \frac{(n+1)\bar{X}_{bl}}{r_{bl}} - P'_n r_{bl} \left( \frac{\partial \sin \phi}{\partial \bar{X}_{bl}} \right)^T \right] + \sum_{n=2}^{N_t} \chi^n \sum_{m=1}^n \left\{ \begin{aligned} & [\bar{C}_{nm} \cos m\theta + \bar{S}_{nm} \sin m\theta] \times \\ & \left[ \bar{P}'_{nm} r_{bl} \left( \frac{\partial \sin \phi}{\partial \bar{X}_{bl}} \right)^T - \bar{P}_{nm} \frac{(n+1)\bar{X}_{bl}}{r_{bl}} \right] + \\ & m[\bar{S}_{nm} \cos m\theta - \bar{C}_{nm} \sin m\theta] \bar{P}_{nm} r_{bl} \left( \frac{\partial \theta}{\partial \bar{X}_{bl}} \right)^T \end{aligned} \right\} \right\} \quad (3.3.1-1)$$

where  $\chi$  is the ratio of  $\rho_l/r_{bl}$ ,  $N_z$  is the degree of zonals used in the spherical harmonic expansion and  $N_t$  is the degree and order of tesseral harmonics in the expansion. The recursive formulas for  $P_n$ ,  $P'_n$ ,  $\bar{P}_{nm}$ , and  $\bar{P}'_{nm}$  in terms of the argument  $\sin \phi$  which have been coded in PEP are given in Appendix A.

The partial derivatives of the selenographic spherical angles in (3.3.1-1) are obtained by differentiating Equations (3.2-5) and (3.2-6). This differentiation results in the following relationships

$$r_{bl} \left( \frac{\partial \sin \phi}{\partial \bar{X}_{bl}} \right)^T = \bar{R}_3 - \frac{\bar{X}_{bl}}{r_{bl}} \sin \phi \quad (3.3.1-2)$$

$$-\sin \theta \left( \frac{\partial \theta}{\partial \bar{X}_{bl}} \right)^T = \frac{\bar{R}_1}{r \cos \phi} - \frac{\cos \theta}{\cos \phi} \left( \frac{\partial \cos \phi}{\partial \bar{X}_{bl}} \right)^T - \frac{\bar{X}_{bl}}{r_{bl}^2} \cos \theta \quad (3.3.1-3)$$

$$\cos \theta \left( \frac{\partial \theta}{\partial \bar{X}_{bl}} \right)^T = \frac{\bar{R}_2}{r \cos \phi} - \frac{\sin \theta}{\cos \phi} \left( \frac{\partial \cos \phi}{\partial \bar{X}_{bl}} \right)^T - \frac{\bar{X}_{bl}}{r_{bl}^2} \sin \theta \quad (3.3.1-4)$$

Equations (3.3.1-3) and (3.3.1-4) can be simplified by multiplying the first by  $-\sin\theta$ , the second by  $\cos\theta$ , and then adding the two equations. This yields the following formula for the partial derivative with respect to  $\theta$ .

$$\left( \frac{\partial \theta}{\partial \bar{X}_{bl}} \right)^T = \frac{1}{r_{bl} \cos \phi} [\bar{R}_2 \cos \theta - \bar{R}_1 \sin \theta] \quad (3.3.1-5)$$

Equation (3.3.1-1) is singular at  $\phi = \pm 90^\circ$  for PEP's algorithms. This is generally not a problem since it is highly unlikely that a satellite numerical integration step would land exactly over a pole. One simulation, however, used a polar location as an initial condition and PEP was unable to propagate its orbit. The initial mean anomaly for this orbit was altered by one degree and the integration proceeded without any further difficulties.

### 3.3.2 Effect of Other Gravitational Body Harmonics

PEP has the capability to include other (non-central) gravitational body perturbing effects upon a satellite's motion. This enables PEP to handle spacecraft fly-by missions. PEP can include the effects of a destination, or target, body's harmonics upon the motion of a satellite traveling towards one body but which is within the sphere of influence of another body. Using this feature, PEP can also include the earth's  $J_2$  harmonic upon a lunar orbiting satellite. Higher order terms can also be included for integration accuracy, but are rarely required.

The effect of earth perturbations on the motion of a lunar satellite relative to the moon ( $H_e$  from (3.3-3)) is the difference between the effect of the earth on the satellite ( $H_{be}$ ) and the effect of the earth on the moon ( $H_{le}$ ).  $H_{be}$  is given by Equation (3.3.1-1) with a change of subscripts, replacing subscript  $l$  with  $e$ . The effect of earth harmonics upon the moon is calculated by replacing the  $GM_l$  terms in (3.3.1-1) by  $GM_c$ , (the subscript  $c$  refers to the earth-moon barycenter), the subscript  $l$  by  $e$ , and the subscript  $b$  by  $l$ . The  $H_e$  term in (3.3-3) is then given by

$$\bar{H}_e = \bar{H}_{be} - \bar{H}_{le} \quad (3.3.2-1)$$

## LUNAR GRAVITATIONAL FIELD ESTIMATION AND SATELLITE ORBIT PREDICTION

Since low altitude lunar orbits and eccentric orbits with apolune on the far side of the moon were simulated, no earth perturbing effects were included. When processing real observations to estimate the lunar gravitational field, earth's  $J_2$  harmonic should be considered since it is three orders of magnitude larger than the other earth harmonics.

### 3.3.3 Effect of Mass Concentrations

For this thesis, PEP was modified to include the effects of mascons upon lunar orbiting satellites. Since these modifications have not been integrated into the SAO's version of the software, the Draper Laboratory modified version will be referred to as PEP-D. PEP-D implements mascons by modeling them as point masses (Section 2.3.1).

Due to mascon model implementation, the equations of motion for a lunar satellite relative to the moon (3.3-3) become, in PEP-D,

$$\frac{d^2 \bar{X}_{bl}}{dt^2} = -GM_l(1-v) \frac{\bar{X}_{bl}}{r_{bl}^3} + \bar{H}_l + \bar{\Psi} + \bar{H}_e + \bar{K} \quad (3.3.3-1)$$

with the same initial conditions, (3.3-4). In Equation (3.3.3-1), the K term is the effect of all of the mascons and  $v$  is their total mass fraction.

The mass of each mascon and its selenographic position in spherical coordinates is entered into PEP-D as the program is initialized. The mass or strength of a mascon is input as a fraction of the total central body mass and both positive and negative values are allowed. If  $N_k$  is the total number of mascons, the total mass fraction of the mascons is then calculated by

$$v = \sum_{i=1}^{N_k} m_i \quad 0 \leq v < 1 \quad (3.3.3-2)$$

The original central body term from (3.3-3) is reduced by the factor  $(1-v)$  to conserve mass in the lunar system. This will allow the lunar mascon model to behave identically to the central force model far from the moon.

The acceleration on a satellite due to the gravitational potential of  $N_k$  mascons is obtained by taking the gradient of the point mass potential (2.3.1-2). The resulting acceleration is

$$\bar{K} = -GM_l \sum_{i=1}^{N_k} \frac{m_i \bar{X}_{bi}}{r_{bi}^3} \quad (3.3.3-3)$$

From the input spherical mascon selenographic coordinates, PEP-D determines their inertial Cartesian coordinates  $\bar{X}_{il}$  using Equation (3.2-3) and the inverse of Equation (3.2-2). The coordinates of the lunar satellite relative to mascon  $i$  and their separation are then

$$\bar{X}_{bi} = \bar{X}_{bl} - \bar{X}_{il} \quad (3.3.3-4)$$

$$r_{bi} = |\bar{X}_{bi}| \quad (3.3.3-5)$$

Unfortunately the mascon implementation in PEP-D does not constrain the lunar center of mass. As mentioned in Section 2.3.2, when converting a surface layer model with an unconstrained center of mass to a spherical harmonic expansion, first degree harmonic coefficients  $J_1$ ,  $C_{11}$ , and  $S_{11}$  need to be determined. Rather than modify PEP-D to estimate first degree coefficients, this thesis uses mascon models in which the lunar center of mass is not disturbed. If any mascons are used, PEP-D calculates the central body center of mass by the formula

$$\bar{X}_{c.m.} = \sum_{i=1}^{N_k} m_i \bar{X}_{il} \quad (3.3.3-6)$$

When the somewhat arbitrary mascon "truth" model was created (Section 6.4), this feature was used to determine the placement and mass of "balancing" mascons to preserve the lunar center of mass.

### 3.4 Partial Derivatives of the Satellite Motion Differential Equation

The partial derivative of Equation (3.3-3) with respect to a parameter  $\alpha$  yields the variational equations that are numerically integrated in PEP along

with the equations of motion. The parameter  $\alpha$  could be one of the orbit's initial conditions, the harmonic coefficients of the gravitational field, or other parameters of interest. Taking into account the effects of mascons, the partial derivative of Equation (3.3.3-1) with respect to the same parameter  $\alpha$  yields PEP-D's variational equations

$$\frac{d^2 \left( \frac{\partial \bar{X}_{bl}}{\partial \alpha} \right)}{dt^2} = \left\{ \begin{aligned} & -\frac{\partial(GM_l)}{\partial \alpha} (1-\nu) \frac{\bar{X}_{bl}}{r_{bl}^3} + \\ & \frac{GM_l}{r_{bl}^3} (1-\nu) \left[ \frac{3\bar{X}_{bl}}{r_{bl}^2} \left( \bar{X}_{bl}^T \frac{\partial \bar{X}_{bl}}{\partial \alpha} \right) - \frac{\partial \bar{X}_{bl}}{\partial \alpha} \right] \\ & + \frac{\partial \bar{H}_l}{\partial \alpha} + \frac{\partial \bar{\Psi}}{\partial \alpha} + \frac{\partial \bar{H}_e}{\partial \alpha} + \frac{\partial \bar{K}}{\partial \alpha} \end{aligned} \right\} \quad (3.4-1)$$

with the initial condition at  $t = t_0$

$$\frac{\partial \bar{X}_{bl}^*}{\partial \alpha} = \frac{\partial \bar{X}_{bl0}^*}{\partial \alpha} \quad (3.4-2)$$

Unless estimating the mass of the moon, the first term in (3.4-1) is zero. Additionally, since the mascon masses were not estimated in this thesis, the ratio  $\nu$  was considered constant.

The effect of perturbing body attractions (point mass approximation) upon the partial derivative with respect to  $\alpha$  is obtained by differentiating Equation (3.3-5), yielding

$$\frac{\partial \bar{\Psi}}{\partial \alpha} = \left\{ \begin{aligned} & \sum_{i=e,s,p} \frac{GM_i}{r_{ib}^3} \left[ \frac{3\bar{X}_{ib}}{r_{ib}^2} \left( \bar{X}_{ib}^T \frac{\partial \bar{X}_{ib}}{\partial \alpha} \right) - \frac{\partial \bar{X}_{ib}}{\partial \alpha} \right] \\ & - \sum_{i=e,s,p} \frac{GM_i}{r_{il}^3} \left[ \frac{3\bar{X}_{il}}{r_{il}^2} \left( \bar{X}_{il}^T \frac{\partial \bar{X}_{il}}{\partial \alpha} \right) - \frac{\partial \bar{X}_{il}}{\partial \alpha} \right] \end{aligned} \right\} \quad (3.4-3)$$

### 3.4.1 Effect of Lunar Spherical Harmonics on the Partial Derivatives

The effect of the lunar gravitational harmonics upon the partial derivatives of satellite motion with respect to a parameter  $\alpha$  is obtained by



differentiating Equation (3.3.1-1) term by term. After differentiating, like series summations can be regrouped for numerical algorithms. The resulting equation takes the form

$$\frac{\partial \bar{H}_l}{\partial \alpha} = \frac{\bar{H}_l}{GM_l} \frac{\partial(GM_l)}{\partial \alpha} + \frac{GM_l}{r_{bl}^2} [\bar{Z} + \bar{T}] \quad (3.4.1-1)$$

where  $\bar{Z}$  is the series expansion for the zonal terms and  $\bar{T}$  is the series expansion for the tesseral terms. The first term in (3.4.1-1) is set to zero unless attempting to estimate the mass of the moon.  $\bar{Z}$ , the zonal series expansion, is provided by the following expression:

$$\bar{Z} = \sum_{n=2}^{N_z} \chi^n \left\{ J_n \left[ \begin{aligned} & \frac{\partial J_n}{\partial \alpha} \left[ \frac{(n+1)\bar{X}_{bl}}{r_{bl}} P_n - P'_n r_{bl} \left( \frac{\partial \sin \phi}{\partial \bar{X}_{bl}} \right)^T \right] + \\ & \frac{(n+1)}{r_{bl}} \left[ \frac{\partial \bar{X}_{bl}}{\partial \alpha} - \frac{(n-1)\bar{X}_{bl}}{r_{bl}^2} \left( \bar{X}_{bl}^T \frac{\partial \bar{X}_{bl}}{\partial \alpha} \right) \right] P_n + \\ & \frac{(n+1)}{r_{bl}} \left\{ \left( \frac{\partial \sin \phi}{\partial \bar{X}_{bl}} \right)^T \left( \bar{X}_{bl}^T \frac{\partial \bar{X}_{bl}}{\partial \alpha} \right) + \bar{X}_{bl} \frac{\partial \sin \phi}{\partial \alpha} \right\} P'_n + \\ & - r_{bl} \left( \frac{\partial^2 \sin \phi}{\partial \bar{X}_{bl} \partial \alpha} \right)^T \\ & - \left[ r_{bl} \left( \frac{\partial \sin \phi}{\partial \bar{X}_{bl}} \right)^T \frac{\partial \sin \phi}{\partial \alpha} \right] P''_n \end{aligned} \right] \right\} \quad (3.4.1-2)$$

The first term in the above equation is zero since the zonal coefficients are constant.

After grouping like terms, the series expansion for the tesserals,  $\bar{T}$ , reduces to the following expression:

$$\bar{T} = \sum_{n=2}^{N_t} \chi^n \sum_{m=1}^n \left\{ \begin{aligned} & \left[ \frac{\partial \bar{C}_{nm}}{\partial \alpha} \cos m\theta + \frac{\partial \bar{S}_{nm}}{\partial \alpha} \sin m\theta \right] \times \\ & \left[ \bar{P}'_{nm} r_{bl} \left( \frac{\partial \sin \phi}{\partial \bar{X}_{bl}} \right)^T - \bar{P}_{nm} \frac{(n+1) \bar{X}_{bl}}{r_{bl}} \right] + \\ & m \left[ \frac{\partial \bar{S}_{nm}}{\partial \alpha} \cos m\theta - \frac{\partial \bar{C}_{nm}}{\partial \alpha} \sin m\theta \right] r_{bl} \left( \frac{\partial \theta}{\partial \bar{X}_{bl}} \right)^T \bar{P}_{nm} + \\ & [\bar{C}_{nm} \cos m\theta + \bar{S}_{nm} \sin m\theta] \bar{T}_1 + \\ & m [\bar{S}_{nm} \cos m\theta - \bar{C}_{nm} \sin m\theta] \bar{T}_2 \end{aligned} \right\} \quad (3.4.1-3)$$

The first two terms in this expansion are zero since the tesseral spherical harmonic coefficients are constant. The expansion for  $T_1$  and  $T_2$  are then

$$\bar{T}_1 = \left\{ \begin{aligned} & \left[ \frac{(n+1)}{r_{bl}} \left\{ \frac{(n+3) \bar{X}_{bl}}{r_{bl}^2} \left( \bar{X}_{bl}^T \frac{\partial \bar{X}_{bl}}{\partial \alpha} \right) - \frac{\partial \bar{X}_{bl}}{\partial \alpha} \right\} \right] \bar{P}_{nm} \\ & - m^2 r_{bl} \left( \frac{\partial \theta}{\partial \alpha} \right) \left( \frac{\partial \theta}{\partial \bar{X}_{bl}} \right)^T \right] \\ & + \left[ r_{bl} \left( \frac{\partial^2 \sin \phi}{\partial \bar{X}_{bl} \partial \alpha} \right)^T - \right. \\ & \left. \frac{(n+1)}{r_{bl}} \left\{ \left( \frac{\partial \sin \phi}{\partial \bar{X}_{bl}} \right)^T \left( \bar{X}_{bl}^T \frac{\partial \bar{X}_{bl}}{\partial \alpha} \right) + \bar{X}_{bl} \frac{\partial \sin \phi}{\partial \alpha} \right\} \right] \bar{P}'_{nm} \\ & + \left[ r_{bl} \left( \frac{\partial \sin \phi}{\partial \alpha} \right) \left( \frac{\partial \sin \phi}{\partial \bar{X}_{bl}} \right)^T \right] \bar{P}''_{nm} \end{aligned} \right\} \quad (3.4.1-4)$$

$$\bar{T}_2 = \left\{ \begin{aligned} & r_{bl} \left( \frac{\partial^2 \theta}{\partial \bar{X}_{bl} \partial \alpha} \right)^T - \\ & \frac{(n+1)}{r_{bl}} \left\{ \left( \bar{X}_{bl}^T \frac{\partial \bar{X}_{bl}}{\partial \alpha} \right) \left( \frac{\partial \theta}{\partial \bar{X}_{bl}} \right)^T + \bar{X}_{bl} \frac{\partial \theta}{\partial \alpha} \right\} \bar{P}_{nm}(\sin \phi) \\ & + r_{bl} \left[ \left( \frac{\partial \sin \phi}{\partial \bar{X}_{bl}} \right)^T \frac{\partial \theta}{\partial \alpha} + \left( \frac{\partial \theta}{\partial \bar{X}_{bl}} \right)^T \frac{\partial \sin \phi}{\partial \alpha} \right] \bar{P}'_{nm}(\sin \phi) \end{aligned} \right\} \quad (3.4.1-5)$$

The recursive formulas for calculating  $P_n$ ,  $P'_n$ ,  $P''_n$ ,  $\bar{P}_{nm}$ ,  $\bar{P}'_{nm}$ , and  $\bar{P}''_{nm}$  in terms of their argument  $\sin \phi$  are included in Appendix A.

Additionally, based upon the transformation between selenographic spherical coordinates and the inertial frame (3.2-4), (3.2-5) and (3.2-6), the following partial derivatives are obtained.

$$r_{bl} \frac{\partial \sin \phi}{\partial \alpha} = \left[ \left( \bar{R}_3 - \frac{\bar{X}_{bl} \sin \phi}{r_{bl}} \right)^T \frac{\partial \bar{X}_{bl}}{\partial \alpha} \right] + \frac{\partial \bar{R}_3^T}{\partial \alpha} \bar{X}_{bl} \quad (3.4.1-6)$$

$$r_{bl} \cos \phi \frac{\partial \phi}{\partial \alpha} = \left\{ \begin{aligned} & \left( \frac{\partial \bar{R}_2}{\partial \alpha} \cos \theta - \frac{\partial \bar{R}_1}{\partial \alpha} \sin \theta \right)^T \bar{X}_{bl} \\ & + \left( \bar{R}_2 \cos \theta - \bar{R}_1 \sin \theta \right)^T \frac{\partial \bar{X}_{bl}}{\partial \alpha} \end{aligned} \right\} \quad (3.4.1-7)$$

$$r_{bl} \left( \frac{\partial^2 \sin \phi}{\partial \bar{X}_{bl} \partial \alpha} \right)^T = \left\{ \begin{aligned} & \left[ \frac{2 \bar{X}_{bl} \sin \phi}{r_{bl}^3} - \frac{\bar{R}_3}{r_{bl}^2} \right] \left( \bar{X}_{bl}^T \frac{\partial \bar{X}_{bl}}{\partial \alpha} \right) + \\ & \frac{\partial \bar{R}_3}{\partial \alpha} - \frac{\sin \phi}{r_{bl}} \frac{\partial \bar{X}_{bl}}{\partial \alpha} - \frac{\bar{X}_{bl}}{r_{bl}} \frac{\partial \sin \phi}{\partial \alpha} \end{aligned} \right\} \quad (3.4.1-8)$$

$$r_{bl} \cos \phi \left( \frac{\partial^2 \theta}{\partial \bar{X}_{bl} \partial \alpha} \right)^T = \left\{ \begin{array}{l} \left[ \frac{\partial \bar{R}_2}{\partial \alpha} \cos \theta - \frac{\partial \bar{R}_1}{\partial \alpha} \sin \theta \right] - \\ \left[ \bar{R}_2 \sin \theta + \bar{R}_1 \cos \theta \right] \frac{\partial \theta}{\partial \alpha} \\ + \frac{r_{bl} \sin \phi}{\cos \phi} \frac{\partial \sin \phi}{\partial \alpha} \left( \frac{\partial \theta}{\partial \bar{X}_{bl}} \right)^T \\ - \frac{\cos \phi}{r_{bl}} \left( \bar{X}_{bl}^T \frac{\partial \bar{X}_{bl}}{\partial \alpha} \right) \left( \frac{\partial \theta}{\partial \bar{X}_{bl}} \right)^T \end{array} \right\} \quad (3.4.1-9)$$

PEP has the option of using different degrees of spherical harmonic models for calculating the partial derivatives in Equation (3.4-1) than for calculating the satellite motion in Equation (3.3-3) or (3.3.3-1). Since calculating the effect of the harmonics is such a tedious process, calculating the partial derivative's harmonic effect with a lower degree spherical harmonic model can save quite a bit of computer time. This option works well for high altitude earth satellites where  $J_2$  dominates the other harmonic effects. This option was found impractical for low altitude lunar satellites, so the same degrees  $N_z$  and  $N_t$  were used as the summation upper limits in Equations (3.4-1) as in (3.3.3-1).

### 3.4.2 Effect of Earth Spherical Harmonics on the Partial Derivatives

The effect of earth harmonics on the partial derivatives of satellite motion with respect to a parameter  $\alpha$  is calculated by differentiating Equation (3.3.2-1). This calculation involves differentiating two factors of the form of Equation (3.4.1-1) since the effect of the earth harmonics on the moon must be subtracted from the effect of the earth harmonics upon the lunar satellite. For this thesis, the effect of earth harmonics upon the partial derivatives were neglected in Equation (3.4-1) because all of the orbits propagated were low altitude ones:

$$\frac{\partial \bar{H}_e}{\partial \alpha} = \bar{0} \quad (3.4.2-1)$$

### 3.4.3 Effect of Mass Concentrations upon the Partial Derivatives

The effect of mass concentrations on the partial derivatives of satellite motion with respect to a parameter  $\alpha$  is obtained by differentiating Equation (3.3.3-3) assuming that the total lunar mass remains constant.

$$\frac{\partial \bar{K}}{\partial \alpha} = GM_l \sum_{i=1}^{N_k} \left\{ \frac{m_i}{r_{bi}^3} \left[ \frac{3\bar{X}_{bi}}{r_{bi}^2} \left( \bar{X}_{bi}^T \frac{\partial \bar{X}_{bi}}{\partial \alpha} \right) - \frac{\partial \bar{X}_{bi}}{\partial \alpha} \right] - \frac{\partial m_i}{\partial \alpha} \frac{\bar{X}_{bi}}{r_{bi}^3} \right\} \quad (3.4.3-1)$$

The above equation was not coded into PEP-D. The partial equations were calculated on orbit fitting runs and all of the orbit fitting was done to spherical harmonic models. The spherical harmonic plus mascon truth model was run to generate the satellite observations for each gravitational sensing method, for which partial derivatives were not required. If PEP-D was used to estimate coefficients in a spherical harmonic plus mascon model, this equation would be required and could be used in an estimation fit which varied the mascon strength and location.

### 3.4.4 Effects of Initial Conditions on the Partial Derivatives

The partial derivatives of the satellite's initial conditions with respect to  $\alpha$  from Equation (3.3-4) (used as initial conditions (3.4-2)) are zero unless the parameter itself is a satellite initial condition. For the cases where  $\alpha$  is a Cartesian coordinate initial condition, the partial derivative is obtained from the following relation.

$$\frac{\partial \bar{X}_{b10}^*}{\partial \bar{X}_{b10}^*} = I \equiv \begin{bmatrix} 1 & 0 & 0 & 0 & 0 & 0 \\ 0 & 1 & 0 & 0 & 0 & 0 \\ 0 & 0 & 1 & 0 & 0 & 0 \\ 0 & 0 & 0 & 1 & 0 & 0 \\ 0 & 0 & 0 & 0 & 1 & 0 \\ 0 & 0 & 0 & 0 & 0 & 1 \end{bmatrix} \quad (3.4.4-1)$$

Rather than solve the partial derivatives with respect to inertial Cartesian initial conditions, PEP uses the partial derivatives of the initial osculating elliptical orbital elements ( $a_0, e_0, i_0, \Omega_0, \omega_0, M_0$ ) or ( $a_0, e_0, i_0, \Omega_0, (\Omega+\omega)_0, (\Omega+\omega+M)_0$ ). The osculating orbit is the one which would result if the disturbing forces in Equations (3.3-3) or (3.3.3-1) were instantly "turned off" and the satellite's motion continued along the two-body orbit defined by the

central body force. These orbital elements, like the Cartesian coordinate state vector, completely describe the satellite's initial state. Calculating the partial derivatives with respect to the initial osculating elliptical orbital elements is numerically more efficient because only the partial derivative with respect to the initial osculating semi-major axis grows with time. Reference [6] contains the formulas for the partial derivatives of the initial conditions with respect to the initial osculating elliptic orbital elements in the integration coordinate frame.

### **3.4.5 Checking Partial Derivatives by the Difference Method**

To verify that partial derivatives were being calculated correctly, they were checked using a finite difference method. This method was used to check both position,  $\bar{X}$ , and observation partials. For these checks, orbits and/or observations with partials were generated with two different values of the parameter  $\alpha$  ( $\alpha_1$  and  $\alpha_2$ ). The finite difference method then verifies the partial derivatives of the quantity of interest,  $\Gamma$  (scalar position coordinate or theoretical observation), by verifying the following equality.

$$\frac{1}{2} \left[ \frac{\partial \Gamma}{\partial \alpha} \Big|_{\alpha=\alpha_1} + \frac{\partial \Gamma}{\partial \alpha} \Big|_{\alpha=\alpha_2} \right] = \frac{\Gamma|_{\alpha=\alpha_1} - \Gamma|_{\alpha=\alpha_2}}{\alpha_1 - \alpha_2} \quad (3.4.5-1)$$

This check allows coding errors to be detected and verifies the proper execution of the program. Once coding errors are fixed and the program is being run properly (appropriate control inputs are used), the orbit fitting process generally converges to a solution. If the program is running properly but has difficulty converging upon a solution, this indicates that parameters are too highly correlated, the observations do not provide adequate observability, or the fit model is an inadequate representation of the observed behavior.

## Chapter Four

# Satellite Observations

### 4.1 Observation Simulation and Processing

Knowledge of the world in which we live is based upon observations, or measurements, of physical phenomenon. Theories that attempt to explain and model natural occurrences are developed to explain previous observations and are validated by accurately predicting future behavior. The discovery of the planet Neptune is an example of the impact observations have upon the development and refinement of theoretical models. After the discovery of Uranus, astronomers could not reconcile observations of the planet's motion with theoretical predictions. English astronomer John Couch Adams and French astronomer Urbain-Jean-Joseph Le Verrier, independently studying the motion, concluded that Uranus' behavior was due to a planet beyond it. Using a new model, both astronomers were able to predict the location of this ultra-Uranian planet, and shortly thereafter Neptune was discovered [10, pp. 472-473].

The Planetary Ephemeris Program (PEP) was designed to process observations of the sun, moon, planets, stars, and spacecraft and to further scientific knowledge through this observation processing [8]. PEP processes observations of interplanetary, earth, and lunar spacecraft using observation files. These files, based on actual astronomical observations or simulated observations, are made up of observation series. Observation series are limited to a single sensing method (Section 4.2) and a pair of observation types (Section 4.3). Multiple observation methods, types, periods, and frequencies are accommodated within PEP by either including more than one

## LUNAR GRAVITATIONAL FIELD ESTIMATION AND SATELLITE ORBIT PREDICTION

observation series in an observation file or by using more than one observation file at a time.

To optimally estimate a spherical harmonic expansion fit to the lunar gravity field for this thesis, PEP generated simulated "truth" model observations based upon the observation geometry and measurement type being evaluated. Observation series for each observation geometry and measurement type were created using PEP's dummy observation feature where output observation files were created from knowledge of earth-based observing sites, and observing and observed satellite states determined from numerical orbit propagations which used the gravitational "truth" model. These observation series included each method's associated measurement error - an indication of the statistical accuracy of any given measurement. The error values used were based upon published or calculated instrument capabilities. During the fitting process, the observation files were read and these errors were used to weight the observations.

Treating the "truth" model observations as real, PEP fit a spherical harmonic model to these observations. Using first guesses for the fit model coefficients and satellite initial osculating orbital elements, the equations of motion and the equations for the partial derivatives of the motion with respect to these quantities were numerically integrated. From the numerical integrations, the theoretical observation values were determined. Observation residuals, the difference between the "true" observations and the theoretical values calculated, and the observation partial derivatives were computed and written to an observation output file. This file was later used to update the guess for the gravitational coefficients and orbital initial conditions.

There was no measurement noise added to the "truth" model observations in this thesis. White measurement noise could be added using a random number generator, with any non-zero measurement biases estimated by PEP.

Both "truth" model and theoretical observation values depend upon the location of the observing site, the observation time (signal receive time), the location of the observed body at reflection time, and any distortion factors. PEP determines the receiving site's position or state at signal receive time in



the inertial Cartesian coordinate frame based upon integration or n-body files. For observation processing in cis-lunar space, position is determined relative to the center of the earth. For extremely precise observations, PEP can perform the light time iterations with the center of mass of the solar system as the center of the inertial coordinate system.

The distance between the observed body at a guessed reflection, transpond, or transmission time and the observing site at receive time is converted to light time, and the reflection, transpond, or transmission time is adjusted until the difference between the reflection, transpond, or transmission time and receive time is sufficiently close to the distance between the bodies converted to light seconds.

For two way observation signals, this process is performed twice. The first iteration is used to determine the reflection time and state of the observed body. The second step uses the reflection time (less any systemic delays) and state of the observed body to compute the signal source's send time and position. Bent pipe observations perform these light time iterations as many times as necessary to recreate the path of the electromagnetic signals from signal receive time back to its origin.

## **4.2 Observation Methods**

Astronomical observations are collected using several different methods. The most common observations are taken from earth sites. These can be observations of celestial bodies or man-made spacecraft in earth, lunar, or interplanetary orbits. Additionally, satellite based observations are made of other satellites or of sites on the earth or lunar surface. Finally, bent pipe observations are made in which a signal is passed among multiple satellites and sites. PEP can simulate observations using each of these methods and can also model physical effects which affect these observations.

### **4.2.1 Earth-Based Observations**

PEP contains the coordinates of several earth based sites to process astronomical observations. DSN sites are included in cylindrical coordinates and most other locations are in spherical coordinates. Observation sites not already included can be added to PEP. This will permit the creation of lunar observation sites. If a lunar base or navigation site were established, PEP could process lunar-based observations in the same manner used to process earth-based observations, after some straightforward software modifications.

When an earth-based site is involved in an observation, the site's inertial location with respect to the center of the earth must be determined to calculate the theoretical value of the observations. Given an observation receive or send time in UTC time (as disseminated by the U.S. Naval Observatory Time Service Radio Station, WWV, and other time services), PEP determines the coordinate time (CT), UT1 time, and earth wobble coordinates from look-up tables. International Astronomical Union (IAU) expressions for the sidereal time as a function of UT1 time and the earth precession-nutation matrices as functions of CT time are then evaluated. PEP transforms the observing site's earth fixed coordinates to the integration frame coordinate system using the transformations described in Appendix C.2. PEP can also calculate the partial derivatives of the observing site's integration frame coordinates with respect to cylindrical or spherical coordinates. This feature allows PEP to improve the estimate of the observation site's location in earth fixed coordinates as part of the process. As lunar sites are established, PEP can therefore survey the site's location by processing satellite-, earth-, and lunar-based observations.

### **4.2.2 Satellite-Based Observations**

PEP also allows observations when a satellite is the signal receiving and/or sending site. In this case, PEP uses the satellite's integration file to determine its state and the partial derivatives of the state at receive, bounce/transpond, or send time. When using a lunar satellite for observations, the satellite's state and partial derivatives are translated from lunar- to earth-centered coordinates. The lunar satellite's state and any partial

derivatives at receive, bounce/transpond, or send time are determined using the interpolation methods described in Section 3.1.

#### **4.2.3 Bent Pipe Observations**

PEP also processes observations in which signals pass among several satellites and sites. This coding has been used to recreate two different ranging observations [8]. In the first method, an earth site transmitted a ranging signal to an earth satellite which then transponded the signal to a second earth satellite. This second satellite then transponded the signal to an earth receiving site. The second bent pipe method used the same signal path from the originating earth site through the second satellite, but then the signal was transponded back to the first satellite and then transponded to an earth receiving site. In both cases the earth sending and receiving sites can be the same or different sites. PEP-D can process these same bent pipe observations methods for lunar orbiting spacecraft with earth-based sending and receiving sites. Unfortunately these bent pipe methods currently only process ranging observations (Section 4.3.6). To accommodate bent pipe range rate measurements, PEP will have to be modified.

A bent pipe method using two two-way coherent links has been proposed to observe satellite motion on the far side of the moon (Section 1.4). For this method, an earth-based observation site sends a high frequency signal to a lunar satellite. This Doppler shifted received frequency is used to generate a medium frequency signal for a two-way coherent Doppler loop between two lunar satellites. The returned Doppler shifted medium frequency is then modulated onto the received high frequency signal and transmitted to earth, completing a second coherent loop [40]. Since this observation method was not available for range rate measurements, it was simulated by using two separate, unrelated coherent Doppler loops. Since the proposed method depends on a single frequency source, the simulated method used a perfect, non-drifting frequency source for the satellite-to-satellite loop. This method obtained range rate observables equivalent to the proposed method.

### **4.2.4 Observation Interruptions**

All observations involve the transmission of an electromagnetic signal (light or radio waves) between sending and receiving sites and satellites. Observations therefore depend upon a clear line-of-sight between the sites and satellites. Multiple signal path methods depend upon a clear line-of-sight for each path. For earth observations of a lunar satellite, the line-of-sight can be interrupted by either the earth or the moon. The first case occurs if the line-of-sight passes below the horizon. In the second case, the moon occults the line-of-sight when the lunar satellite passes behind the moon. PEP models both of these observation interruptions and deletes observations from dummy "truth" model observation series.

Given the radius of the occulting body, PEP determines whether the satellite is occulted by its central body using vector descriptions of the observing site, observed satellite, and central body locations. When the observed body becomes occulted by its central body, observations cease until the observed body returns to view. For the gravitational sensing methods simulated, this feature was used with a lunar radius slightly larger than the lunar radius to eliminate poor quality observations and account for satellite acquisition difficulties at the edges.

Given a limiting elevation angle, as depicted in Figure 4.3.1-2, PEP determines whether the line-of-sight has passed below the observing site's horizon using vector descriptions of the line-of-sight and the vector normal to the observing site. PEP discontinues observations while the line-of-sight is below the required elevation angle. This feature was not used in the lunar gravity model estimation simulations since there is at least one observing site facing the moon at all times (these sites are spaced around the earth's longitude). For this thesis, the simulations used a single observing site which made observations through a "transparent" earth rather than using several observing sites and simulating the handing off of observation responsibilities from site to site.

### 4.3 Observation Types

In the past, astronomical measurements were limited to optical sightings of celestial bodies involving angular measurements and sighting times. Angular sighting observation pairs include azimuth and elevation, right ascension and declination, and meridian crossing and elevation angle. More recent astronomical measurements involve electromagnetic waves being transmitted through space. Electromagnetic signals may be reflected, transponded, or transmitted by man-made bodies. In addition, natural bodies are also used to reflect radar signals. These more recent observation techniques can provide precise interferometric angular information as well as accurate range and range rate measurements. Independently of the observation method used, PEP determines the signal path from send to receive time using the light time iterations described in Section 4.1. PEP models any effects which could bend or distort this signal path based upon the type of observation. The aberration of light, the Doppler shift in frequency, atmospheric refraction, ionospheric distortions, general relativity, and interplanetary plasma effects are all modeled in PEP to determine the proper signal path. The adjusted signal path between sending and receiving sites,  $\bar{q}$ , is then used to recreate observations.

#### 4.3.1 Azimuth-Elevation Observations

Early astronomical sightings measured the angles between the apparent line-of-sight to the target body and a reference frame. Azimuth and elevation angle observations at the observing site use the vector normal to the observing site and the plane tangent to it to describe the location of the observed body. The elevation angle is the angle between the line-of-sight and its projection in the tangent plane. The azimuth angle is defined as the angle in the tangent plane between north and the line-of-sight's projection. These vectors and angles are depicted in Figures 4.3.1-1 and 4.3.1-2.

In earth-fixed Cartesian coordinates, the vector  $\hat{p}$  is  $[0\ 0\ 1]^T$  and the unit normal,  $\hat{n}$ , is defined by the longitude  $\theta$  and geodetic latitude  $\phi$  as

$$\hat{n} = \begin{bmatrix} \cos \theta \cos \phi \\ \sin \theta \cos \phi \\ \sin \phi \end{bmatrix} \quad (4.3.1-1)$$

PEP transforms these vectors to the inertial coordinate frame in which  $\bar{q}$  is calculated using the transformations of Appendix C.2.

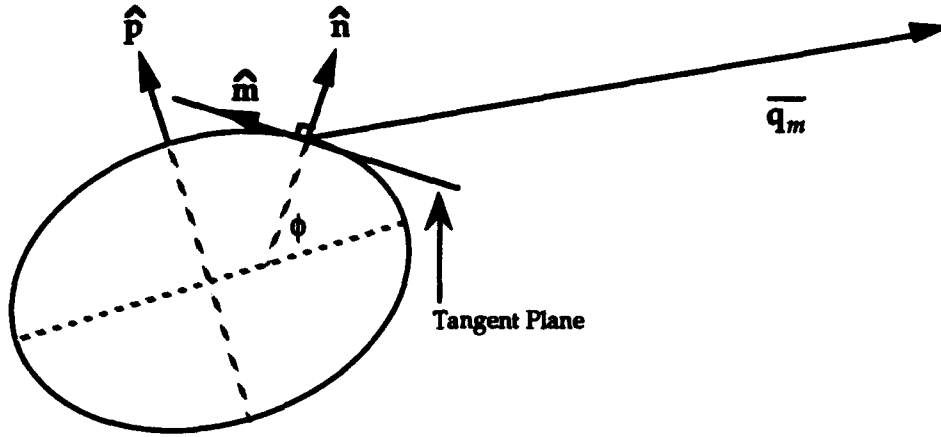


Figure 4.3.1-1: Azimuth-Elevation Angle Vectors in the Meridian Plane

The vector  $\hat{m}$ , which points along the meridian from the observation site towards the north, serves as the north reference direction. This vector is defined by the following equation:

$$\hat{m} = \text{unit}[\hat{p} - (\hat{p} \cdot \hat{n})\hat{n}] \quad (4.3.1-2)$$

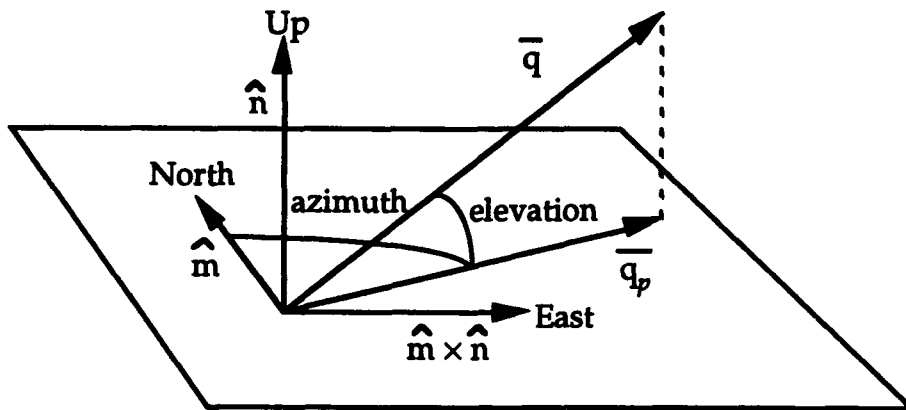


Figure 4.3.1-2: Azimuth-Elevation Angles and the Tangent Plane

The projection of the signal path,  $\bar{q}$ , in the observation site's tangent plane,  $\bar{q}_p$ , is used to define the azimuth angle and is obtained by the equation

$$\bar{q}_p = \bar{q} - (\bar{q} \cdot \hat{n})\hat{n} \quad (4.3.1-3)$$

Additionally, Figure 4.3.1-1 shows the projection of the signal path in the meridian plane,  $\bar{q}_m$ .

The following equations are used to calculate the observed azimuth and elevation angles. Two-argument arctangent routines should be used for improved accuracy and to distinguish the proper quadrants [8].

$$\text{elevation} = \sin^{-1} \left( \frac{\hat{n} \cdot \bar{q}}{|\bar{q}|} \right) \quad (4.3.1-4)$$

$$\text{azimuth} = \tan^{-1} \left( \frac{(\bar{q}_p \times \hat{m}) \cdot \hat{n}}{\bar{q}_p \cdot \hat{m}} \right) \quad (4.3.1-5)$$

#### 4.3.2 Right Ascension-Declination Observations

When an object is observed against a star background, right ascension and declination angles can be determined from the object's relationship to catalogued stars. Right ascension and declination are angles referred to an inertial Cartesian coordinate system centered within the observing body or the true equinox and equator of date. If the line-of-sight vector  $\bar{q}$  is given in the relevant Cartesian coordinate system,  $[x_q \ y_q \ z_q]^T$ , the right ascension and declination angles are calculated from the following relations, where once again two-argument arctangent routines should be used for improved accuracy and quadrant determination [8].

$$\text{declination} = \sin^{-1} \left( \frac{z_q}{|\bar{q}|} \right) \quad (4.3.2-1)$$

$$\text{right ascension} = \tan^{-1} \left( \frac{y_q}{x_q} \right) \quad (4.3.2-2)$$

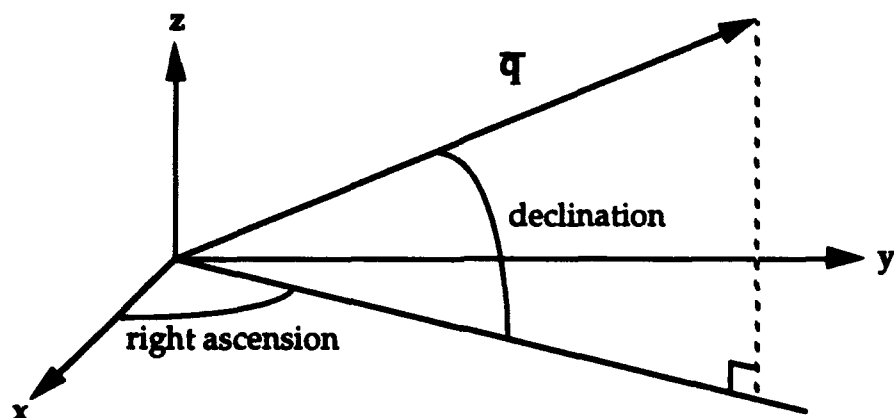


Figure 4.3.2-1: Right Ascension and Declination Angles

### 4.3.3 Meridian Crossing-Elevation Angle Observations

Some of the earliest observations recorded the time and elevation of a celestial body's passage across the earth's meridian. These observations were performed by constraining the sighting instrument in the plane of the meridian and measuring the elevation angle as the observed body crossed the plane. Specifying the time of meridian crossing uses the rotating earth to determine one of the angular components of the line-of-sight from the observing body.

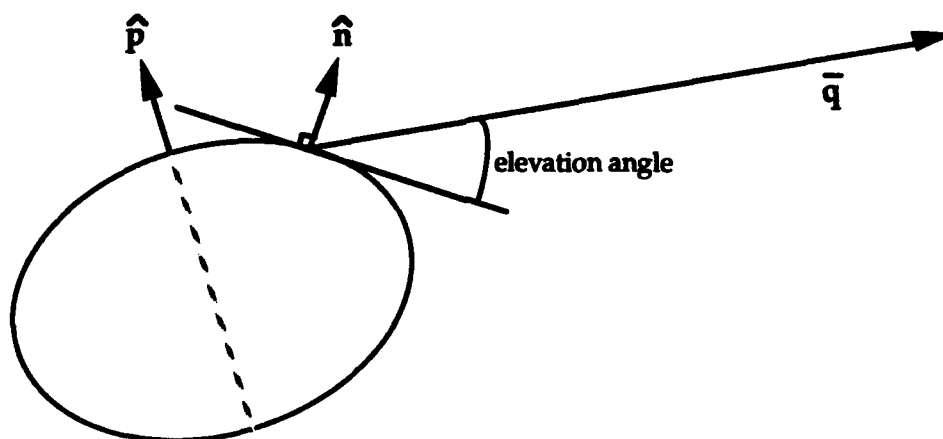


Figure 4.3.3-1: Elevation Angle at Meridian Crossing

This method is similar to the azimuth-elevation observation with the elevation angle constrained to the meridian plane. It is also related to the right ascension-declination observation because the local sidereal time at



meridian crossing, converted to radians, is the right ascension. Based upon the observing body's orbit and rotation, meridian crossing time and elevation angles are converted to right ascension and declination angles [8].

#### 4.3.4 Satellite Look Angle Observations

When a satellite is the observing site, PEP defines the azimuth and elevation angles in the satellite's pitch-roll-yaw coordinate system. The yaw axis,  $\hat{y}$ , points from the satellite to the center of the body which it orbits. The roll axis,  $\hat{r}$ , lies in the orbital plane normal to the yaw axis, making an acute angle with the satellite's velocity vector. The pitch axis,  $\hat{p}$ , is normal to the orbital plane and completes the right hand coordinate system. This coordinate frame is defined for a lunar satellite's position and velocity vectors by the relations

$$\hat{y} = -\text{unit}[\bar{X}_{bl}], \quad \hat{p} = \text{unit}[\bar{X}_{bl} \times \dot{\bar{X}}_{bl}], \quad \hat{r} = \hat{y} \times \hat{p} \quad (4.3.4-1)$$

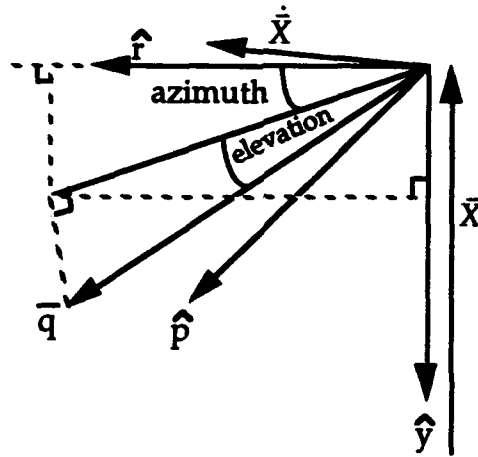


Figure 4.3.4-1: Satellite-Based Look Angles

From this coordinate system, PEP's azimuth angle is defined as the angle about the pitch axis and its elevation angle is the rotation angle from this point to the line-of-sight. These angles are depicted in Figure 4.3.4-1 and the formulas for PEP's azimuth and elevation angles are given below [8].

$$\text{elevation} = \sin^{-1} \left( \frac{\bar{q} \cdot \hat{p}}{|\bar{q}|} \right) \quad (4.3.4-2)$$

$$\text{azimuth} = \tan^{-1} \left( \frac{\bar{q} \cdot \hat{r}}{\bar{q} \cdot \hat{y}} \right) \quad (4.3.4-3)$$

#### 4.3.5 Interferometry Observations

PEP can also determine angular measurements from interferometer measurements. The angle between the incoming wave and the line connecting the two observing sites can be determined when two sites receive an electromagnetic signal and determine its arrival time difference.

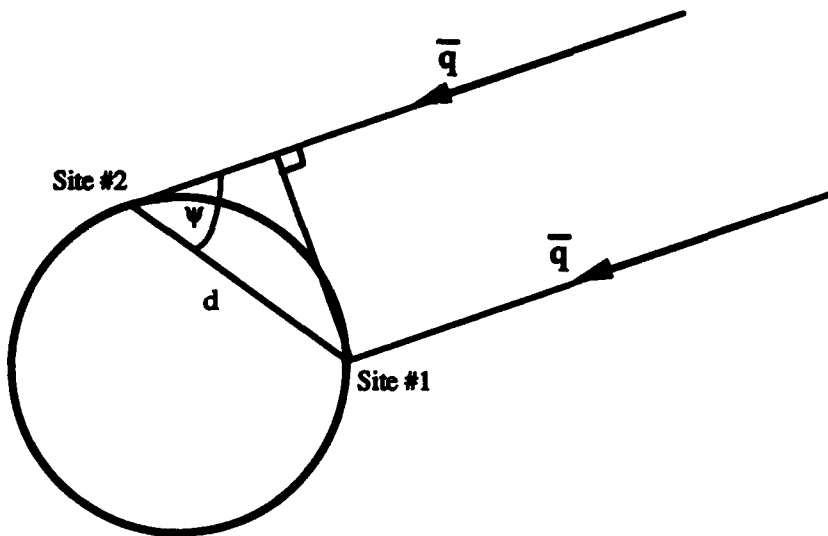


Figure 4.3.5-1: Long Baseline Interferometry Measurement Geometry

If the signal source (such as a radio star) is sufficiently far from two receiving sites separated by a distance  $d$ , then the two signal paths are considered parallel. If the signal arrives at site 2 at a time  $\Delta t$  after it reaches site 1, then this signal has traveled the additional distance  $c\Delta t$ , where  $c$  is the speed of light. The angle  $\psi$  is then determined from the relationship

$$\psi = \cos^{-1} \left( \frac{c\Delta t}{d} \right) \quad (4.3.5-1)$$

The theoretical value of an interferometer measurement of a satellite is the difference between the light times from the two observing sites at the same receive time and the satellite at the signal transmission times. Detecting smaller  $\Delta t$ 's requires increasing the separation between the observing

sites to even intercontinental distances increases the accuracy of interferometric observations. The use of hydrogen maser atomic clocks allows angular measurements with milli-arc second accuracy. Previously discussed angular measurements are limited to approximately an arc second of accuracy. PEP is coded to simulate and process these observations and model the bias between the clocks at the two receiving sites [8].

#### **4.3.6 Range Observations**

The range between two bodies can be determined from the time delay of a signal sent between the bodies. Range measurements depend upon a precise knowledge of when the signal was sent and when the signal was received. Since it is very difficult to synchronize two separated clocks, one-way ranging measurements are not often used, except for multi-GPS satellite observations where receiving site clock error is measured. A two-way signal provides a more accurate single satellite range measurement since a single clock is used to measure the time delay.

Two-way range observations can be obtained by sending a pulsed electromagnetic signal between two bodies. The time it takes the pulse to return to the sending site, less any known delays, reveals the range between the bodies calculated rigorously from light time iterations. Since the electromagnetic signal travels at the speed of light, the range is calculated from the compensated time delay,  $\Delta t$ , as

$$R = \frac{c\Delta t}{2} \quad (4.3.6-1)$$

This two-way range observation can also be obtained with the transmission of a continuous sine wave signal by shifting the phase of the sine wave 180° at a certain repetition interval according to a coded pattern. Since this phase shifting is preserved as the signal passes through space, transponder electronics, or is reflected off of an observed body, the receiving site can recreate the phase shifting coded pattern from the received signal. By correlating the sent coded pattern with the received pattern over time, the receiving site can determine the signal's round trip time delay. Using this phase shift keying technique on a continuous sine wave signal allows the

signal to be used for both range and range rate observations, as well as for communications, if desired [45].

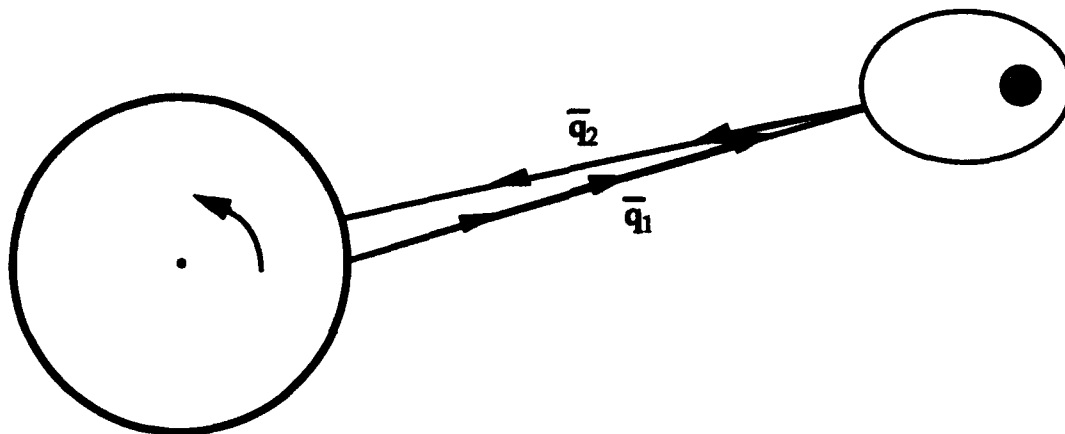


Figure 4.3.6-1: Simulated Two-Way Ranging Measurement

Two-way time delay measurements in PEP are obtained directly from knowing the site and body positions at the appropriate times plus any transponder delays. Transponder time delays can be determined prior to launch or can be estimated from the measurements. Typically both methods are used by separating the time delay into known (previously measured) and unknown (to be estimated) parts.

### 4.3.7 Range Rate Observations

Range rate observations measure the rate at which the observation site and observed body are approaching one another. These observations take advantage of the Doppler effect upon electromagnetic signals. Since this observation measures the change in frequency between send and receive time, it has the same difficulty with one-way observations as range measurements. Coherent two-way signal paths, however, provide very accurate measurements of the range rate between two bodies.

The Doppler effect is a shift in the frequency of an electromagnetic wave radiated, reflected or received by an object in motion. This frequency shift is a result of the expansion or compression of electromagnetic waves along the direction of a moving source [43]. This compression in the direction of motion is visualized in Figure 4.3.7-1 below. For astronomical

range rate measurements, the frequency of the signal sent from site 1 to site 2 is shifted due to the relative velocity of site 1 at send time and site 2 at receive time along the line-of-sight. From the light time iteration process mentioned in Section 4.1, PEP determines this relative velocity from the state of the two sites at the two times in an inertial reference frame.

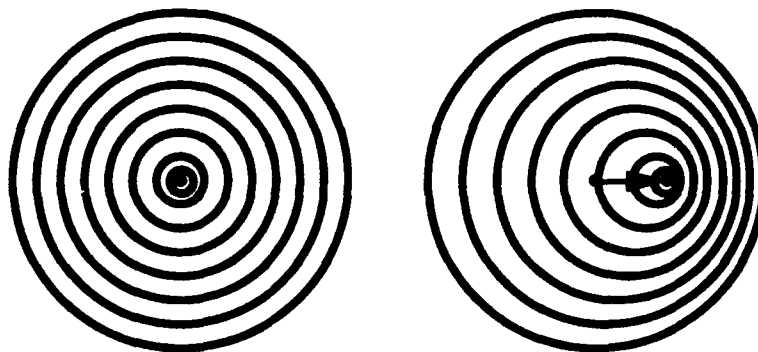


Figure 4.3.7-1: Waves Radiated from a Stationary and Moving Source

For a range rate of  $\dot{R}$ , the one-way Doppler shift of a frequency source,  $f_s$ , is given by the formula

$$\Delta f = -f_s \frac{\dot{R}}{c} \quad (4.3.7-1)$$

$\dot{R}$  is positive when the bodies are moving apart and the signal's frequency is decreasing due to the Doppler shift. This formula is used to determine the frequency received or reflected at the observed body. For radio wave transponder observations, the received frequency is multiplied by a rational factor  $q$ , so that the body transponds a different frequency,  $f_{s2}$ , from the signal it receives.

$$f_{s2} = q f_s \left( 1 - \frac{\dot{R}}{c} \right) \quad (4.3.7-2)$$

Once again, after transmission, this frequency shifts due to the Doppler effect by (4.3.7-1) where  $f_s$  is the send frequency from (4.3.7-2) and the range rate depends upon the new send and receive time positions and velocities.

For approximately instantaneous send and receive times with no transponder frequency shifting ( $q = 1$ ), the round trip Doppler shift is approximated by the single expression [43]

$$\Delta f = -2f_s \frac{\dot{R}}{c} \quad (4.3.7-3)$$

The NASA Deep Space Network (DSN) measures a coherent count of the zero crossings of the Doppler signal, referred to as Integrated Doppler. A DSN site sends a continuous sine wave signal towards a spacecraft at a frequency controlled by an atomic frequency standard. The receiving DSN station can be the same or different from the sending site because of the network's precise synchronization. The receiving station pre-multiplies the transmitted frequency by the spacecraft's transponder translation factor and then subtracts this frequency from the received signal. Any system biases are then added to this differenced frequency, if known, or they can be estimated in the fitting process. A counter at the receiving site is incremented for every positive traveling zero crossing of the differenced frequency. This counter is read at uniform intervals,  $\Delta t$ , to determine the interval's Doppler frequency shift in cycles per second (Hz). Additionally, a resolver is used to give fractional cycle resolution of the zero crossings [36].

Within PEP, the theoretical value of this observable is the difference in round trip phase delays at the count starting and ending receive times multiplied by the sending frequency. PEP also accounts for any transponder frequency translation when calculating the theoretical value of the observation. The exact formula for the Doppler count observable is coded in PEP [8] and is approximately equal to the instantaneous Doppler shift over the count interval.

#### **4.4 Partial Derivatives of Satellite Observations**

The partial derivatives of the theoretical value of an observation are required, along with the observation residuals, to estimate orbital initial conditions and parameters. The theoretical value of an observation is a function of the receiving site coordinates at signal receive time, the observed body's coordinates at transpond time, the sending site's coordinates at send time, and other parameters. If bent pipe observations are used, the theoretical

value is also a function of any additional body's coordinates at the appropriate times. For a given observation,  $\Gamma$ , this functional relationship is denoted by

$$\Gamma(t_r) = f(\bar{X}_{r,s}^*(t_r), \bar{X}_{t,s}^*(t_t), \bar{X}_{s,s}^*(t_s), \dots, \bar{\beta}) \quad (4.4-1)$$

where  $t_r$  is the receive time, r.s. is the receiving site, t.s. is the transponding or reflection site,  $t_t$  is the transpond or reflection time, s.s. is the sending site, and  $t_s$  is the send time. The ellipses denote that  $\Gamma$  may be a function of other coordinates at other times, depending upon the observation method.  $\bar{\beta}$  is the vector of parameters besides motion which affect  $\Gamma$ .

As the theoretical observations are determined, their partial derivatives with respect to the coordinates of interest can also be calculated. Depending upon the type of observation, PEP also calculates the partial derivatives of the observation with respect to the parameters,  $\bar{\beta}$ , which affect the observation, such as measurement biases and transponder delays. The partial derivative of the theoretical observation,  $\Gamma$ , with respect to a parameter of interest,  $\alpha$ , is then calculated by the chain rule.

$$\frac{\partial \Gamma}{\partial \alpha} = \frac{\partial \Gamma}{\partial \bar{X}_{r,s}^*} \frac{\partial \bar{X}_{r,s}^*}{\partial \alpha} + \frac{\partial \Gamma}{\partial \bar{X}_{t,s}^*} \frac{\partial \bar{X}_{t,s}^*}{\partial \alpha} + \frac{\partial \Gamma}{\partial \bar{X}_{s,s}^*} \frac{\partial \bar{X}_{s,s}^*}{\partial \alpha} + \dots + \frac{\partial \Gamma}{\partial \bar{\beta}} \frac{\partial \bar{\beta}}{\partial \alpha} \quad (4.4-2)$$

The parameter  $\alpha$  would be any parameter to be estimated, such as orbital initial conditions, gravitational harmonic coefficients, observing site coordinates or observation biases. The partial derivative of a satellite's coordinates are determined by interpolation from the satellite's integration file using the methods discussed in Section 3.1. The partial derivative of a site coordinate is a function of the site's spherical or cylindrical coordinates.

Once calculated, these partial derivatives are written to an observation output file for each receive time for each observation type in an observation series. The theoretical observations, their partial derivatives, and the observation residuals for each observation series on the output file can then be used to calculate adjustments to the parameters  $\bar{\alpha}$ .

# LUNAR GRAVITATIONAL FIELD ESTIMATION AND SATELLITE ORBIT PREDICTION



## Chapter Five

# Parameter Estimation and Prediction of Uncertainty

### 5.1 Parameter Estimation

Estimation is the process of extracting information from a collection of observations (measurements) to develop a better understanding of the observed behavior. For this thesis, the parameter estimation process attempts to obtain the best set of lunar gravitational harmonic coefficients. The values obtained in the estimation process are best in the sense that the estimated model's generated observations provide the closest match with the "truth" model simulated observations. This does not mean that a better fit could not be realized with more or different "truth" model observations. It also does not imply that a better fit could not be obtained with a better model of the behavior. The estimation process additionally provides insight into the uncertainty of the estimates' ability to model the behavior. This information can be used to analyze and evaluate the estimated model.

#### 5.1.1 Observation Vector as a Random Variable

Using the gravitational "truth" model, observations were generated for several proposed sensing schemes. These observations are dependent on the lunar gravitational field and orbital states of the satellites. Together these observations form the N-dimensional vector  $\bar{z}$  where N is the total number of measurements.

With initial guesses for 1) the lunar gravitational field coefficients, 2) satellite initial conditions (initial osculating orbital elements for each satellite used in the sensing scheme), and 3) measurement biases, theoretical values of the estimated model observations, the difference between the two sets of observations, and the partial derivatives of the estimated model observations are generated. The estimated model observations' theoretical values are a function of the observation time, the estimated model parameters, and other factors, such as the positions of the observing sites. These other factors are treated as known quantities for the estimation process. Let  $\bar{\alpha}_g$  be the vector of unknown gravitational parameters and  $\bar{\beta}$  be the vector of unknown measurement biases and any other unknown parameters. For a sensing scheme with  $N_b$  satellites, there are  $N_b$  vectors  $\bar{\alpha}_n$  of unknown orbital initial conditions. If  $\bar{\alpha}$  is the vector of all of these unknown system parameters, then the theoretical observation at time  $t$  is a function of  $t$  and  $\bar{\alpha}$ .

$$\bar{\alpha}_g = [J_2 \quad \cdots \quad J_{N_s} \mid \bar{C}_{21} \quad \cdots \quad \bar{C}_{N_s, N_s} \mid \bar{S}_{21} \quad \cdots \quad \bar{S}_{N_s, N_s}]^T \quad (5.1.1-1)$$

$$\bar{\alpha}_n = [a_{n0} \quad e_{n0} \quad i_{n0} \quad \Omega_{n0} \quad \omega_{n0} \quad M_{n0}]^T \quad (5.1.1-2)$$

$$\bar{\alpha} = [\bar{\alpha}_g^T \quad \bar{\alpha}_1^T \quad \cdots \quad \bar{\alpha}_{N_b}^T \quad \bar{\beta}^T]^T \quad (5.1.1-3)$$

Due to imperfect knowledge of the gravitational field coefficients and satellite initial conditions and the difference between the fit and truth models, the theoretical observations do not perfectly recreate the "truth" model observations. For each measurement time,  $t$ , there is a measurement error,  $\theta(t)$ , between the "truth" model and theoretical observations. With the "true" values for the parameters  $\bar{\alpha}$ , the remaining measurement error,  $\theta$ , is assumed to be a zero-mean random variable (disregarding the difference between the fit and truth models). Since  $\theta$  is the result of several independent random causes, it will be assumed to be normally distributed by the central limit theorem. The collection of  $N$  measurement errors over the observation period is then  $\bar{\theta}$ .

From the previous definitions, it follows that the vector of measurements is a random vector composed of a deterministic value, the theoretical observation, and a random quantity, the measurement error.

$$\begin{bmatrix} z_1(t_1) \\ z_2(t_2) \\ \vdots \\ z_N(t_N) \end{bmatrix} = \begin{bmatrix} f_1(t_1; \bar{\alpha}) \\ f_2(t_2; \bar{\alpha}) \\ \vdots \\ f_N(t_N; \bar{\alpha}) \end{bmatrix} + \begin{bmatrix} \theta_1 \\ \theta_2 \\ \vdots \\ \theta_N \end{bmatrix}$$

or

(5.1.1-4)

$$\bar{z} = \bar{f}(t; \bar{\alpha}) + \bar{\theta}$$

Since the measurement error,  $\bar{\theta}$ , is assumed normally distributed, the measurement vector is also normally distributed with the following statistics:

$$\bar{\mu} = E\{\bar{z}\} = E\{\bar{f}(t; \bar{\alpha})\} + E\{\bar{\theta}\} = \bar{f}(t; \bar{\alpha}) \quad (5.1.1-5)$$

$$E\{(\bar{z} - \bar{\mu})(\bar{z} - \bar{\mu})^T\} = E\{\bar{\theta}\bar{\theta}^T\} = \Theta \quad (5.1.1-6)$$

### 5.1.2 Maximum Likelihood Estimation

The maximum likelihood estimate selects the parameters  $\bar{\alpha}$  such that the probability of  $\bar{z}$ , the likelihood function, is maximized. This method estimates parameter values so that the "truth" model observations are the most likely ones to have occurred. Since  $\bar{z}$  is a normal random variable, its probability density is the normal joint probability density:

$$p(\bar{z}; \bar{\alpha}) = \frac{1}{\sqrt{(2\pi)^N |\Theta|}} \exp\left[-\frac{1}{2}(\bar{z} - \bar{f}(t; \bar{\alpha}))^T \Theta^{-1}(\bar{z} - \bar{f}(t; \bar{\alpha}))\right] \quad (5.1.2-1)$$

The maximum likelihood estimate maximizes the likelihood function (5.1.2-1) and minimizes the negative log-likelihood function below:

$$\zeta(\bar{z}; \bar{\alpha}) = -\ln[p(\bar{z}; \bar{\alpha})] \quad (5.1.2-2)$$

$$\zeta(\bar{z}; \bar{\alpha}) = \left[\frac{N}{2} \ln(2\pi) + \frac{1}{2} \ln(|\Theta|)\right] + \frac{1}{2}(\bar{z} - \bar{f}(t; \bar{\alpha}))^T \Theta^{-1}(\bar{z} - \bar{f}(t; \bar{\alpha})) \quad (5.1.2-3)$$

The maximum likelihood estimate  $\hat{\bar{\alpha}}$  therefore satisfies the equation

$$\left( \frac{\partial \zeta(\bar{z}; \hat{\bar{\alpha}})}{\partial \bar{\alpha}} \right)^T = \bar{0} \quad (5.1.2-4)$$

The maximum likelihood estimate  $\hat{\bar{\alpha}}$  is obtained starting with an initial guess of the parameters,  $\bar{\alpha}_0$ . Based upon the theoretical observations generated with  $\bar{\alpha}_0$ , adjustments,  $\Delta \bar{\alpha}$ , to the guessed parameters are sought such that

$$\Delta \bar{\alpha} = \hat{\bar{\alpha}} - \bar{\alpha}_0 \quad (5.1.2-5)$$

Expanding Equation (5.1.2-4) in a Taylor series expansion about  $\bar{\alpha}_0$  yields

$$\bar{0} = \left( \frac{\partial \zeta(\bar{z}; \bar{\alpha})}{\partial \bar{\alpha}} \right)^T \Big|_{\bar{\alpha}=\bar{\alpha}_0} + \frac{\partial}{\partial \bar{\alpha}} \left( \frac{\partial \zeta(\bar{z}; \bar{\alpha})}{\partial \bar{\alpha}} \right)^T \Big|_{\bar{\alpha}=\bar{\alpha}_0} \Delta \bar{\alpha} + O(\Delta \bar{\alpha}^2) \quad (5.1.2-6)$$

The parameter adjustments,  $\Delta \bar{\alpha}$ , are determined by taking the partial derivatives of the negative log-likelihood function from Equation (5.1.2-3) (assuming that the term in brackets does not depend on the parameters  $\bar{\alpha}$ ) and by neglecting the higher order terms in the Taylor series expansion. The second derivative of the negative log-likelihood function with respect to  $\bar{\alpha}$  is replaced with its expected value, which can be theoretically expressed as the expected value of the dyadic product of first partial derivatives [42]:

$$E \left\{ \frac{\partial}{\partial \bar{\alpha}} \left( \frac{\partial \zeta(\bar{z}; \bar{\alpha})}{\partial \bar{\alpha}} \right)^T \right\} = E \left\{ \left( \frac{\partial \zeta(\bar{z}; \bar{\alpha})}{\partial \bar{\alpha}} \right)^T \frac{\partial \zeta(\bar{z}; \bar{\alpha})}{\partial \bar{\alpha}} \right\} \quad (5.1.2-7)$$

Assuming that  $\Theta$  does not depend on  $\bar{\alpha}$ , Equations (5.1.2-3) and (5.1.2-7) imply

$$E \left\{ \frac{\partial}{\partial \bar{\alpha}} \left( \frac{\partial \zeta(\bar{z}; \bar{\alpha})}{\partial \bar{\alpha}} \right)^T \right\} = \left( \frac{\partial \bar{f}(\bar{z}; \bar{\alpha})}{\partial \bar{\alpha}} \right)^T \Theta^{-1} \left( \frac{\partial \bar{f}(\bar{z}; \bar{\alpha})}{\partial \bar{\alpha}} \right) \quad (5.1.2-8)$$

Replacing the Hessian of second partial derivatives in Equation (5.1.2-6) by its expected value (the Fisher information approximation) leads to the linear matrix equation, called the normal equations, for the adjustments to the parameters. These equations are formed with the partial derivatives of the theoretical observations with respect to the estimated parameters, the observation residuals, and the measurement error statistics.

$$\mathbf{A} \Delta \bar{\alpha} = \bar{b}$$

or

$$\left[ \left( \frac{\partial \bar{f}(\bar{z}; \bar{\alpha}_0)}{\partial \bar{\alpha}} \right)^T \Theta^{-1} \left( \frac{\partial \bar{f}(\bar{z}; \bar{\alpha}_0)}{\partial \bar{\alpha}} \right) \right] \Delta \bar{\alpha} = \left( \frac{\partial \bar{f}(\bar{z}; \bar{\alpha}_0)}{\partial \bar{\alpha}} \right)^T \Theta^{-1} (\bar{z} - \bar{f}(\bar{z}; \bar{\alpha}_0))$$

(5.1.2-9)

### 5.1.3 Weighted Least Squares Estimation

Least squares estimation selects the parameters  $\hat{\bar{\alpha}}$  so as to minimize the sum of the squares of the deviations between the "truth" model and theoretical measurements. For N observations, the least squares estimate seeks to minimize the quantity

$$Q = \sum_{i=1}^N (z_i - f_i(t_i; \bar{\alpha}))^2$$

(5.1.3-1)

If the measurements are of varying quantities and units, and some measurements are more reliable than others, the weighted cost function Q is used.

$$Q = \sum_{i=1}^N \frac{(z_i - f_i(t_i; \bar{\alpha}))^2}{W_i}$$

(5.1.3-2)

where  $W_i$  is a sequence of weighting values [21]. A sequence of observations may involve a wide variety of physical quantities, i.e. distances, angles, temperatures, frequencies. Typically the error weightings non-dimensionalize these disparate measurements in the cost function.

The least squares or weighted least squares estimate is found by setting the derivative of the cost function with respect to the estimation parameters  $\bar{\alpha}$  equal to zero.

#### 5.1.4 Choice of Estimation Method

The weighted least squares and maximum likelihood methods provide the same estimates if the measurement residuals,  $\bar{\theta}$ , are uncorrelated.

$$E\{\theta_i \theta_j\} = 0 \quad \forall \quad i \neq j \quad (5.1.4-1)$$

By assuming that this measurement noise is uncorrelated, the covariance matrix,  $\Theta$  defined in Equation (5.1.1-6) becomes the diagonal matrix

$$\Theta = \begin{bmatrix} \sigma_1^2 & 0 & \dots & 0 \\ 0 & \sigma_2^2 & \dots & 0 \\ \vdots & \vdots & \ddots & \vdots \\ 0 & 0 & \dots & \sigma_N^2 \end{bmatrix} \quad (5.1.4-2)$$

where  $\sigma_n^2$  is the variance and  $\sigma_n$  is the standard deviation of the  $n^{\text{th}}$  measurement. Inserting this diagonal matrix into Equation (5.1.2-1) and (5.1.2-3) for the likelihood and negative log-likelihood functions results in the following:

$$p(\bar{z}; \bar{\alpha}) = \frac{1}{(2\pi)^{\frac{N}{2}} \sigma_1 \dots \sigma_N} \exp \left[ -\frac{1}{2} \sum_{i=1}^N \frac{(z_i - f_i(t_i; \bar{\alpha}))^2}{\sigma_i^2} \right] \quad (5.1.4-3)$$

$$\zeta(\bar{z}; \bar{\alpha}) = \left[ \frac{N}{2} \ln(2\pi) + \ln(\sigma_1 \dots \sigma_N) \right] + \frac{1}{2} \sum_{i=1}^N \frac{(z_i - f_i(t_i; \bar{\alpha}))^2}{\sigma_i^2} \quad (5.1.4-4)$$

Both the maximum likelihood and weighted least squares estimates are determined by setting the partial derivative of a cost function with respect to  $\bar{\alpha}$  equal to zero. Since the maximum likelihood estimate assumes that the constant part in brackets [ ] from (5.1.4-4) does not depend upon the parameters  $\bar{\alpha}$ , the two methods (compare Equations (5.1.3-2) and (5.1.4-4)) provide identical estimates when uncorrelated measurement error variances,  $\sigma_n^2$ , are used to weight the measurement residuals. Since PEP's parameter estimation routine assumes uncorrelated measurement errors, its estimation technique is referred to as least squares maximum likelihood estimation.

### 5.1.5 Incorporation of A Priori Information

Frequently, existing models provide a priori information about some of the estimation parameters. The estimation process can be shortened or simplified by including this a priori information in the normal equations.

Suppose a priori information has estimated the value of the parameter  $\alpha_i$  as  $\tilde{\alpha}_i$  with an uncertainty, or standard deviation, of  $\tilde{\sigma}_i$ . These a priori parameter values are then grouped into the m-dimensional vector  $\tilde{\alpha}$ , where m is the total number of parameters estimated. A zero value is assigned to any parameters when no a priori knowledge is available. The variances of the a priori estimates are collected into the m x m diagonal matrix  $\tilde{\Sigma}$ . For any parameters without a priori standard deviation information, their diagonal element is infinity, although in practice some reasonably large value will suffice. A full covariance matrix can be used for  $\tilde{\Sigma}$  if correlations are available for the a priori parameter estimates  $\tilde{\alpha}$ .

With a priori information, instead of minimizing Equation (5.1.2-3), the following functional is minimized [11].

$$Q = (\bar{z} - \bar{f}(t; \bar{\alpha}))^T \Theta^{-1} (\bar{z} - \bar{f}(t; \bar{\alpha})) + (\bar{\alpha} - \tilde{\alpha})^T \tilde{\Sigma}^{-1} (\bar{\alpha} - \tilde{\alpha}) \quad (5.1.5-1)$$

For parameters where no a priori standard deviation information is available, the cost function remains the same as in (5.1.2-3).

Setting the partial derivative of this cost function with respect to the parameters  $\bar{\alpha}$  equal to zero and making the same assumptions as in Section 5.1.2, yields the following linear matrix equations.

$$\mathbf{A} = \left( \frac{\partial \bar{f}(\bar{z}; \bar{\alpha}_0)}{\partial \bar{\alpha}} \right)^T \Theta^{-1} \frac{\partial \bar{f}(\bar{z}; \bar{\alpha}_0)}{\partial \bar{\alpha}} + \tilde{\Sigma}^{-1} \quad (5.1.5-2)$$

$$\bar{b} = \left( \frac{\partial \bar{f}(\bar{z}; \bar{\alpha}_0)}{\partial \bar{\alpha}} \right)^T \Theta^{-1} (\bar{z} - \bar{f}(\bar{z}; \bar{\alpha}_0)) - \tilde{\Sigma}^{-1} (\bar{\alpha}_0 - \tilde{\alpha}) \quad (5.1.5-3)$$

such that

$$\Delta \bar{\alpha} = \mathbf{A}^{-1} \bar{b} \quad (5.1.5-4)$$

## LUNAR GRAVITATIONAL FIELD ESTIMATION AND SATELLITE ORBIT PREDICTION

From studies of the earth's gravitational field, William Kaula proposed an empirical relationship for the variance of the gravitational harmonic coefficients [24]. Estimates of the lunar gravitational harmonic coefficients led him to believe that the same relationship was valid. For the lunar coefficients, Kaula adjusted the constant coefficient to account for the gravitational field strength difference between the moon and earth [37]. From their studies of the lunar gravitational field, Bills and Ferrari chose a slightly different semi-empirical formula for the covariance; one which had been proposed by Vening-Meinesz. After having difficulty converging upon gravitational harmonic coefficients, Bills and Ferrari included the Vening-Meinesz a priori covariance information and developed a  $16 \times 16$  lunar spherical harmonic potential model with coefficient uncertainties [12]. Research scientists at JPL continue to use this method to develop  $50 \times 50$ , and even  $75 \times 75$  spherical potential models of the moon [27].

The method of incorporating a priori information into the normal equations was not used for these simulations. This thesis evaluates gravitational sensing schemes which may be employed to develop gravity field models. As such, an arbitrary lunar gravitational "truth" model was developed and there was no a priori information available regarding this "truth" model. When a gravitational sensing method is selected and its mission flown, a priori lunar gravitational field information can and should be used in the development of new gravitational field models.

### 5.1.6 Solution to the Normal Equations

Since the normal equations [(5.1.2-9) or (5.1.5-4)] are linear, the adjustments to the parameters can be solved by various numerical techniques. PEP uses the Gauss-Jordan method to simultaneously solve the normal equations and invert the coefficient matrix. This method uses diagonal pivots without interchanging rows or columns, so that only the lower diagonal half of the symmetric coefficient matrix  $A$  is stored in memory.

Numerical problems can arise if the coefficient matrix is ill-conditioned. This could happen if the vector of parameter adjustments  $\Delta\bar{\alpha}$



consisted of widely different sized quantities or quantities with widely different units. To prevent these numerical difficulties, PEP scales the normal equations prior to solving them. This process scales each row and column of the symmetric coefficient matrix by the square root of the diagonal element. To preserve the equality, each row of the right hand side vector is also scaled by the same factor. After the adjustments to the parameters are solved, PEP unscales its rows to provide the proper units and values to the parameter adjustments [8].

This scaling process can be avoided by using the square root of the normal equations [11]. This method takes advantage of the properties of the symmetric coefficient matrix and, by using the square root of the normal equations, lessens the effect of disparate units or scale factors. The JPL orbit fitting software uses this method [27].

Since the equation for  $\Delta\hat{\alpha}$  was obtained by neglecting second and higher order terms in a Taylor series expansion, this adjustment will not yield  $\hat{\alpha}$  exactly. An iterative technique must be used to approach a maximum likelihood estimate for the parameters. Once the parameter adjustments are determined, the initial parameter guesses are adjusted. The equations of satellite motion are then re-integrated and the theoretical observations, partial derivatives, and residuals are recalculated. The normal equations are then reformed and a second set of parameter adjustments are determined. These iterations continue until the process converges.

### 5.1.7 Other Estimation Techniques

For some applications, least squares maximum likelihood may not be the optimum method for estimating the gravitational coefficients. If noise were included in the satellite dynamics, Kalman filtering techniques would be more appropriate. A linearized Kalman filter about a nominal satellite trajectory or an extended Kalman filter for which the reference trajectory is updated for each observation could be used [31, Chapter 9]. The Kalman filter would then estimate the gravitational parameters as well as the satellite's state by augmenting the state vector to include them as non-dynamic state variables.

Since Kalman filtering techniques become extremely cumbersome as higher degree models are estimated, a more efficient technique may be necessary. Maximum likelihood system identification combines the two approaches by performing a Kalman filter on the satellite state,  $\bar{X}^*$ , and a maximum likelihood estimate on the satellite's orbital initial conditions and the gravitational harmonic coefficients [31, Chapter 10]. In this method, the satellite's motion is propagated with a Kalman filter and then a maximum likelihood adjustment is made to the initial conditions and parameters. The process is then repeated until convergence.

Unmodeled forces such as radiation pressure, fuel tank leakage, and higher order gravitational harmonic effects will cause noise in the satellite dynamics. Because of this noise, one of these techniques should be used. Least squares maximum likelihood estimation, however, was sufficient for this thesis' evaluation of sensing methods.

### **5.2 Statistical Prediction of Uncertainty**

Solving the normal equations produces information about the uncertainty of the estimated parameters  $\hat{\alpha}$  as well as the values of the parameters themselves. The parameter estimation covariance matrix provides a measure of the uncertainty of the estimates. This additional information can be used to evaluate the resulting estimated model of the observed behavior.

The coefficient matrix **A** from (5.1.2-9) and (5.1.5-4) is the Fisher information matrix and by the Cramer-Rao lower bound, the covariance of any unbiased estimate is greater than or equal to its element in the inverse of the Fisher information matrix [42, 46]. Additionally, maximum likelihood estimates have the desirable property that they are asymptotically unbiased with the Cramer-Rao lower bound obtained as the number of observations approaches infinity [42]. This bound only applies if the nonlinear system has been modeled correctly in (5.1.1-4).

If the assumed standard deviation of the measurement errors,  $\sigma_n$ , are correct and the modeling is correct for both the equations of motion and the observations, the root mean square (rms) of the post-fit observation residuals divided by the assumed measurement errors would be approximately one:

$$\text{rms} = \sqrt{\frac{1}{N-m} (\bar{z} - \bar{f}(t; \bar{\alpha}))^T \Theta^{-1} (\bar{z} - \bar{f}(t; \bar{\alpha}))} \quad (5.2-1)$$

Typically the number of observations is much greater than the number of parameters, so the  $1/(N-m)$  term is replaced by  $1/N$ . When the above rms differs greatly from one, the parameter covariance matrix produced by the inverse of the coefficient matrix from the normal equations ( $A^{-1}$ ), by the Cramer-Rao lower bound, should be multiplied by this rms to obtain a truer estimate of the uncertainty in the parameter estimates. This adjustment accounts for incorrect values of the measurement standard deviations,  $\sigma_n$  in  $\Theta$ , but does not account for any modeling error effects on the uncertainty.

The parameter covariance matrix,  $\Sigma$ , is then obtained as

$$\Sigma = \text{rms} \times A^{-1} \quad (5.2-2)$$

The standard deviation of parameter estimate  $\hat{\alpha}_i$  is

$$\sigma_i = \sqrt{\Sigma_{ii}} \quad (5.2-3)$$

and the correlation between parameter estimates  $\hat{\alpha}_i$  and  $\hat{\alpha}_j$  is

$$\epsilon_{ij} = \frac{\Sigma_{ij}}{\sigma_i \sigma_j} \quad (5.2-4)$$

PEP saves the matrix  $A^{-1}$  and the rms of the observation residuals divided by the assumed measurement errors resulting from an estimation run so they can be used to predict the uncertainty of an orbit propagated with the estimated parameters  $\hat{\alpha}$ .

Let  $\bar{X}_0^*$  be the state of a lunar satellite at time  $t_0$  assumed to be known perfectly, perhaps by determination from navigation satellite observations. These satellite initial conditions are numerically integrated in time using the estimated gravitational model. Partial derivatives of the satellite's motion with respect to the parameters  $\bar{\alpha}$  are also numerically integrated. The state

covariance matrix,  $\Xi$ , for the uncertainty in the satellite state, can then be calculated at any time  $t$  as

$$\Xi(t) = \frac{\partial \bar{X}^*(t)}{\partial \bar{\alpha}} \Sigma(t) \left( \frac{\partial \bar{X}^*(t)}{\partial \bar{\alpha}} \right)^T \quad (5.2-3)$$

The standard deviation of the uncertainty in any one coordinate direction is the square root of that diagonal element. The root sum square (rss) of the position and velocity uncertainties are then

$$\text{rss}(R) = \sqrt{\Xi_{11} + \Xi_{22} + \Xi_{33}} \quad (5.2-4)$$

$$\text{rss}(V) = \sqrt{\Xi_{44} + \Xi_{55} + \Xi_{66}} \quad (5.2-5)$$

Since the state covariance matrix  $\Xi$  is based upon the augmented state vector (3.3-1), it is partitioned as follows:

$$\Xi(t) = \begin{bmatrix} \Xi^{RR}(t) & \Xi^{RV}(t) \\ \Xi^{RV}(t) & \Xi^{VV}(t) \end{bmatrix} \quad (5.2-6)$$

Often, the cross correlations between position and velocity  $\Xi^{RV}$  are neglected and the covariance matrix for position  $\Xi^{RR}$  and velocity  $\Xi^{VV}$  are used separately to evaluate the uncertainty of orbit prediction. The state uncertainty analyses performed for the estimated lunar gravity fields in Chapter Seven use these individual state covariance matrices rather than the augmented state covariance matrix.

The inertial (x,y,z) coordinate uncertainties thus obtained can also be converted to a local vertical, local horizontal coordinate frame to provide navigation uncertainty information. The local vertical, local horizontal frame is defined by the vertical (VT), down range (DR), and cross track (CT) directions. Their translations from inertial coordinates are obtained by

$$\hat{u}_{VT}(t) = \text{unit}[\bar{X}(t)] \quad (5.2-7)$$

$$\hat{u}_{CT}(t) = \text{unit}[\dot{\bar{X}}(t) \times \bar{X}(t)] \quad (5.2-8)$$

$$\hat{u}_{DR}(t) = \hat{u}_{VT}(t) \times \hat{u}_{CT}(t) \quad (5.2-9)$$

The transformation matrix from local vertical, local horizontal to inertial coordinates is then

$$\mathbf{R}_{IL}(t) = [\hat{u}_{VT}(t) \mid \hat{u}_{CT}(t) \mid \hat{u}_{DR}(t)] \quad (5.2-10)$$

and this transformation can be used to obtain the covariance matrix for the uncertainty in the satellite state in the LVLH frame.

$$\Xi_L^{RR}(t) = \mathbf{R}_{IL}^T(t) \Xi_I^{RR}(t) \mathbf{R}_{IL}(t) \quad (5.2-11)$$

$$\Xi_L^{VV}(t) = \mathbf{R}_{IL}^T(t) \Xi_I^{VV}(t) \mathbf{R}_{IL}(t) \quad (5.2-12)$$

The standard deviation of the uncertainty in any one LVLH coordinate direction is the square root of that diagonal element. With these formulas, the uncertainty of position and velocity in the vertical, cross track, and range directions can be calculated at each time  $t$  due to uncertainties in the estimated parameter  $\hat{\alpha}$ . These routines were coded in analytical software separate from PEP and each estimated gravity model was evaluated in this manner. This analysis was performed for both the PEP supplied covariance matrix ( $A^{-1}$ ) and the covariance adjusted by the rms of the observation residuals divided by the assumed measurement errors. These analyses simulated the propagation of uncertainties onto the far side of the moon after obtaining a navigation fix on the near side.

The previous statistical uncertainty prediction was performed using the assumption that the lunar satellite initial state,  $\bar{X}_0^*$ , was known perfectly. If this is not the case, the same process for calculating the uncertainty of orbit prediction would still apply. In general, the vector of estimated parameters  $\hat{\alpha}$  would be augmented to include estimates of the satellite initial conditions and the process repeated. Since this thesis is concerned with the uncertainty due to a mismodeled lunar gravitational field, perfect knowledge of the satellite's initial conditions was assumed.

### **5.3 Prediction Uncertainty Due to Mismodeling**

The statistical uncertainty analysis presented in the previous section is based upon the assumption that the estimated gravitational model correctly models the lunar gravity field. Due to the inclusion of mascons in the "truth" model, the finite spherical harmonic estimation model could not correctly model the observed behavior. In most real world cases there is no way to account for or analyze the errors between modeled and true behavior because the modeling errors cannot be separated from the other errors. For this thesis, however, a direct comparison between the true and predicted behavior can be made, since both the "truth" and fit models are available.

Given satellite initial conditions,  $\bar{X}_0^*$ , orbits for the truth and fit models can be numerically integrated. At each point in time, the position and velocity deviations between the two models can be calculated. These modeling errors in position and velocity can then be transformed from inertial coordinates to the local vertical, local horizontal frame using the transformations (5.2-7), (5.2-8), and (5.2-9). The root sum square of the position and velocity errors due to gravitational field mismodeling can also be calculated. The impact mismodeling has upon navigation uncertainty prediction is revealed by comparing the modeling errors with the statistical uncertainty predictions.

Once again, using software separate from PEP, this analysis was performed for orbits propagated from the lunar near side to the far side for one orbital period. Additionally, the uncertainty due to mismodeling was analyzed by comparing the "true" path of a lunar landing when the maneuver was calculated based upon simulations using the estimated model and then executed in the "true" lunar gravitational field. These landing errors provide a feel for the impact lunar gravitational field mismodeling will have upon the execution of future space missions.

## Chapter Six

# Orbit Fitting and Gravity Estimation

### 6.1 Methodology

Several different lunar gravitational sensing methods were evaluated using the PEP orbit integration, observation generation, and parameter estimation capabilities described in Chapters Three, Four and Five. For each sensing scheme, the following procedures, depicted in Figure 6.1-1, were used to generate "truth" model observations and estimate gravitational field coefficients.

First, each sensing scheme was analyzed to determine the nature of the satellite orbits employed, the type of observations generated, and the observation accuracy and frequency. Using the "truth" model and these descriptions of the observation method, PEP simulated the mission's orbits and observations, including lunar occultations. Auxiliary software routines converted the integration output to selenographic osculating orbital elements ( $a, e, i, \Omega, \omega, M$ ) as well as selenographic spherical coordinates ( $r, \theta, \phi$ ) versus time. This data was plotted to analyze the orbit's stability over the integration period (14 to 28 days). For stable orbits, the "truth" model observation file was then used to estimate the fit model lunar spherical harmonic coefficients and satellite initial conditions.

For the estimation process, the gravitational harmonic coefficients and satellite initial conditions were perturbed from the "true" values used to generate the observations. The gravity field was altered to reflect the fit

## LUNAR GRAVITATIONAL FIELD ESTIMATION AND SATELLITE ORBIT PREDICTION

model's degree and order ("truth" model usually included mascons). From the initial perturbed parameters,  $\tilde{\alpha}_0$ , the satellite orbits were propagated, theoretical values of the observations were calculated, and the difference between the "truth" model observations and these theoretical observation values (observation residuals) were calculated. Partial derivatives of the motion and partial derivatives of the theoretical observations were calculated with respect to all parameters to be estimated. From the observation residuals

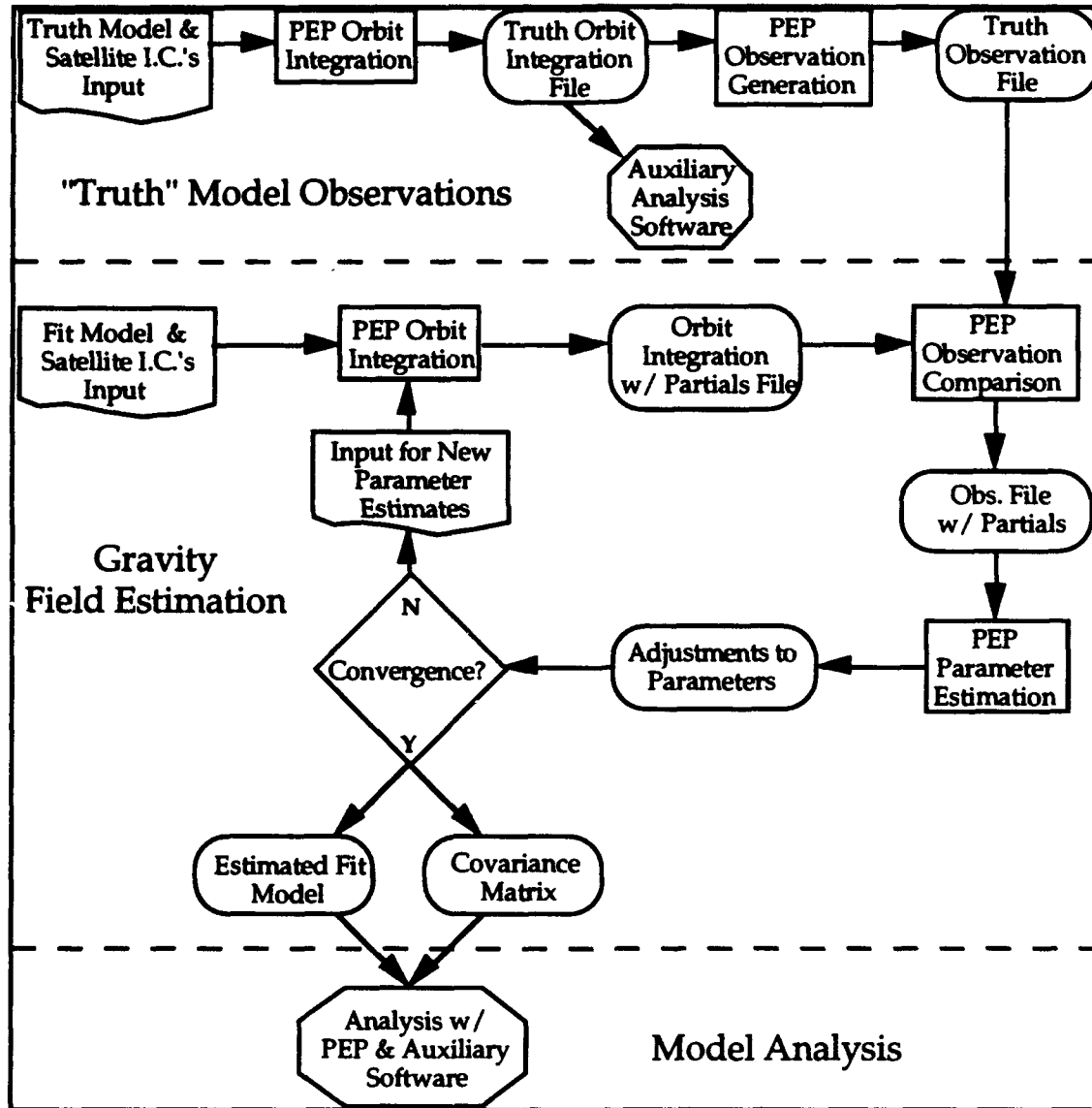


Figure 6.1-1: Flow Diagram for Gravity Sensing Mission Simulations

and partial derivatives, the parameter estimation module formed and solved the normal equations to calculate the adjustments to the parameters,  $\Delta\tilde{\alpha}$ . The size of the parameter adjustments and their uncertainties determined if



the process had converged. If the process had not converged, the new parameters were used to propagate the next iteration's orbit and the process was repeated. The maximum likelihood parameter estimates and the covariance matrix ( $A^{-1}$ ) were written to output files when the process finally converged. These files were then used to analyze the estimated gravitational model and its ability to predict future lunar missions.

Although this process is straight-forward, it is a very time and computer memory intensive process. A typical 14 day orbit propagation for an  $8 \times 8$  spherical harmonic gravity field with partials calculated for 79 parameters typically took over eight hours on a Sun Sparcstation IPC. Also, due to the high correlations between gravitational parameters, it was not unusual for a run with different "truth" and fit models to require at least fifteen iterations to converge upon a solution. The convergence criterion, perhaps unnecessarily stringent, required the adjustments to be less than 1% of the parameter uncertainties.

## **6.2 Fifth Degree Harmonic Truth and Fit Model Test Case**

Since PEP was modified to include lunar mascons and expand the degree and order spherical harmonic expansions allowable, several test cases were run to ensure that PEP-D's modules were operating correctly. The first set of tests involved the attempt to estimate a  $5 \times 5$  spherical harmonic expansion fit model for observations generated with a  $5 \times 5$  spherical harmonic expansion truth model. Since the degree and order of the estimated fit and truth models were the same, this test was expected to be a good warm-up exercise for future runs.

For these tests, a single lunar polar 200 km altitude near-circular satellite orbit was numerically integrated for twenty-eight days. The initial selenographic orbital elements are listed in Table 6.2-1, where elements in parentheses are in PEP's internal units (angles referred to the mean equinox and equator of the earth of 1950.0). A zero degree initial mean anomaly was selected first, placing the satellite directly over the lunar north pole. Due to a singularity in PEP's algorithm for the central body harmonic effects, it could

## LUNAR GRAVITATIONAL FIELD ESTIMATION AND SATELLITE ORBIT PREDICTION

not propagate this orbit. Because of perturbation forces, it would be highly unlikely that this condition would be repeated during the middle of an orbit propagation. The mean anomaly was adjusted one degree and the process restarted with no further difficulties.

Table 6.2-1: Satellite Initial Conditions for 5 X 5 Spherical Harmonic Test Case

$a_0$	1938 km ( $1.295472995 \times 10^{-5}$ AU)
$e_0$	0.05
$i_0$	90° (103.1048493849350°)
$\Omega_0$	90° (304.1996805394721°)
$\omega_0$	90° (72.2394269798987°)
$M_0$	1°

The starting time for the orbit integration was 16 May 1968 or Julian Date 2,440,001.5 0 hour Coordinate Time. This initial epoch was selected over an epoch in 1996 or 1997, when a lunar gravitational sensing mission might occur, because it is near the beginning of the n-body file supplied by the SAO. This file is read and interpolated from during the integration and observation modules, so computer time was saved by selecting an initial epoch near the beginning of the file. Other than saving computer time, the choice of initial epoch should not effect the simulations of this thesis.

The lunar satellite's orbit was propagated using the first five degree and order coefficients from the 1980 Bills and Ferrari 16 X 16 lunar spherical harmonic model [12]. These coefficients are given in Table 6.2-2. The central body attraction of the moon and the perturbing attractions of the earth and sun were included in the Adams-Moulton numerical integration with a step size of  $2^{-14}$  day. This allowed approximately 1,451 steps per 2.125504 hour orbit. This was an extremely small step size to characterize fifth degree and order harmonics and ensure numerical stability in the integration of motion.

The observation module then created Doppler observations of the satellite from NASA DSN's Goldstone site every minute. Four different observation scenarios were generated for this test case. Two involved range and Doppler observations and two involved Doppler observations only. In two cases observations were occulted by the moon and in the other two cases the observations continued through a fictitious "transparent" moon.

Table 6.2-2: 5 X 5 Spherical Harmonic Truth Model Coefficients

Harmonic	$\times 10^{-6}$	Harmonic	$\times 10^{-6}$
$J_2$	202.431	$\bar{S}_{21}$	-0.00
$\bar{C}_{21}$	-0.07	$\bar{S}_{22}$	0.03
$\bar{C}_{22}$	34.49		
$J_3$	8.8897	$\bar{S}_{31}$	6.63
$\bar{C}_{31}$	21.96	$\bar{S}_{32}$	4.76
$\bar{C}_{32}$	14.14	$\bar{S}_{33}$	-2.45
$\bar{C}_{33}$	15.87		
$J_4$	-11.73	$\bar{S}_{41}$	1.91
$\bar{C}_{41}$	-4.82	$\bar{S}_{42}$	-6.76
$\bar{C}_{42}$	-8.13	$\bar{S}_{43}$	-14.43
$\bar{C}_{43}$	0.48	$\bar{S}_{44}$	-0.55
$\bar{C}_{44}$	-3.50		
$J_5$	2.388	$\bar{S}_{51}$	-1.53
$\bar{C}_{51}$	-9.66	$\bar{S}_{52}$	-2.35
$\bar{C}_{52}$	3.71	$\bar{S}_{53}$	4.91
$\bar{C}_{53}$	-0.39	$\bar{S}_{54}$	-6.58
$\bar{C}_{54}$	0.56	$\bar{S}_{55}$	11.60
$\bar{C}_{55}$	-6.69		

The initial test cases recreated the measurements of the Lunar Orbiter missions (Section 1.3). The orbits were selected to simulate orbits proposed for the Lunar Observer or Lunar Scout missions [16, 25, 39]. The observation scheme, duplicating the processing of Lunar Orbiter data, used the DSN S-band frequency (2.115 GHz) for collecting Doppler range rate observations for sixty-second intervals. No transponder frequency translation was simulated. These observations had a quoted accuracy of 1 mm/sec [29], which is the accuracy achievable for integer Doppler counts over the sixty-second interval. Range observations were also generated in the "truth" model observation file. When fitting to only Doppler observations, the range observations were given negative error weights so that they would be ignored in the estimation process. The two way range measurement was included on the same signal used for the Doppler observable and had a three meter accuracy. This accuracy is based upon the ability to detect a 20 nanosecond time delay for a two-way phase shift keyed code.

## LUNAR GRAVITATIONAL FIELD ESTIMATION AND SATELLITE ORBIT PREDICTION

Over the twenty-eight day observation period, the satellite would orbit over the entire lunar surface as the moon rotated under its orbital plane. Due to the extremely conservative integration step size, the twenty-eight day viewing period, and the calculation of partials, these initial test cases quickly filled up the available disk space, resulting in a system crash. Reevaluating the simulation requirements, the observation period was reduced to fourteen days, which still provides complete lunar coverage in either an ascending or descending pass.

After the "true" observations were generated, the satellite initial conditions and thirty-two lunar harmonic coefficients were perturbed to provide the first guess for the estimation process. Each gravitational harmonic coefficient's absolute value was increased by  $1.0 \times 10^{-7}$ . The orbital initial conditions were altered by the values given in Table 6.2-3. The satellite orbit was then numerically integrated along with partial derivatives.

Table 6.2-3: Perturbed Satellite Initial Conditions for Estimation Model

$\delta a$	149.6 km ( $1.0 \times 10^{-11}$ AU)
$\delta e$	$1.0 \times 10^{-5}$
$\delta i$	$-1.0 \times 10^{-4}^\circ$
$\delta \Omega$	$-1.0 \times 10^{-4}^\circ$
$\delta \omega$	$-1.0 \times 10^{-4}^\circ$
$\delta M_0$	$1.0 \times 10^{-4}^\circ$

These tests were run using saved partial derivatives of motion. Using this feature, partial derivatives were calculated during the first iteration step and these saved partials of motion were used to determine the partial derivatives of observations on subsequent iterations. Computation time was saved by not recalculating the partials on each iteration. This approach worked well for test cases with the same "truth" and fit models, but was not effective on other simulations. In general, this feature is very effective when the process is close to convergence.

The fitting process revealed that all of the harmonic terms included in the equations of motion have to be included in the partial derivative calculations. By default, PEP was only calculating the second degree harmonic effects upon the partials. This provides sufficient accuracy for earth satellites

where the  $J_2$  effect dominates motion, but it was not sufficient for lunar satellites. Additionally, the first scenario's slow convergence raised concerns about the choice of initial osculating orbital elements. For a circular orbit, the argument of perilune ( $\omega$ ) is undefined. For the near-circular orbit, the perilune position was very difficult to determine. The argument of perilune and mean anomaly were difficult to estimate because of their high correlation. PEP software does not currently use equinoctial orbital elements [ $e \sin(\Omega + \omega)$ ,  $e \cos(\Omega + \omega)$ ], but it provides the option of replacing the  $\Omega$ ,  $\omega$ , and  $M$  orbital elements with the sum of the angle elements  $\Omega$ ,  $\Omega + \omega$ ,  $\Omega + \omega + M$ . After the initial orbital elements were converted to this form, their correlations were reduced and the parameter estimation routine had no difficulty estimating these parameters.

After overcoming the previously mentioned difficulties, the simulations converged in three iterations for all four scenarios. After these test cases, a fifth scenario was run in which radar biases for the time delay and Doppler shift observations were estimated along with the gravitational parameters and satellite initial conditions. This scenario evaluated the estimation procedure's ability to handle measurement bias estimates and also converged in three iterations.

### **6.2.1 Scenario One: No Occultation, Range and Range Rate**

The first scenario calculated a spherical harmonic fit model based on 20,156 time delay (range) and 20,156 Doppler shift (range rate) observations over the fourteen day period. Observations were processed every sixty seconds for the entire period since there were no horizon or occultation restrictions. The thirty-two gravitational harmonic coefficients and six initial conditions were all estimated within approximately ten digits of accuracy for each parameter (six digits for angular initial conditions). The observation residuals divided by the assumed measurement errors, referred to as the non-dimensional "fit residuals", had a root mean square (rms) value of  $7.45263 \times 10^{-4}$ , essentially zero. The theoretical rms for these cases is zero, as opposed to the value of one mentioned in Section 5.2 because the "true" observations were exact (without measurement noise) and the truth and fit models are of the same degree and order. The run also calculated correlations as high as

-0.998 between the  $\bar{C}_{33}$  and  $\bar{C}_{53}$  coefficients and  $\bar{S}_{32}$  and  $\bar{S}_{52}$  coefficients. Fifteen of the 703 correlations were greater in magnitude than 0.95. Initially, these high parameter correlations seemed as if they were due to a resonance in a particular harmonic frequency, but later fits to higher degree models also demonstrated high correlations for the higher degree terms.

### **6.2.2 Scenario Two: No Occultation, Range Rate**

This scenario excluded the 20,156 time delay (range) observations from the previous run's fourteen day period in its estimation of the spherical harmonic fit model. Once again the thirty-eight parameters were all estimated with approximately ten digits of accuracy and the fit residuals were essentially zero, with an rms value of  $8.83418 \times 10^{-4}$ . The highest parameter correlation was again -0.998 between  $\bar{C}_{33}$  and  $\bar{C}_{53}$ . The  $\bar{S}_{33}\bar{S}_{53}$  and  $\bar{S}_{32}\bar{S}_{52}$  correlations were the second highest at -0.997. The  $\bar{S}_{33}$  and  $\bar{S}_{53}$  correlation was up from -0.996 in the previous scenario. Once again fifteen of the 703 correlations were greater in magnitude than 0.95.

### **6.2.3 Scenario Three: Occultation, Range and Range Rate**

After the previous scenarios were completed, the "truth" model observations were recreated with lunar occultations. This third scenario then calculated its fit model based upon 15,672 time delay (range) and 15,672 Doppler shift (range rate) observations over the fourteen day period. Lunar occultations eliminated 3 days, 2 hours and 44 minutes of observations over the fourteen day period. Again the thirty-eight parameters were estimated to within ten digits accuracy of their "true" values. With the reduced observability, fit residuals increased, having an rms value of  $2.54901 \times 10^{-3}$ . Although these residuals are larger, the fit model is still essentially exact. The parameter correlations for this scenario essentially repeat those of the first scenario with the  $\bar{C}_{33}\bar{C}_{53}$  and  $\bar{S}_{32}\bar{S}_{52}$  coefficients having the highest correlation (-0.998). As in both previous cases, fifteen of the 703 correlations were greater than 0.95.

#### **6.2.4 Scenario Four: Occultation, Range Rate**

This scenario excluded the 15,672 time delay (range) observations from the previous run in its estimation of the gravitational coefficients and orbital initial conditions. The scenario's fit model agreed with the truth model to about nine places. The fit residuals for this scenario were up from the previous scenario with an rms value of  $6.86066 \times 10^{-3}$ . The highest parameter correlation was the  $\bar{C}_{33}\bar{C}_{53}$  correlation (-0.999). The  $\bar{S}_{32}\bar{S}_{52}$  and  $\bar{S}_{33}\bar{S}_{53}$  correlations were once again close behind (-0.998). As before, fifteen of the 703 correlations were greater than 0.95.

#### **6.2.5 Scenario Five: Occultation, Range and Range Rate with Biases**

This scenario used the 15,672 time delay (range) and 15,672 Doppler shift (range rate) observations from the third scenario and attempted to estimate the thirty-two gravitational harmonic coefficients and six orbital initial conditions as well as measurement biases for the time delay and Doppler shift observations. This scenario estimated the gravitational coefficients and initial conditions with about nine places of accuracy. Additionally it estimated a  $1.43121 \times 10^{-9}$  second time delay bias and a  $-4.37639 \times 10^{-9}$  Hz Doppler shift bias. No biases were included in the observations and this run essentially estimated zero biases. The fit residuals were lower than the fourth scenario's with an rms value of  $6.10319 \times 10^{-3}$ , also essentially zero. The  $\bar{C}_{33}$  and  $\bar{C}_{53}$  coefficients once again had a -0.999 correlation with the  $\bar{S}_{32}\bar{S}_{52}$  and  $\bar{S}_{33}\bar{S}_{53}$  parameters yielding the second highest correlations (-0.998). Fifteen of the 780 correlations were greater than 0.95.

### **6.3 Earth-Based Doppler Observable Mascon Test Cases**

The second set of tests included two small mascons in the truth model and increased the degree of the spherical harmonic fit model. This test case was run to determine whether PEP-D could estimate a spherical harmonic model based on observations with a different truth model and to determine

## LUNAR GRAVITATIONAL FIELD ESTIMATION AND SATELLITE ORBIT PREDICTION

whether the sensing geometry affected the estimate's ability to model the lunar gravitational field.

For the first scenario, the previous  $5 \times 5$  spherical harmonic expansion (Table 6.2-2) was augmented with two mascons of equal strength placed at the limbs of the moon on the equator. For the second scenario, the  $5 \times 5$  model was augmented with mascons of equal strength placed on the front and back faces of the moon, still at the equator. Mascons were included in pairs to preserve the center of mass of the moon and avoid solving for first degree harmonic coefficients. The strongest surface disk estimated in the Wong model [47] was selected for the strength of these mascons whose strengths and locations are listed in Table 6.3-1.

Table 6.3-1: Mascon Test Case - Mascon Placement

	Mascon on Limb		Mascon on Face	
	1	2	1	2
$m_i$	$7.212 \times 10^{-6}$	$7.212 \times 10^{-6}$	$7.212 \times 10^{-6}$	$7.212 \times 10^{-6}$
$r_i$	1680 km	1680 km	1680 km	1680 km
$\theta_i$	90.0°	270.0°	0.0°	180.0°
$\phi_i$	0.0°	0.0°	0.0°	0.0°

The same lunar polar 200 km altitude near-circular satellite orbit was numerically integrated for fourteen days over these two lunar gravitational fields. For both cases, the orbit integration was once again started on 16 May 1968 and used the same satellite initial conditions as in the previous tests (Table 6.2-1). The lunar polar satellite's motion was detected by the same earth-based Doppler shifted observables used for the previous tests. Observations were again interrupted by lunar occultations. To reduce the size of the computer files generated in the simulation, the Doppler count interval was changed from sixty seconds to one hundred and twenty seconds.

These tests were run to determine whether earth observations are sufficient to estimate the lunar gravitational field despite the mascons' location. Mascons cause radial disturbing accelerations as satellites pass over them and Doppler observations sense relative velocity along the line-of-sight. Doppler observations should therefore have an easier time sensing mascon disturbances when the observing site, observed body, and mascon are all aligned. These two lunar mascon scenarios present two geometrical extremes



for Doppler sensing. In the first case, the disturbing acceleration due to passage over a mascon on the limb is orthogonal to the Doppler line-of-sight. In the second case, the disturbing acceleration and Doppler line-of-sight are aligned as the orbiting satellite passes over the near face's mascon.

These test cases were initially run using the saved partials feature of PEP mentioned in Section 6.2. For the first scenario full partials were recalculated on the fifth iteration and the parameters converged on the ninth iteration. The parameters from this solution were then run with full partials and they required six more iterations to converge. For the second scenario, the first five iterations were run using the saved partials feature since the "semi-convergence" of the previous case had not been discovered. After the fifth iteration, the saved partials feature was abandoned and this scenario also required fifteen total iterations to converge.

The mascon test cases, requiring fifteen iterations to converge, demonstrated the difficulty of estimating gravitational parameters when the "truth" and fit models differed. Additionally, these scenarios revealed the limitations of PEP's saved partials feature. Since it was not clear that saved partials were helping the estimation process, the method was abandoned. This significantly increased the amount of computer time and the size of the memory files required for the simulation process.

### **6.3.1 Scenario One: Limb Mascons**

As mentioned previously, this scenario converged in fifteen iterations to a degree and order eight spherical harmonic model. Appendix E's Table E-1 lists the estimated harmonic coefficients for this fit model. Additionally this run estimated the satellite osculating orbital initial conditions. Table 6.3.1-1 compares the true initial conditions with their estimated values.

The fit residuals (observation residuals divided by assumed measurement noise) for this model have an rms of 7.36725. For the first time this non-dimensional statistic, which measures how well the estimated model agrees with the observed behavior, is greater than one. This shows that this spherical harmonic model is inefficient at modeling a gravitational field with mascon anomalies. An analysis of the parameter correlations

## LUNAR GRAVITATIONAL FIELD ESTIMATION AND SATELLITE ORBIT PREDICTION

reveals that four pairs of correlations have cross correlations greater than -0.999:  $\bar{S}_{66}\bar{S}_{86}$ ,  $\bar{C}_{66}\bar{C}_{86}$ ,  $\bar{C}_{55}\bar{C}_{75}$ , and  $\bar{S}_{55}\bar{S}_{75}$ . The  $\bar{C}_{54}\bar{C}_{74}$  and  $\bar{S}_{54}\bar{S}_{74}$  correlations also had an extremely high correlation of -0.989. Twenty-two of the 3,403 correlations were greater in magnitude than 0.90 with nine of these greater than 0.95. These correlations for the same 200 km lunar polar orbiter provided an indication that the high parameter correlations discovered in Section 6.2 were not due to the resonance of a particular harmonic frequency.

Table 6.3.1-1: Limb Mascon Orbital Initial Condition Estimates

	"True"	Fit	$\Delta$
$a_0$	1938.0 km	1938.1106 km	110.6 meters
$e_0$	0.05	0.050091	0.000091
$i_0$	103.1048°	103.1067°	0.0019°
$\Omega_0$	304.1997°	304.1939°	-0.0058°
$(\Omega+\omega)_0$	16.4391°	16.6468°	0.2077°
$(\Omega+\omega+M)_0$	17.4391°	17.6389°	0.1998°

### 6.3.2 Scenario Two: Face Mascons

This scenario fit the observed behavior to an  $8 \times 8$  spherical harmonic expansion in fifteen iterations. Table E-2 in Appendix E lists the estimated harmonic coefficients for this fit model. This run also estimated the satellite orbital initial conditions for the observed lunar satellite. Table 6.3.2-1 compares the true initial conditions with the estimated initial conditions.

This case's non-dimensional fit residuals had a root mean square of 11.8025, once again an order of magnitude greater than desired for an estimated model. The increase in the residuals' rms over the previous scenario is most likely due to the lack of observations for the far-side mascon. The Doppler observations in this scenario sense the radial accelerations due to the mascon on the near face but cannot account for the lunar far-side perturbations with the  $8 \times 8$  spherical harmonic expansion. In the previous case, since the mascon disturbing accelerations were orthogonal to the

Doppler line-of-sight, the observations did not sense large disturbances and had an easier time fitting the small disturbances to the fit model.

An analysis of the parameter correlations once again reveals that four pairs of correlations are greater than -0.998:  $\bar{S}_{66}\bar{S}_{86}$ ,  $\bar{C}_{66}\bar{C}_{86}$ ,  $\bar{C}_{55}\bar{C}_{75}$ , and  $\bar{S}_{55}\bar{S}_{75}$ . The  $\bar{C}_{54}\bar{C}_{74}$  and  $\bar{S}_{54}\bar{S}_{74}$  correlations are again very highly correlated at -0.989 and -0.988 respectively. Of the 3,403 correlations, nineteen were greater in magnitude than 0.90 and nine of these were greater than 0.95.

Table 6.3.2-1: Face Mascon Orbital Initial Condition Estimates

	"True"	Fit	$\Delta$
$a_0$	1938.0 km	1937.9781 km	-21.9 meters
$e_0$	0.05	0.049956	-0.000044
$i_0$	103.1047°	103.1015°	-0.0032°
$\Omega_0$	304.1997°	304.2022°	0.0025°
$(\Omega+\omega)_0$	16.4391°	16.3311°	-0.1080°
$(\Omega+\omega+M)_0$	17.4391°	17.3624°	-0.0767°

## 6.4 Truth Model Development

Since the true lunar gravitational field is not precisely known, a lunar gravitational "truth" model was developed for this thesis. This truth model was then used to evaluate various proposed lunar gravitational sensing schemes. Previous lunar missions have discovered mascons on the near side of the moon [35]. There is no conclusive evidence regarding mascons on the far side of the moon, since there are no observations of a satellite's motion over the far side. For this thesis' truth model, mascons were placed on both the near and far sides. These mascons augmented the previously used 5 x 5 spherical harmonic expansion (Table 6.2-2).

From their surface layer representation of the lunar gravitational field, Wong et. al. identified major lunar mass anomalies with their selenographic

features [47 Table 2]. Wong's group modeled the lunar gravitational field with 50 km radii surface disks distributed around the lunar surface (Section 2.3.2). Each surface feature was therefore represented by several disks depending upon the size of the feature. The seven most influential mass anomalies, requiring forty-nine surface disks, were selected for the truth model's near-side mascons. Since PEP-D does not model mascons as surface disks, these forty-nine disks were converted to point masses placed 58 km below the lunar surface. The selenographic positions and strengths of the 600 surface disks [47 Figure 4 and Table 6] were then correlated with topographic and gravitational maps depicting the major surface features [26] to determine the forty-nine point masses required for the "truth" model.

Since all of the previously identified mascons are on the near side, there was no scientific basis for establishing lunar far-side mascons. For this thesis, far-side mascons were developed to meet two requirements. First, they should be difficult to detect from earth-based observations, and secondly they should not alter the lunar center of mass. Since a mascon placed on the back face of the moon would be the most difficult to sense, the first far-side mascon was centered at  $180^\circ$  longitude and  $0^\circ$  latitude. Masses comparable to the near-side mass anomalies were selected for these point masses. Since lines of longitude are more widely spaced at the equator and nineteen point masses were used, this mascon is the largest and strongest of any mass anomaly in the truth model.

The translation of the lunar center of mass determined the placement of the second far-side mascon. This balancing mascon was composed of seven point masses centered on  $214.5^\circ$  longitude and  $-48.0^\circ$  latitude. After these two far-side mascons were added to the near-side mascons, the center of mass was still askew, so an additional point mass added to the model. The entire gravitational truth model is contained in Appendix D.

The lunar polar 200 km altitude orbit used in the two previous test cases was then numerically integrated for twenty-eight days with this lunar gravitational truth model. The satellite orbit was then converted to selenographic orbital elements and plotted to determine whether the mascons had drastically altered the lunar gravitational field. The plots revealed that the mascons affected the satellite when it was in the prime

meridian plane, seven and twenty-one days into the orbit propagation. At this point, the instantaneous semi-major axis increases noticeably. The lunar altitude, however, never drops below 100 km over the integration period. The lunar altitude for this orbiter oscillates between 100 - 300 km. When numerically integrated without mascons, the satellite orbit exhibits the same altitude oscillations, but the semi-major axis does not show the peaks observed in the mascon case. The inclusion of mascons does not affect the orbital inclination and has a limited effect on the variation of eccentricity over the twenty-eight day period. This analysis showed that the addition of mascons to the lunar gravitational field did not detrimentally affect the satellite orbit.

**Table 6.4-1: "Truth" Model Major Mass Anomalies**

Mascon	Strength $\times 10^{-6}$ Lunar Mass	Longitude	Latitude	# of Point Masses
Sea of Rains	22.8	328° - 350°	28° - 48°	11
Sea of Serenity	21.5	8° - 25°	17° - 34°	12
Sea of Crises	9.2	52° - 63°	12° - 23°	7
Sea of Nectar	8.4	27° - 38°	-17° - -19°	6
Seething Bay	4.2	347° - 353°	7° - 13°	4
Sea of Moisture	6.0	318° - 325°	-29° - -22°	3
Smyth's Sea	3.1	82° - 93°	-8° - 3°	6
Subtotal	75.2			49
Difficult to Obs.	40.025	175° - 185°	-8° - 8°	19
Balancing	27.157	212° - 217°	-51° - -45°	7
Point Mass	1.114	217.6°	-63.4	1
Subtotal	68.296			27

### **6.5 Single Orbiter, Earth-Based Doppler Sensing Scheme**

The first sensing scheme evaluated with the lunar gravitational truth model was the earth-based Doppler observation of a single lunar orbiter. This scheme was selected because it was used to obtain the current lunar gravity field models. This scheme's ability or inability to estimate the "true" lunar gravitational field may provide an idea of how well current models represent the real lunar gravity field. The lunar orbiter was placed in a polar near-circular orbit which would provide total lunar surface coverage over the fourteen day observation period. This orbit attempted to recreate the "gravity sensing" satellite's orbit in the Lunar Observer or Scout missions [16, 25, 39].

Since the acceleration due to gravity is larger for low altitude orbits, its disturbances are easier to sense and the lowest possible orbital altitude was desired for this mission. Unfortunately this desire conflicts with the desire to observe undisturbed motion for at least one lunar period. Very low altitude orbits typically require re-boosting to keep them at a safe distance above the lunar surface. Re-boost maneuvers, however, disrupt the estimation procedure by introducing new forces on the orbiting body which are difficult to include in the estimation process. A 100 km altitude polar orbiter was numerically integrated for twenty-eight days. Plots of its selenographic orbital elements revealed that this orbiter barely remained above the lunar surface for the twenty-eight day period. Since this orbiter would require re-boosting during the twenty-eight days, the orbital altitude was increased by 100 km. The 200 km altitude polar orbiter maintained an altitude of 100-300 km over the twenty-eight day period. This satellite orbit was a compromise satisfying both the low-altitude and no re-boost requirements.

#### **6.5.1 Single Orbiter "Truth" Model Observations**

The single polar 200 km altitude lunar orbiter motion was numerically integrated for fourteen days from 16 May 1968 (JD 2,440,001.5) with the satellite initial conditions given below. The orbit was propagated using the Adams-Moulton numerical integration technique with a step size of  $2^{-13}$  day. The integration step size was relaxed from previous cases to save computer disk space, especially when partial derivatives are calculated at each step.

Relaxing the integration step size still provided over 725 steps per 2.125504 hour orbit, more than required for numerical stability and adequate for the characterization of an eighth degree and order harmonic fit model.

Over this fourteen day period, Doppler observations of the lunar orbiter were processed every sixty seconds, except during lunar occultations, from the DSN Goldstone station using the S-Band frequency (2.115 GHz). Transponder frequency translation was not simulated and no horizon constraints were imposed. A 14 mHz accuracy was assumed for the Doppler observations, roughly equivalent to the quoted 1 mm/sec range rate accuracy for sixty second intervals [29]. The simulations of this mission produced 15,695 Doppler shift observations over the fourteen day period.

Table 6.5.1-1: Satellite Initial Conditions for "Truth" Model Observations

$a_0$	1938 km ( $1.295472995 \times 10^{-5}$ AU)
$e_0$	0.05
$i_0$	90° (103.1048493849350°)
$\Omega_0$	90° (304.1996805394721°)
$\omega_0$	90° (72.2394269798987°)
$M_0$	1°

### 6.5.2 Eighth Degree and Order Fit

The first estimation run attempted to fit the observations to an 8 x 8 spherical harmonic expansion. The final iteration of the limb mascon test case provided the initial guess of parameters and initial conditions for this case's iterations. This saved computer time since both cases were based on observations of the same polar orbiter and the limb mascon case had already integrated the satellite's motion with partial derivatives.

Due to the significant difference between the model used to generate the "true" observations and the fit model, this case required twenty-five iterations to converge upon a solution. The estimated harmonic coefficients for the fit model are listed in Table E-3 in Appendix E. The simulation also estimated the satellite orbit's initial conditions and Table 6.5.2-1 compares the true initial conditions with their estimated values.

## LUNAR GRAVITATIONAL FIELD ESTIMATION AND SATELLITE ORBIT PREDICTION

The observation residuals divided by the assumed measurement errors, referred to as the non-dimensional "fit residuals", had a root mean square value of 365.954 for this model. This is over thirty times larger than the Face Mascon test case and is a further indication of the  $8 \times 8$  spherical harmonic expansion's inability to fit the observed satellite's motion. Eighteen of the 3,403 parameter correlations were greater in magnitude than 0.90 and nine of these were greater than 0.95. Four pairs of correlations ( $\bar{C}_{55}\bar{C}_{75}$ ,  $\bar{S}_{66}\bar{S}_{86}$ ,  $\bar{C}_{66}\bar{C}_{86}$ , and  $\bar{S}_{55}\bar{S}_{75}$ ) were greater than -0.998 and two pairs ( $\bar{S}_{54}\bar{S}_{74}$  and  $\bar{C}_{54}\bar{C}_{74}$ ) were greater than -0.988.

Table 6.5.2-1:  $8 \times 8$  Single Orbiter Initial Condition Estimates

	"True"	Fit	$\Delta$
$a_0$	1938.0 km	1938.1154 km	115.4 meters
$e_0$	0.05	0.047811	-0.002189
$i_0$	103.1048°	103.0998°	-0.0050°
$\Omega_0$	304.1997°	304.1957°	0.0040°
$(\Omega+\omega)_0$	16.4391°	15.9600°	-0.4791°
$(\Omega+\omega+M)_0$	17.4391°	17.3912°	-0.0479°

### 6.5.3 Twelfth Degree and Order Fit

The estimated gravity model's fit residuals show that the  $8 \times 8$  spherical harmonic expansion was not a close fit to the observed behavior. Mascons in the truth model result in very high frequency gravitational behavior in the local area (Section 2.3). Since the spherical harmonic expansion requires higher degree and order expansions to model this high frequency behavior, a fit to a  $12 \times 12$  spherical harmonic model was attempted.

For the initial parameter guesses, estimates from the  $8 \times 8$  fit model were used and all of the new coefficients (ninth through twelfth degrees) were set to zero. The satellite initial condition estimates for the  $8 \times 8$  fit, used for the  $12 \times 12$  fit's initial iteration, are listed in Table 6.5.3-1. The same "truth" model observations used in the  $8 \times 8$  fit were used for this fit.



## Chapter Six: Orbit Fitting and Gravity Estimation

Since the fit model was increased to twelfth degree and order, the numerical integration step size was reduced to  $2^{-14}$  days. The step size was changed to sample the higher degree harmonic effects more often with 1,451 steps per 2.125504 hour orbit. With the change in step size and dramatically increased number of estimation parameters and parameter partials, the numerical integration required approximately 23 hours to propagate the satellite's motion and partial derivatives for fourteen days.

Table 6.5.3-1: 12 X 12 Fit Initial Guesses for Satellite Initial Conditions

$a_0$	$1.29555011876471 \times 10^{-5}$ AU
$e_0$	0.0478107828679364
$i_0$	103.099831198443°
$\Omega_0$	304.195650955435°
$(\Omega + \omega)_0$	15.9599887633931°
$(\Omega + \omega + M)_0$	17.3911644150588°

On the fitting process' second iteration several of the parameter adjustments were an order of magnitude larger than their previous estimate. These estimates were used to propagate the next iteration's orbit, resulting in increased residuals and even larger parameter adjustments. By the fifth iteration, the normal equations could not be solved because 152 of the 171 diagonal elements in the coefficient matrix (A) were negative. Since the normal equations could not be inverted, the fitting process was abandoned.

Table 6.5.3-2: 12 X 12 Spherical Harmonic Fit Progression

Iteration	Pre-adjustment RMS Residual	Predicted RMS Residual
1	365.954	112.113
2	10,433.0	99.5596
3	42,590.9	192.212
4	106,490	1,999.54
5	760,314,000	16,484,700

Table 6.5.3-2 shows how the parameter adjustments kept leading the process further and further from a solution. The fitting process started with observation residuals divided by the assumed measurement errors with a root mean square value of 366. After solving the normal equations, PEP

predicted a non-dimensional rms residual of 112. The predicted residual is the computed pre-adjustment residual less the sum of the observable partial derivatives times the parameter adjustments. Instead of reducing the residuals by a third, the new parameter estimates produced residuals with a non-dimensional rms almost thirty times greater than in the previous iteration! Unfortunately instead of making it easier to fit to the observed lunar orbiter motion, increasing the degree and order of the spherical harmonic model made it more difficult to solve the normal equations and converge upon a fit solution. This may have occurred because of the limited observability of lunar far-side motion and high parameter correlations.

### **6.6 Tenth Degree Harmonic Truth and Fit Model Test Case**

After the previous convergence difficulties, a test was run to estimate a  $10 \times 10$  spherical harmonic expansion for observations generated with the same degree and order truth model. Since the previous case was the first attempt to fit to harmonic expansions higher than eighth degree and order, this test would verify whether or not the difficulties encountered were due to the estimation program or the spherical harmonic expansion's ability to fit to the observed behavior.

The same lunar polar 200 km altitude near-circular orbit used in previous runs was used to generate Doppler "truth" observations with 1 mm/sec accuracy. This orbit, again integrated for fourteen days from 16 May 1968, used the orbital initial conditions listed in Table 6.2-1 and a  $10 \times 10$  spherical harmonic lunar gravity truth model. This truth model used the 1980 Bills and Ferrari coefficients [12] for the initial five degrees (Table 6-2.2). Gravitational coefficients developed at JPL by Alex Konopliv for his  $50 \times 50$  spherical harmonic expansion were used for the sixth through tenth degree harmonic coefficients [27], because the Bills and Ferrari coefficients [12] were not manually entered into the PEP input stream. The coefficients used are listed in Table E-4 in Appendix E.

After generating the "truth" model observations, the satellite initial conditions and one hundred and seventeen lunar harmonic coefficients were

perturbed to provide the first guess for the estimation process. As in the previous fit to a pure harmonic truth test case, each gravitational harmonic coefficient's absolute value was increased by  $1.0 \times 10^{-7}$  and the orbital initial conditions were perturbed by the values given in Table 6.2-3. The satellite orbit was then numerically integrated with partial derivatives.

In the first iteration the pre-adjustment observations residuals divided by the assumed measurement error had a root mean square value of 715,121! As a result, the calculated parameter adjustments were orders of magnitude larger than the guessed parameters. After the first iteration, the lunar orbiter eccentricity grew from 0.05001 to 0.24325 and the semi-major axis was increased by 532 km. These initial conditions were then propagated to create the next iteration's observations. In the second iteration, the normal equations could not be solved because 51 of the 123 diagonal elements in the coefficient matrix (A) were negative. Once again since the normal equations could not be inverted, the estimation process was abandoned. Rather than converging upon a solution, Table 6.6-1 demonstrates how quickly the process diverged.

**Table 6.6-1: 10 X 10 Spherical Harmonic Fit Progression**

<b>Iteration</b>	<b>Pre-adjustment RMS Residual</b>	<b>Predicted RMS Residual</b>
<b>1</b>	<b>715,121</b>	<b>248,467</b>
<b>2</b>	<b><math>3.20623 \times 10^{10}</math></b>	<b><math>2.11726 \times 10^7</math></b>

Since the previous test case (Section 6.2) encountered difficulty when an incomplete set of harmonic coefficients were used to generate partial derivatives of the satellite motion, this cases' observation partial derivatives were checked using a finite difference method (Section 3.4.4). This check verified that the observation partials were correct.

Since the estimation software was operating properly, the gravitational model's sensitivity to initial guesses seemed to cause the convergence difficulties. Apparently the initial guesses resulted in theoretical observation values so different from the observed behavior that correct parameter adjustments could not be determined. Since the estimation of higher degree and order expansion fit models is extremely sensitive to the initial parameter

## **LUNAR GRAVITATIONAL FIELD ESTIMATION AND SATELLITE ORBIT PREDICTION**

guesses, fit models above eighth degree and order were not attempted for the remainder of this thesis' simulations.

Smaller parameter adjustments from iteration to iteration could help the process converge. Incorporating a priori estimates of the lunar gravitational field and their uncertainties would reduce the size of the parameter adjustments (see Section 5.1.4). Smaller parameter adjustments could also be used by under-weighting the calculated adjustments, i.e. only adjusting the initial guesses by 2/3 of the calculated adjustment on the first iteration, etc. Convergence could also be aided by first estimating an  $8 \times 8$ , then a  $9 \times 9$ , and then a  $10 \times 10$  degree and order fit model to the observed behavior, using the estimates from one model as initial guesses for the next higher degree model.

### **6.7 Dual Orbiter, Bent Pipe Doppler Sensing Scheme**

The next sensing scheme evaluated with the lunar gravitational "truth" model featured two lunar satellites and the simulation of a bent pipe Doppler sensing scheme between earth-based sites and the two satellites. This sensing scheme was selected since it is one of the schemes being considered by NASA for future lunar gravitational sensing missions.

This sensing scheme uses a low altitude circular polar "gravity sensing" satellite. A coplanar elliptical "viewing" satellite makes lunar far-side observations of the "gravity sensing" satellite's motion [16, 39, 40]. The polar 200 km altitude near-circular lunar orbiter used in previous simulations is once again the "gravity sensing" satellite for this dual orbiter sensing scheme. The satellite initial conditions and numerical integration parameters for this simulation were the same as for the single orbiter, earth-based Doppler observation sensing scheme and are given in Section 6.5. The "viewing" satellite was placed in a 450 km  $\times$  7,000 km altitude elliptical orbit with a 10.06 hour period. This satellite was given the same initial inclination ( $i$ ) and longitude of the ascending node ( $\Omega$ ) as the circular satellite, placing them in the same orbital plane, orbiting the moon in the same direction. With this selection of ascending node, the far side of the moon rotates

underneath the elliptical orbit's apolune during the first fourteen days of orbit propagation. This maximizes the satellite's ability to view the low altitude orbiter's far-side motion.

The argument of perilune was selected to skew the ellipse and bring the orbit's apolune position out of the earth occultation zone (Figure 1.4-1). Keeping the satellite's apolune passage out of the occultation zone increases the time earth-based sites can view the elliptical satellite for bent-pipe measurements as well as data transfers. The long term behavior of the osculating orbital elements was studied to determine this skew direction. Formulas for the doubly averaged effect of the earth upon a lunar orbit revealed that if the initial argument of perilune,  $\omega$ , is in the second or fourth quadrants, the polar orbit's eccentricity will decrease and  $\omega$  will drift to the first or third quadrant [9]. Based upon this analysis and the desire to keep the apolune over the backside of the moon, a perilune angle in the fourth quadrant was selected. The initial selenographic orbital elements for this elliptical satellite are given in Table 6.7-1, with the angle values in parentheses referred to the mean equinox and equator of the earth of 1950.0. These initial conditions were numerically integrated for fourteen days from 16 May 1968 (JD 2,440,001.5) using the Nordsieck variable step size integration technique (Section 3.1). Since the elliptical orbit was newly propagated, its numerical integration file was converted to selenographic orbital elements. Plots of these elements revealed that the orbit was stable and, as predicted, the orbital eccentricity did decrease over the fourteen day period.

Table 6.7-1: Elliptical Satellite Initial Conditions for "Truth" Model Observations

$a_0$	5463 km ( $3.651789462 \times 10^{-5}$ AU)
$e_0$	0.05994874611
$i_0$	90° (103.1048493849350°)
$\Omega_0$	90° (304.1996805394721°)
$\omega_0$	315° (297.2394269798987°)
$M_0$	1°

### **6.7.1 Dual Orbiter "Truth" Model Observations**

The coherent bent pipe observation method (Section 4.2.3) was simulated over the fourteen days the satellites' orbits were propagated. One two-way coherent Doppler loop processed observations between the DSN Goldstone site and the elliptical satellite. Simultaneously, the elliptical satellite generated two-way coherent Doppler observations of the low-altitude orbiter. Although the coherent bent pipe scheme would be interrupted if any of the links were occulted, only the individual links in this simulation were interrupted by lunar occultations. In addition to the bent pipe observation simulation, the DSN Goldstone site generated Doppler observations of the near-circular polar satellite during its near-side passes. All of these observations were simulated using the 2.115 GHz S-band frequency with approximately 1 mm/sec range rate accuracy (14 mHz) [29].

Simulating this sensing scheme produced 15,695 earth-based Doppler observations of the circular satellite. Because the elliptical orbit was skewed, 19,699 Doppler observations were generated between it and the DSN station. Over this same period, 10,680 Doppler observations were simulated between the two satellites. Auxiliary software analyzed these observation series and their occultation periods to evaluate the far-side lunar coverage. Over the fourteen days, the low altitude polar orbiter passed behind the moon 114 times. For most of these occultations, the elliptical satellite viewed this far-side passage. The moon blocked the line-of-sight between the two satellites on 49 of these 114 occasions and this blockage usually only affected a portion of the passage. There were only 15 cases in which the line-of-sight to the elliptical satellite was blocked for the entire far-side passage. Since these gaps in observation coverage did not occur for sequential far-side passes, the 46,074 observations should provide excellent visibility into the circular orbiter's motion on the lunar far side.

### **6.7.2 Eighth Degree and Order Fit**

These observations, generated with the lunar gravitational "truth" model, were then fit to an  $8 \times 8$  spherical harmonic expansion representing the moon's gravitational field. The initial conditions for the two satellites

were perturbed from their true values for the initial guess in the fitting process. Table 6.2-3 lists the perturbations which were applied to both the circular and elliptical orbits' initial conditions. The true values of the  $5 \times 5$  spherical harmonic expansion used in the truth model were used as initial guesses for the first five degrees of gravitational coefficients (Table 6.2-2). Gravitational coefficients from Alex Konopliv's  $50 \times 50$  spherical harmonic model of the moon [27] were used for the sixth, seventh, and eighth degree coefficient initial guesses. Table E-4 in Appendix E lists these coefficients.

The iteration fit did not converge upon a solution in its normal sense. With the increased observability of lunar far-side motion, the parameter estimation routine drove the non-dimensional residuals down to a root mean square of 386.462 from an initial 23,763.6 in the first four iterations. Because of the difference between the "truth" and fit models, the estimation routine could not reduce the non-dimensional residual rms below 360 as shown in Table 6.7.2-1. Once again, the predicted residual is the computed pre-adjustment residual minus the sum of the observable partial derivatives times the parameter adjustments.

**Table 6.7.2-1:  $8 \times 8$  Spherical Harmonic Fit Progression,**

<b>Iteration</b>	<b>Pre-adjustment RMS Residual</b>	<b>Predicted RMS Residual</b>
1	23,763.6	817.104
2	2,983.65	437.085
3	1,746.75	383.599
4	386.462	371.811
5	375.229	366.587
6	368.213	363.927
⋮	⋮	⋮
15	361.210	361.015
⋮	⋮	⋮
38	361.099	360.939

Although the estimation routine had minimized the fit residuals, its convergence criteria is based on the ratio of the parameter adjustments to their uncertainties with the assumed measurement errors, and these values remained above the convergence limit of 0.01. Since the convergence

## LUNAR GRAVITATIONAL FIELD ESTIMATION AND SATELLITE ORBIT PREDICTION

criterion did not signal convergence, the estimation iterations continued ad infinitum, slowly reducing the residual rms by hundredths and thousandths. The process was stopped after thirty-eight iterations.

The estimated harmonic coefficients for the fit model are listed in Table E-5 in Appendix E. The simulation also estimated the orbital initial conditions for both of the satellites in the sensing scheme. Tables 6.7.2-2 and 6.7.2-3 compare the true initial conditions with their estimated values.

The estimated model's fit residuals had a root mean square value of 361.099 as listed in Table 6.7.2-1. This is smaller than the root mean square of the residuals achieved with the fit to a single lunar polar orbiter (365.954). The high fit residuals are an indication of the  $8 \times 8$  spherical harmonic expansion's inability to fit the observed motion due to the "true" gravitational field. This dual satellite observation method has significantly reduced some of the high parameter correlations, although the most significant ones still remain. For this fit case fifteen of the 3,916 parameter correlations were greater in magnitude than 0.90 and ten of these were greater than 0.95. As with the previous  $8 \times 8$  spherical harmonic fit, the four highest correlations were among the  $\bar{C}_{55}\bar{C}_{75}$ ,  $\bar{S}_{55}\bar{S}_{75}$ ,  $\bar{S}_{66}\bar{S}_{86}$ , and  $\bar{C}_{66}\bar{C}_{86}$  pairs. Although the correlations between the fifth degree, fifth order and seventh degree, fifth order terms were still greater than -0.998, the other correlations were now reduced to -0.995. The  $\bar{S}_{54}\bar{S}_{74}$  and  $\bar{C}_{54}\bar{C}_{74}$  pairs were again the next highest correlated (-0.988).

Table 6.7.2-2: Circular Orbiter Initial Condition Estimates

	"True"	Fit	$\Delta$
$a_0$	1938.0 km	1937.9401 km	-59.9 meters
$e_0$	0.05	0.049677	-0.000323
$i_0$	103.1048°	103.1033°	-0.0015°
$\Omega_0$	304.1997°	304.1994°	-0.0003°
$(\Omega+\omega)_0$	16.4391°	16.2649°	-0.1742°
$(\Omega+\omega+M)_0$	17.4391°	17.4469°	0.0078°



**Table 6.7.2-3: Elliptical Orbiter Initial Condition Estimates**

	<b>"True"</b>	<b>Fit</b>	<b><math>\Delta</math></b>
<b><math>a_0</math></b>	<b>5463.0 km</b>	<b>5463.6291 km</b>	<b>629.1 m</b>
<b><math>e_0</math></b>	<b>0.599487</b>	<b>0.599573</b>	<b>0.000086</b>
<b><math>i_0</math></b>	<b>103.1048°</b>	<b>103.1068°</b>	<b>0.0020°</b>
<b><math>\Omega_0</math></b>	<b>304.1997°</b>	<b>304.1992°</b>	<b>0.0005°</b>
<b><math>\omega_0</math></b>	<b>297.2394°</b>	<b>297.2542°</b>	<b>0.0148°</b>
<b><math>M_0</math></b>	<b>1.0°</b>	<b>0.9997°</b>	<b>-0.0003°</b>



## Chapter Seven

# Lunar Gravity Field Estimation Analyses

### 7.1 Analysis Techniques

After converging upon a least squares maximum likelihood estimate of gravitational coefficients, the estimated lunar gravity fields were analyzed to compare their ability to estimate the "true" gravity field. Since spaceborne navigation depends on accurately modeling the forces acting on a spacecraft, these analyses focus on the effects of modeling errors on lunar navigation.

The root mean square of the observation residuals does not provide an adequate analysis of the global lunar gravity errors due to mismodeling, since it only considers the areas of the gravity field where observations were made. This underweights the far side of the moon where fewer measurements are taken. In Section 7.2 the global radial accelerations for the estimated fit lunar gravity fields are compared to the "true" lunar radial accelerations. The limb mascon and face mascon estimated fit models are analyzed and the two  $8 \times 8$  spherical harmonic expansion fit models are compared to the lunar gravitational "truth" model developed in Section 6.4.

Next, two different lunar spacecraft mission phases are simulated to evaluate the two estimated fits to the lunar gravitational "truth" model. These analyses show how state errors grow using the estimated gravity field model and are intended to simulate the real-world consequences of planning and executing lunar missions with a mismodeled gravity field.

In Section 7.3 the state uncertainties for a low inclination, low altitude spacecraft orbit are predicted one orbit ahead using the covariance analysis

## **LUNAR GRAVITATIONAL FIELD ESTIMATION AND SATELLITE ORBIT PREDICTION**

described in Section 5.2. Stations tracking a lunar satellite would use this analytical method during far-side passage to predict the spacecraft's state uncertainties upon reemergence from the backside. Since this state uncertainty prediction is based upon a mismodeled lunar gravity field, the predicted uncertainties will not be exact. The "true" state is calculated by numerically integrating the spacecraft orbit using the lunar gravity "truth" model. The difference between the spacecraft's predicted and "true" states is the error. Comparing the "true" state with the predicted states reveals the accuracy of the estimated lunar gravity field.

A lunar landing deorbit maneuver is simulated in Section 7.4. In this analysis the deorbit trajectory from a low inclination circular parking orbit was determined from the estimated lunar gravity field models. The mission was then propagated using the "true" lunar gravity field. Lunar gravity mismodeling resulted in a spacecraft position error by the time the spacecraft reached the lunar altitude for Powered Descent Initiation (PDI), typically about 18 kilometers. In a real lunar mission, the spacecraft would be forced to burn extra propellant in a suboptimal descent trajectory to recover from these errors.

Finally, the high gravitational coefficient correlations encountered in the estimation process are analyzed in Section 7.5. Three different measurement types and orbital orientations are simulated to determine their effect on the correlations. Reducing the coefficient correlations by introducing new observations may permit the process to converge more quickly and estimate a more accurate gravitational model. Additionally, the highest correlations are studied in an attempt to find ways to allow them to be estimated independently.

### **7.2 Global Lunar Radial Acceleration Analysis**

Although the estimation process provides residual statistics, they only provide an idea of how well the estimate fits the observations since the observations are not available over the entire lunar surface. To analyze the fit globally a software program was written to calculate the radial accelerations

for a gravity field model everywhere on a sphere of constant radius. Only the radial accelerations due to gravity harmonics and/or mascons are calculated in this program. These radial accelerations were calculated for fit and truth models for all of the cases estimated in Chapter Six at a lunar altitude of 100 km for grid points spaced every four degrees of selenographic latitude and longitude. Unfortunately, since the commercial graphics package was erroneously plotting lines of constant radial acceleration, contour plots comparing the fit and "truth" models are not currently available.

Based on the calculated radial accelerations, the fit and "truth" models were compared statistically. The radial acceleration errors between the "truth" and fit models were calculated for each grid point. The root mean square error between the two models was then calculated. Because of the even spacing of grid points in selenographic latitude and longitude (chosen for rectangular contour plots), this analysis weights radial acceleration errors more heavily in the polar regions. For the mascon test case this bias does not favor either scenario since the disturbing mascons were placed on the equator. For the two 8 X 8 estimated fit models, the dual orbiter bent pipe estimated fit might have an advantage since the "viewing" satellite observed the "sensing" satellite as it passed over the lunar polar regions. Both models, however, were trying to estimate the same lunar gravity "truth" model, so a comparison of the rss radial acceleration errors is still valid.

### **7.2.1 Limb / Face Mascon Analysis**

Based on the global lunar radial acceleration errors, the face mascon case produced a slightly better estimated gravity field. This case had an rms radial acceleration error at 100 km altitude of 64.7804 milligals. The estimated fit to the limb mascon case had radial acceleration errors with an rms of 66.6636 milligals. This global analysis of the radial accelerations errors reveals that a slightly better lunar gravity field was estimated when the disturbing mascons were aligned with the sensing line-of-sight.

This test case attempted to determine whether the mascon's location and the sensing geometry affected the estimated gravity field. The non-dimensional fit residuals' rms contradicted the global radial acceleration

## **LUNAR GRAVITATIONAL FIELD ESTIMATION AND SATELLITE ORBIT PREDICTION**

analysis. The limb mascon fit model (7.37) resulted in a better fit than the face mascon fit model (11.80). These statistics could be the result of the near-side face mascon causing larger line-of-sight accelerations for the orbiting satellite than the limb mascons produced. These statistics could also result from the measurement's ability to sense the near-side mascon's disturbance or inability to recognize any disturbance from the limb mascons. Unfortunately, this analysis does not indicate which estimated field is better at modeling the radial accelerations in the local vicinity of the mascons. Contour plots of these radial accelerations will demonstrate the fit models' ability to locally model these mascon disturbances.

### **7.2.2 Analysis of the Eighth Degree and Order Fits**

Based on the global lunar radial accelerations errors, the dual orbiter bent pipe sensing scheme produced the best estimated gravity field. This case had an rms radial acceleration error at 100 km altitude of 263.015 milligals. The estimated fit to the single orbiter, earth-based sensing scheme had radial acceleration errors with an rms of 320.073 milligals. The disparity between the two rms values provides a strong indication of the advantage of including lunar far-side observations in the estimation process. These errors also give an indication of how much more difficult it was to estimate a spherical harmonic expansion in the presence of 79 point mass disturbances than it was in the mascon test case with just two point masses.

### **7.3 Single Orbit State Uncertainty Prediction Analysis**

For the next analysis, a low inclination, low altitude lunar satellite orbit was used to analyze the position and velocity errors between the "true" and estimated gravity fields. The lunar gravity field truth model developed in Section 6.4 and the two  $8 \times 8$  spherical harmonic expansion fit models derived from the two different sensing schemes were used for this analysis. A  $15^\circ$  inclination, 100 km lunar altitude satellite orbit was selected for this analysis. The estimated  $8 \times 8$  spherical harmonic fit models and their

coefficient uncertainties were first used to predict the state uncertainties for this orbit. This covariance analysis was performed with both the gravity harmonic coefficient covariance matrix ( $A^{-1}$ ) and this matrix multiplied by the fit residuals' rms ( $\Sigma$ ). Fit residuals, once again, are the observation residuals divided by the assumed measurement errors. This evaluation orbit was then numerically integrated using the "true" lunar gravity field. The state errors between the "true" orbits and those predicted from the two  $8 \times 8$  estimated spherical harmonic models provided a further measure of the two sensing schemes' capabilities and limitations. Furthermore, the predicted uncertainties were compared to the errors to understand the uncertainty prediction accuracy with gravity field modeling errors.

The equations of motion and equations of the partial derivatives of motion with respect to the gravity harmonic coefficients were numerically integrated for one orbit (117.85 minutes) for the two estimated fit models from 16 May 1968 (JD 2,440,001.5 0<sup>h</sup> CT) with the satellite selenographic initial osculating orbital elements listed in Table 7.3-1 (1950.0 angles in parentheses). Based on these initial conditions, the lunar orbiter has emerged from behind the far side of the moon and is in the middle of a near-side pass. In the numerical integration of the "truth" model, partial derivatives were not calculated. Auxiliary software programs then used the numerical integration output files for the three cases as well as the covariance files for the two estimated fit models to perform the error analysis.

Table 7.3-1: Low Inclination, Low Altitude Evaluation Orbit  
Satellite Initial Conditions

$a_0$	1838 km ( $1.22862712 \times 10^{-5}$ AU)
$e_0$	0.01
$i_0$	15° (30.7285027175189°)
$\Omega_0$	210° (26.9029402084826°)
$\omega_0$	180° (222.6750569007985°)
$M_0$	315°

### **7.3.1 State Uncertainty Prediction**

The state uncertainty prediction based on PEP's gravity harmonic coefficient covariance matrix ( $A^{-1}$ ) derived from the assumed measurement errors was overly optimistic for both cases since the fit residuals for the two estimated runs were so high (365.954 and 361.099 rms). This method predicted root sum squared (rss) state uncertainties less than 500 meters in position and one half of a meter per second in velocity over the orbit for the single orbiter estimated fit case. For the dual orbiter estimated fit model this method predicted rss uncertainties of less than 250 meters in position and one quarter of a meter per second in velocity over the same orbit. These predictions are extremely optimistic, especially when compared to the orbital errors presented in Section 7.3.2.

The prediction based on the estimated fit's covariance matrix  $\Sigma$  from Equation (5.2-2) provided a more realistic assessment of the state uncertainties. This method predicted rss state uncertainties as high as 4 kilometers in position and 4 meters per second in velocity for the single orbiter estimated fit case. These predicted state uncertainties, transformed to the local vertical, local horizontal coordinates, are plotted over time for this lunar orbit in Figure 7.3.1-1. For the dual body estimated fit model, this analysis predicted rss uncertainties of approximately 750 meters in position and 0.6 meters per second in velocity. These local vertical, local horizontal predicted state uncertainties are plotted over time in Figure 7.3.1-2. These state uncertainty plots show that the largest position uncertainties are in the range direction and the largest velocity uncertainties are in the vertical direction as might be expected for the radial acceleration perturbations caused by the mascons.

This state uncertainty prediction analysis demonstrates the importance of including lunar far-side observations in the estimation process. The uncertainties predicted for the gravity model estimated from the dual orbiter sensing scheme were approximately one fourth of those estimated from the single orbiter sensing scheme. The dual orbiter cases' uncertainties were also very low while the lunar satellite passed across the lunar near side (first forty minutes of numerical integration). For both cases, the uncertainties grow as the orbiter passes behind the far side of the moon, reaching local maximums



for velocity in the vertical direction and position in the down range direction in the middle of the far-side pass. These uncertainties subside when the spacecraft reemerges from the far side of the moon eighty-eight minutes into the orbit. From this point the uncertainties increase during the final lunar near-side pass.

### **7.3.2 State Errors Between "True" and Estimated Gravity Models**

The errors between the "true" and estimated fit lunar gravity models were determined from a direct comparison of the two numerical integration files. These state errors were then transformed to local vertical, local horizontal coordinates. The local vertical, local horizontal state errors between the orbits generated for the single orbiter estimated lunar gravity field and the "true" gravity field are plotted in Figure 7.3.2-1. The same errors resulting from the difference between the dual orbiter estimated gravity field and the "true" gravity field are plotted versus time in Figure 7.3.2-2.

The errors for the single orbiter estimated gravity field stay relatively flat as the orbiter crosses the near side of the moon. Forty minutes into the numerical integration the orbiter passes behind the moon. Midway through the far-side pass there is a rapid growth of velocity errors. Shortly thereafter these velocity errors manifest themselves as position errors as large as 15 kilometers in the range and 10 kilometers in the cross track directions. These errors demonstrate this estimated fit model's inability to estimate the far-side gravity field.

The errors for the dual orbiter estimated gravity field are much lower than in the previous case. When plotted on the same scales as the errors in the first case, the dual orbiter case's velocity errors stay in a narrow band around zero meters per second. The dual orbiter position errors are also much more reasonable for the cross track and vertical directions. The dual orbiter estimated gravity model still results in large range errors over the single lunar orbit. Since the dual orbiter estimated lunar gravity model is based on observations over the entire lunar surface, the position and velocity errors do not manifest themselves at a specific point in the lunar orbit as was the previous case. In this case the cross track and vertical position errors and

## Single Orbit Spacecraft State Uncertainty

Predicted State Uncertainty for Single Orbiter Sensing Fit

Inclination = 15 deg, Eccentricity = 0.01, Altitude = 100km

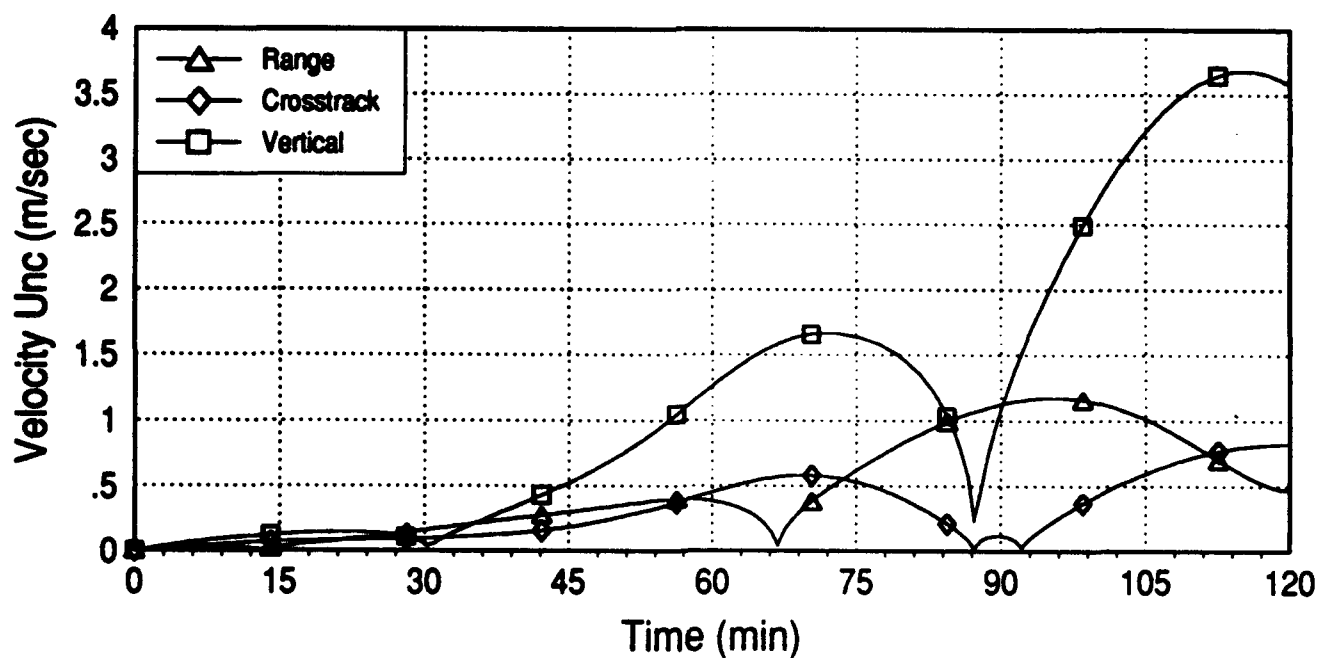
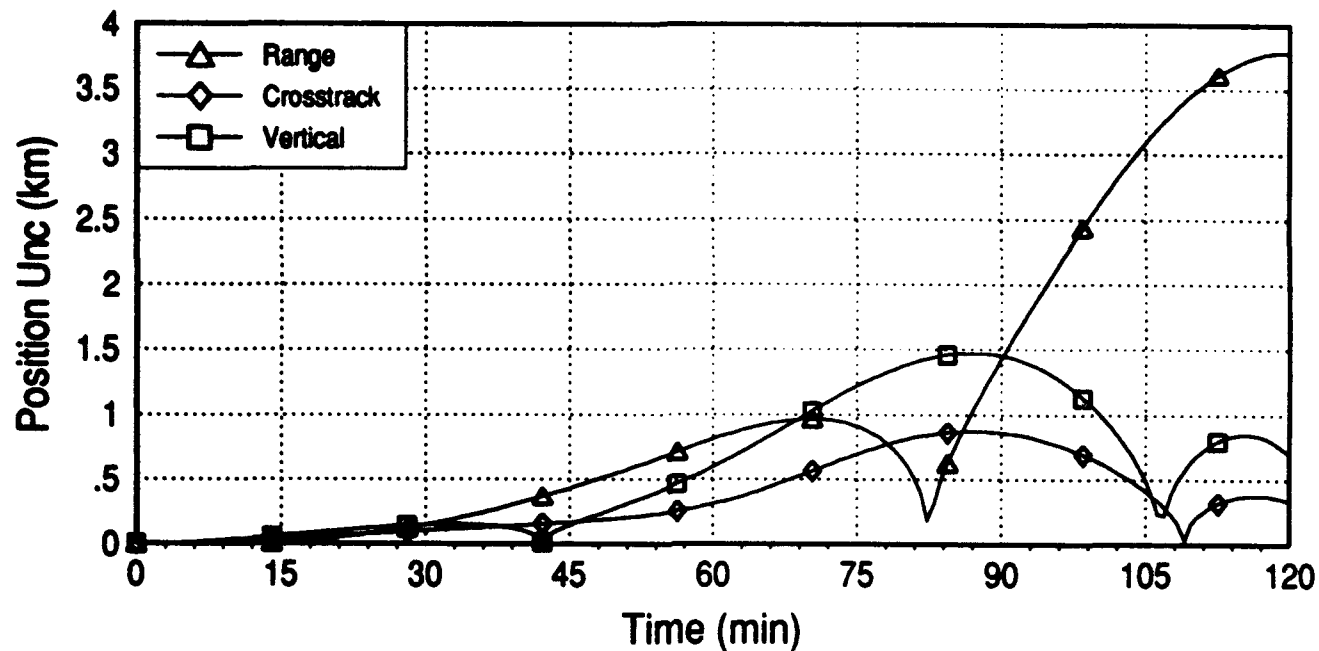


Figure 7.3.1-1: Single Orbiter Estimated Gravity Field State Uncertainties

## Single Orbit Spacecraft State Uncertainty

Predicted State Uncertainty for Dual Orbiter Sensing Fit  
Inclination = 15 deg, Eccentricity = 0.01, Altitude = 100km

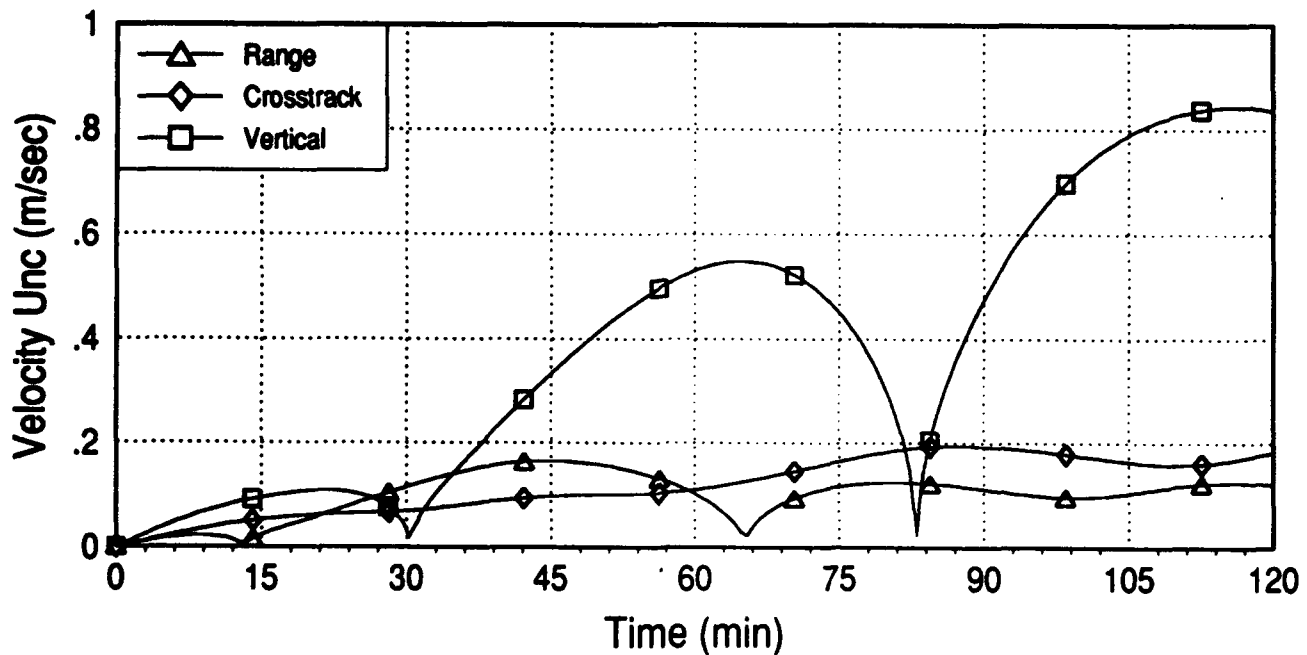
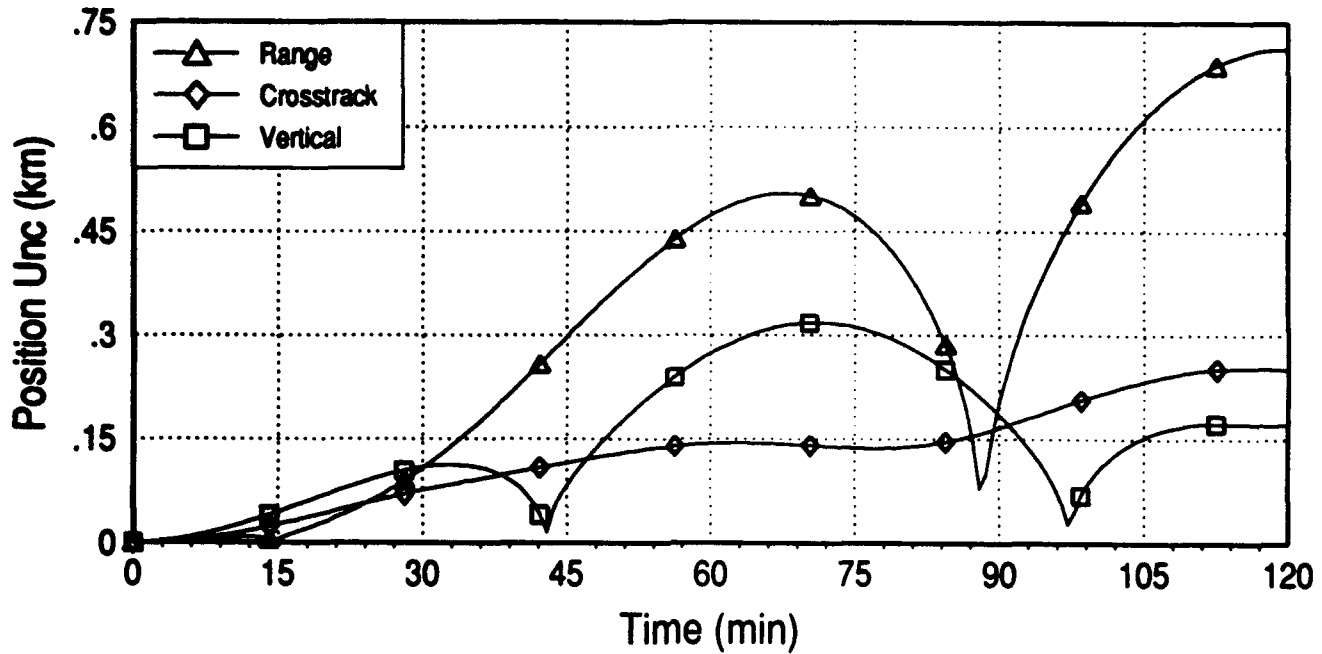


Figure 7.3.1-2: Dual Orbiter Estimated Gravity Field State Uncertainties

## Single Orbit Spacecraft State Errors

Errors Between Single Orbiter Sensing Scheme Fit and Truth Model

Inclination = 15 deg, Eccentricity = 0.01, Altitude = 100km

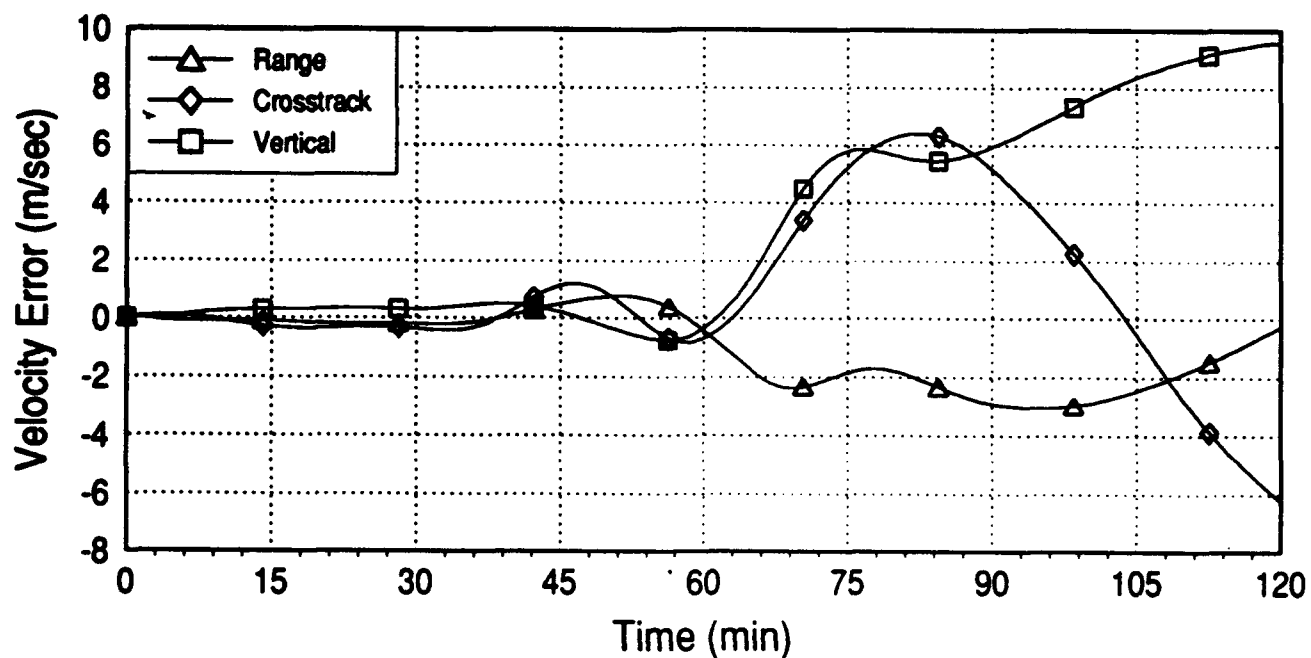
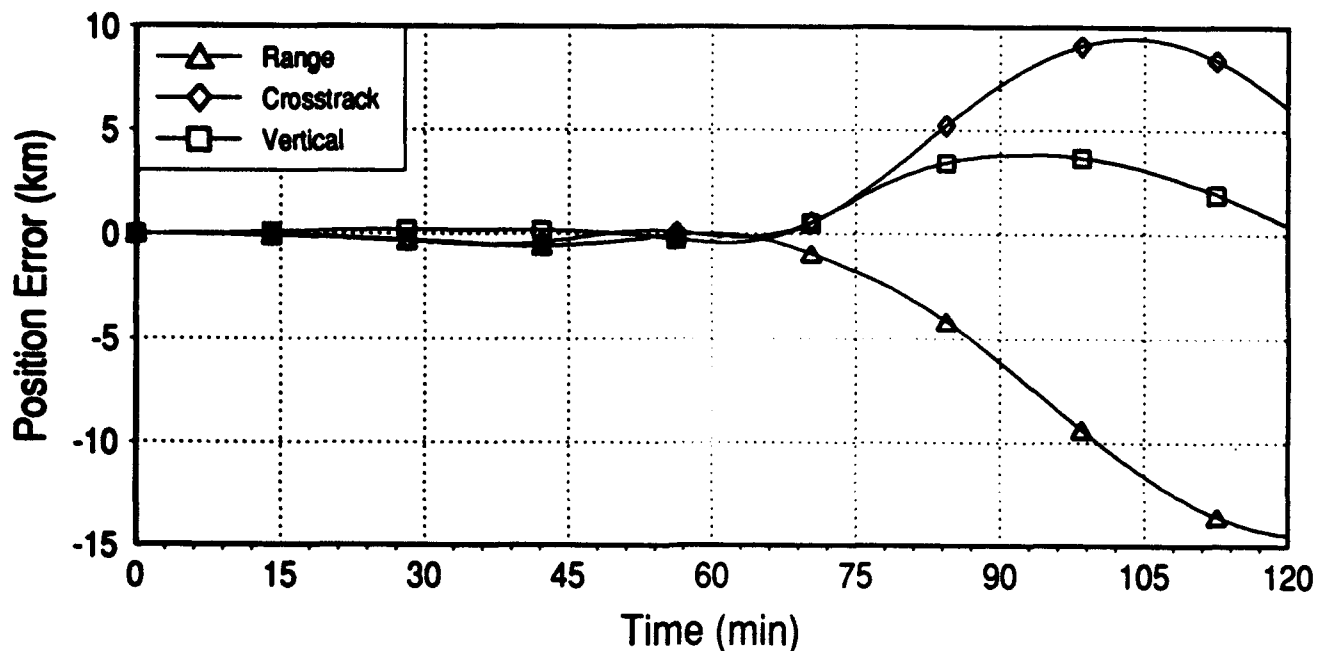


Figure 7.3.2-1: Single Orbiter Estimated Gravity Field State Errors

## Single Orbit Spacecraft State Errors

Errors Between Dual Orbiter Sensing Scheme Fit and Truth Model

Inclination = 15 deg, Eccentricity = 0.01, Altitude = 100km

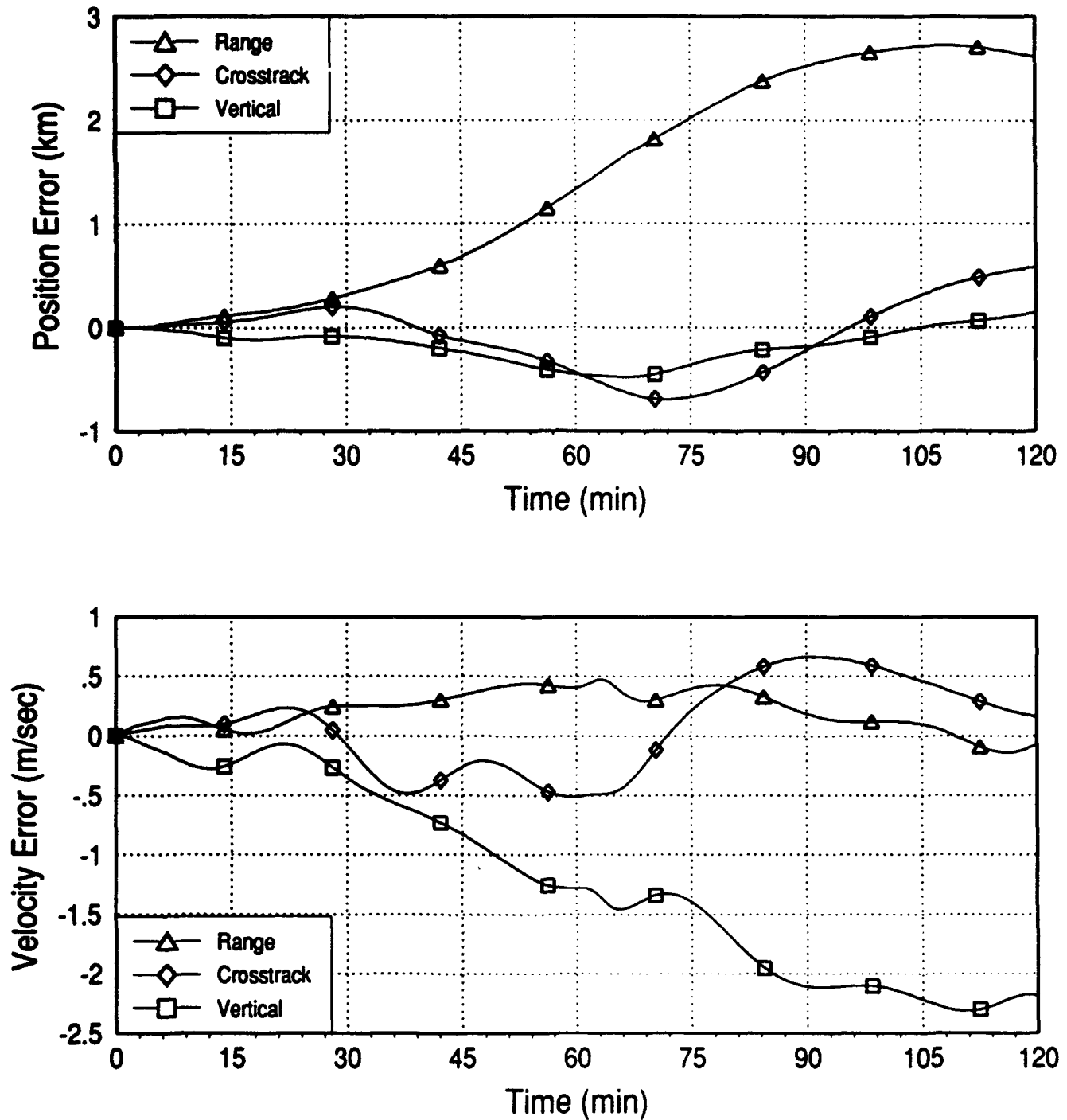


Figure 7.3.2-2: Dual Orbiter Estimated Gravity Field State Errors

the range and cross track velocity errors oscillate about zero for the single lunar orbit. The vertical velocity errors and resulting down range position errors, however, grow without oscillating about zero for the single orbit propagation.

For both cases the state uncertainty prediction was very optimistic, even after including the rms of the fit residuals. This discrepancy results from the difference between the structure of the two lunar gravity models ("truth" and fit). The rss of the predicted position uncertainty was an order of magnitude less than the "true" position errors. The predicted uncertainty in velocity was only slightly better. Additionally, the covariance analysis does not successfully predict cross track position uncertainties. This is especially apparent for the single orbiter estimated gravity field case. Figure 7.3.2-1 shows significant cross track state errors and no notable cross track uncertainties are predicted in Figure 7.3.1-1.

When analyzing the proposed Lunar Observer mission with different truth and fit models, Alex Konopliv also noted that a covariance uncertainty analysis was unbelievable because it was "overly optimistic for all cases" [25]. This deficiency in the covariance analysis is an indication that the system dynamic model needs to include some process noise to account for the gravity field mismodeling. A Kalman filtering or maximum likelihood system identification technique could include this process noise as it propagated the satellite equations of motion.

### **7.4 Lunar Deorbit Maneuver Error Analysis**

Finally, a satellite lunar landing from a low inclination circular orbit was simulated for both estimated gravity fields. The deorbit burn for this lunar maneuver was determined based on numerical orbit integrations using the estimated lunar gravity fields. This maneuver was then executed in the "true" lunar gravity field, and the position errors at PDI were used to evaluate the two estimated gravity field models' ability to plan future lunar missions.

This analysis assumed that the spacecraft was resupplying a lunar base on the near side of the moon and had been inserted into a circular, low inclination orbit. The transfer from this orbit to the lunar surface was planned using a Hohmann transfer. The circular parking orbit was numerically integrated from the near side of the moon to the middle of the far side of the moon. At this point, a deorbit burn placed the spacecraft in an elliptical transfer orbit. The spacecraft's pre-planned Powered Descent Initiation (PDI) location coincided with the elliptical transfer orbits' perilune. From this point, the spacecraft would begin its powered descent to the lunar surface and rendezvous with the lunar base. The powered descent portion of the landing mission was not simulated in this analysis.

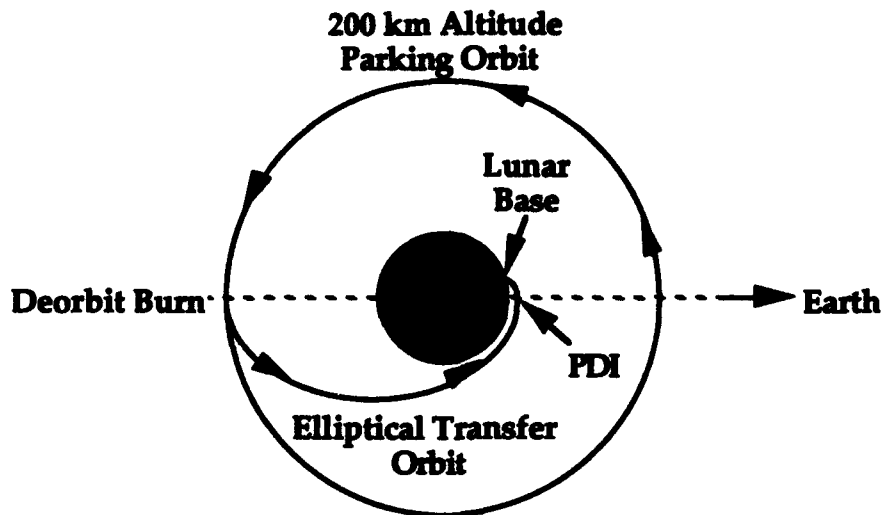


**Figure 7.4-1: Lunar Deorbit Mission**

The mission simulation began by integrating the spacecraft's circular orbit starting on 16 May 1968 (JD 2,440,001.5 0<sup>h</sup>) with the satellite selenographic initial conditions listed in Table 7.4-1 (1950.0 angles in parentheses). Based on the satellite's state at  $M=180^\circ$  in the parking orbit, an initial guess for the  $\Delta v$  was calculated for a Keplerian transfer orbit with the PDI perilune altitude, the lunar surface for this analysis. The elliptical transfer orbit was then numerically integrated and the guessed  $\Delta v$  updated based upon the PDI position error at perilune. These iterations were continued until acceptable target PDI positions were obtained. Since this maneuver was planned for the two different estimated lunar gravity fields, two different  $\Delta v$ 's were calculated and subsequently executed.

## LUNAR GRAVITATIONAL FIELD ESTIMATION AND SATELLITE ORBIT PREDICTION

For the single body estimated gravity field case, the calculated deorbit burn occurred over  $0.0611^\circ$  south latitude and  $179.9215^\circ$  west longitude approximately 63.985 minutes into the numerical integration. The transfer  $\Delta v$  had a magnitude of  $2.535 \times 10^{-5}$  AU/day (PEP's units) with a projected PDI at  $0.040^\circ$  south latitude and  $1.951^\circ$  west longitude. This burn was then executed by the spacecraft in the "true" lunar gravity field. At 63.985 minutes into the numerical orbit integration the previously calculated  $\Delta v$  was subtracted from the satellite's inertial velocity to simulate the deorbit burn. The numerical integration then proceeded from this new state. This maneuver resulted in a PDI at  $0.766^\circ$  south latitude and  $9.903^\circ$  west longitude, a  $7.952^\circ$  error in longitude and  $0.725^\circ$  error in latitude!

Table 7.4-1: Low Inclination, Lunar Landing Parking Orbit  
Satellite Initial Conditions

$a_0$	1938 km ( $1.295472995 \times 10^{-5}$ AU)
$e_0$	0.0005
$i_0$	$5^\circ$ ( $18.2129222440553^\circ$ )
$\Omega_0$	$0^\circ$ ( $349.1664497093493^\circ$ )
$\omega_0$	$0^\circ$ ( $226.5049507382479^\circ$ )
$M_0$	$0^\circ$

The deorbit was then planned with the dual orbiter estimated lunar gravity field. The deorbit burn was again scheduled for 63.985 minutes into the orbit (from the satellite initial conditions in Table 7.4-1) at a selenographic latitude of  $-0.0358^\circ$  and longitude of  $-179.9851^\circ$ . The planned magnitude of the  $\Delta v$  was  $2.5225 \times 10^{-5}$  AU/day with a projected PDI of  $0.4339^\circ$  south latitude and  $5.8691^\circ$  west longitude. This maneuver was then executed with the "true" lunar gravity field. This simulation resulted in a PDI at  $0.2503^\circ$  south latitude and  $4.008^\circ$  west longitude. The PDI errors in this case were now  $1.8613^\circ$  in longitude and  $0.1835^\circ$  in latitude, a significant reduction in the PDI position errors and further evidence of the importance of including lunar far-side observations in lunar gravity field estimations.

On the lunar surface these errors in latitude and longitude would result in a position error of 242 kilometers in the single orbiter estimated  $8 \times 8$  field case and 56 kilometers for the dual orbiter estimated  $8 \times 8$  field. If the landing spacecraft began powered descent this far off target it should still be



able to land close to the lunar base, as long as it is close enough to receive a radio beacon signal. The suboptimal descent trajectory required to compensate for these errors, especially in the first case, would seriously cut into any propellant margins, perhaps jeopardizing future mission plans.

The magnitude of the navigation errors might be reduced if higher than  $8 \times 8$  spherical harmonic or other gravity model fits were estimated. For higher degree and order fits, it would be interesting to note whether the above factor of 4.3 improvement in navigation accuracy still held when far-side satellite-to-satellite measurements were added to near-side earth-based measurements.

## **7.5 Gravity Coefficient Parameter Correlation Analysis**

Each of the estimation runs in Chapter Six produced extremely high correlations for some of the gravitational coefficients. These high correlations inhibited the estimation routine's ability to converge quickly and provide an accurate estimate of the gravitational parameters. Different measurement types and orbital orientations were analyzed to see if any of these parameter correlations could be broken. For this analysis, "truth" model observations were generated for the new observation methods. Based on each new set of observations, the lunar gravity field was estimated for a single iteration of the process outlined in Figure 6.1-1. The gravitational parameter correlations were then obtained from the single iteration's covariance matrix.

For the first correlation analysis, the elliptical "viewing" orbit in the dual orbiter, bent pipe observation scheme was placed in an orthogonal, rather than coplanar, orbit plane. The "sensing" orbit was left in its polar orbit to provide full lunar surface coverage over the fourteen day observation period, so the elliptical satellite was placed in an equatorial orbit. From this orbital geometry, bent pipe observations identical to the coplanar case were simulated for the estimation process. From this iteration, sixteen of the 3,926 correlations were greater in magnitude than 0.90. Fourteen of these were greater than 0.95. The  $\bar{C}_{55}\bar{C}_{75}$ ,  $\bar{S}_{55}\bar{S}_{75}$  pairs had the highest correlation of

## LUNAR GRAVITATIONAL FIELD ESTIMATION AND SATELLITE ORBIT PREDICTION

-0.999. The  $\bar{C}_{54}\bar{C}_{74}$ ,  $\bar{S}_{54}\bar{S}_{74}$  correlation pairs were the second highest at -0.996. The  $\bar{C}_{66}\bar{C}_{86}$  and  $\bar{S}_{66}\bar{S}_{86}$  pairs also had correlations greater than -0.993

The second method investigated an interferometric observation method to determine its impact on the high gravitational parameter correlations. For this scenario, NASA DSN stations made milli-arc second long baseline interferometer measurements of the near-circular 200 km altitude lunar orbiter in addition to the 3 meter range and 1 mm/sec Doppler observations. Because of difficulties encountered simulating PEP's internal interferometry observations, these interferometer measurements were simulated by azimuth and elevation angle observations for a single DSN site (Goldstone) with the interferometric accuracy. Since the interferometer observations only provide a planar angular measurement, the fitting process was executed ignoring the elevation angle observations. The fitting process was then repeated using both of the angle measurements to see what impact precise earth-based three-dimensional angular observations combined with range and Doppler observations would have on the gravitational parameter coefficients.

For both of these fit cases (azimuth only/azimuth and elevation), twenty two of the 3,403 correlations were greater in magnitude than 0.90 and fifteen of these were greater than 0.95. The parameter correlations were almost identical for the two cases, with the highest parameter correlations differing only in the fourth or fifth decimal place. The  $\bar{S}_{55}\bar{S}_{75}$  and  $\bar{C}_{55}\bar{C}_{75}$  pairs were the most highly correlated (-0.999). The  $\bar{C}_{65}\bar{C}_{85}$ ,  $\bar{S}_{65}\bar{S}_{85}$ ,  $\bar{C}_{54}\bar{C}_{74}$ ,  $\bar{S}_{54}\bar{S}_{74}$  parameter correlations were the second highest group. For the interferometric case the 66, 86 correlations are still very high (> -0.990).

For the final case, the Goddard Space Flight Center's (GSFC) proposed co-orbital laser ranging and Doppler lunar gravity field sensing scheme was simulated (Figure 1.4-2). The main satellite was placed in the polar near-circular 200 km altitude orbit which has proven so useful throughout this thesis. The co-orbiting subsatellite was placed in the identical orbit but with an initial mean anomaly nine degrees ahead of the main satellite. Laser ranging and sixty second Doppler observations were processed for the entire fourteen day orbit with 1 mm laser ranging and 1 mm/sec Doppler accuracies. These accuracies were based on GSFC briefed capabilities [2]. Additionally this

method used two-way coherent Doppler observations between the DSN Goldstone site and the main satellite using the S-Band (2.115 GHz) frequency with 1 mm/sec accuracy for sixty second count intervals.

For this case, the parameter correlations were different from all of the previous iterations. The highest gravity coefficient correlations were now the  $\bar{S}_{54}\bar{S}_{74}$  and  $\bar{C}_{54}\bar{C}_{74}$  pairs (-0.998 and -0.996 respectively) with the two initial osculating orbital eccentricities also highly correlated (-0.997). The 66, 86 and 55, 75 correlations in this case were smaller in magnitude than 0.850 except for the  $\bar{S}_{55}\bar{S}_{75}$  correlation which was -0.926.

Each parameter estimation run also determined the spread of the parameter correlations. For each different measurement type and orbital geometry investigated, this distribution was divided by the total number of correlations. Figure 7.5-1 plots this normalized distribution for the parameter correlations greater than 0.50. This graph shows how the single orbiter, earth-based sensing scheme is characterized by very high parameter correlations. If a subsatellite and laser ranging and Doppler instrumentation are added to this scheme, the correlations are driven down significantly and lunar far-side motion is observed. If these mission modifications are not feasible, then augmenting the single orbiter earth-based sensing scheme with long baseline interferometer measurements will also reduce the parameter correlations, although several of the highest correlations still remain in both cases.

According to the graph, a better mission modification would be to include an elliptical "viewing" satellite to observe the near-circular low altitude polar "sensing" satellite. The chart suggests that if the "viewing" satellite is placed in an orbital plane orthogonal to the "sensing" satellite's orbital plane, the lowest parameter correlations are achieved. If both spacecraft, however, are launched together and then separated after Lunar Orbit Insertion (LOI), as was planned for the Lunar Observer mission [39], then coplanar "viewing" and "sensing" satellites will still provide one of the lowest sets of parameter correlations.

These attempts to break the parameter correlations demonstrate that although some of the parameter correlations can be reduced, using a near-circular polar 200 km altitude satellite as the "sensing" vehicle to estimate an  $8 \times 8$  spherical harmonic expansion to model the lunar gravity field

## LUNAR GRAVITATIONAL FIELD ESTIMATION AND SATELLITE ORBIT PREDICTION

consistently results in extremely high gravitational parameter correlations between the  $\bar{C}_{55}\bar{C}_{75}$ ,  $\bar{S}_{55}\bar{S}_{75}$ ,  $\bar{S}_{66}\bar{S}_{86}$ , and  $\bar{C}_{66}\bar{C}_{86}$  gravitational parameters.

**Parameter Correlation Distribution**

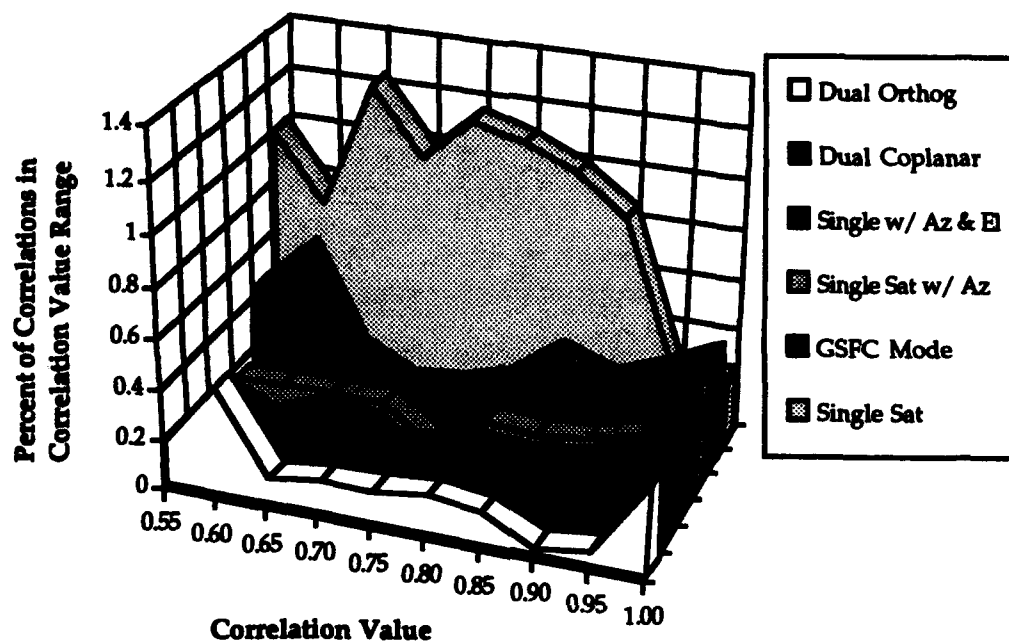


**Figure 7.5-1: Parameter Correlation Distributions for Several Observation Methods**

Because the highest parameter correlations are always for the  $n-2$ ,  $n-2$  and  $n$ ,  $n-2$  parameters and the  $n-3$ ,  $n-3$  and  $n-1$ ,  $n-3$  parameters, the spherical harmonic expansion geometry should be investigated. Both sets of correlations involve sectorial terms and a tesseral counterpart with the same number of longitudinal slices. The  $n=m=6$  sectorial and  $n=8$ ,  $m=6$  tesseral terms zero lines are illustrated by the globes in Figure 7.5-2. The geometrical relationship of these highly correlated gravitational parameters suggests that they may result from estimating the lunar gravity field solely from observations of a polar lunar satellite, since the satellite's ground track repeatedly traverses the sectorial slices of the moon.

This analysis suggests that the best way to break the high gravity coefficient correlations would be to use multiple inclination "sensing" satellites. In his lunar harmonic gravity analysis, Alfred Ferrari noted that

"...[W]ell conditioned estimates of the gravity harmonics are only achieved when data from many different inclinations are used, ..." [19]. Multiple inclination observations could be achieved by using new polar satellite data along with existing Apollo-era near equatorial satellite data. A better scheme is to place near-circular, low altitude "sensing" satellites in  $90^\circ$  and  $45^\circ$  inclination orbits and observe their lunar far-side motion with a single elliptical "viewing" satellite. This data could also be combined with existing Apollo-era Doppler tracking data when estimating the lunar gravity field.

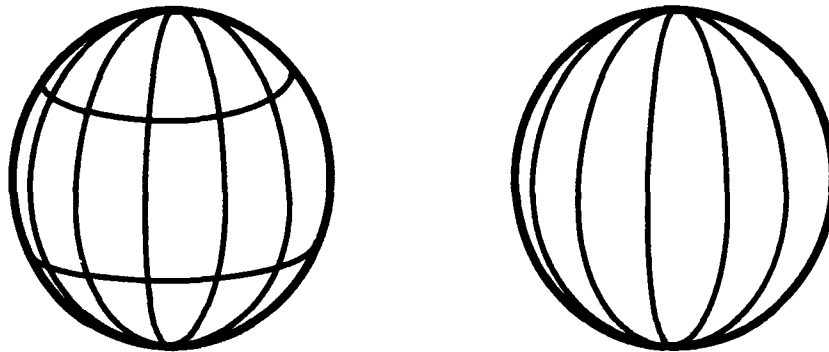


Figure 7.5-2: Tesseral 8,6 and Sectorial 6,6 Zero Line Patterns



## Chapter Eight

# Conclusions

### 8.1 Summary of Results

This thesis investigated the ability of spherical harmonic expansion estimates of the lunar gravity field to predict low altitude lunar orbits globally. These lunar spherical harmonic expansions were estimated from simulated observations of a near-circular polar lunar satellite. Several different observation geometries and measurement methods were investigated; two were used to estimate the lunar gravity field.

Since most of the methods used to derive the lunar gravity field employ Doppler observations, a test was performed to determine the impact sensing geometry had on gravity field estimation. Since the Doppler observations measure velocity along the line-of-sight, the geometrical orientation between the Doppler line-of-sight and the vector between the mascon and orbiting body will affect the observation's ability to detect the mascon's presence. For the first scenario in this test, a pair of mascons were placed on the lunar limbs and an eighth degree and order spherical harmonic expansion was estimated. For the second scenario, two mascons were placed on the lunar near- and far-side faces and the process was repeated. Unfortunately, the test case was unable to conclusively establish the impact of viewing geometry upon the ability to detect and model local mascon disturbances.

A lunar gravity "truth" model was developed for this thesis which combined a fifth degree and order spherical harmonic expansion and nine major mass anomalies or mascons. The seven most significant lunar maria mass anomalies, as identified by Wong et. al. [47], served as the lunar near-

## LUNAR GRAVITATIONAL FIELD ESTIMATION AND SATELLITE ORBIT PREDICTION

side mascons. The two significant far-side mascons were positioned to be difficult to sense from earth-based observations and to balance the lunar center of mass. This truth model, since it contained mascon disturbances, was intended to be a difficult gravity field to model with a pure spherical harmonic expansion.

Using the lunar gravitational "truth" model, the near-circular polar lunar satellite gravity field "sensing" orbit was numerically integrated for fourteen days, half of a lunar period, to provide complete lunar surface coverage as the moon rotated under the orbital plane. Since this satellite does not actually measure the lunar gravity field, different techniques were used to observe this satellite's motion and estimate the gravity field. Estimates of the coefficients in spherical harmonic expansions sought to match the observations of the "sensing" satellite's motion. Based on the observation residuals between the initial parameter guesses' theoretical observations and the "truth" model observations, the initial conditions and harmonic coefficients were adjusted and the process was iterated until the best fit to the observations was obtained. Although different degree and order spherical harmonic expansion fits were attempted, the iterative process failed to converge for those above eighth degree and order, probably because of the difference between the "truth" (spherical harmonics plus mascons) and fit (spherical harmonic expansion only) models.

Estimated lunar gravity fields were obtained for two different sensing schemes. The first scheme recreated the gravitational sensing method used during the Apollo era with mostly near-equatorial satellites. Earth-based Doppler observations of the near-circular polar lunar satellite were used to estimate the lunar gravity field. The second sensing scheme employed a second lunar satellite in an elliptical orbit, viewing the first satellite's motion. Earth- and satellite-based Doppler observables simulated the coherent bent pipe link between an earth tracking station, the elliptical "viewing" satellite, and the circular "sensing" satellite proposed for the Lunar Observer mission [16, 39, 40].

For the cases in which the estimation process converged upon a fit to the observations, the fit model was analyzed to determine how well it



modeled the "true" lunar gravity field. The model's fit to the observations as well as its ability to model global radial accelerations were investigated.

The observation techniques which employed Doppler observations of the lunar far-side motion provided a much better fit to the "true" gravity field. Both estimation techniques employed an eighth degree and order spherical harmonic expansion. In neither case, however, did the eighth degree and order spherical harmonic expansion closely model the "true" lunar gravity field.

Parameter covariance information determined in the estimation fitting process was used to predict satellite state uncertainties ahead one lunar orbit. A low altitude, low lunar inclination orbit was selected for this analysis. Significantly lower state covariances were predicted for the estimated lunar gravity field based on the dual orbiter sensing scheme. Observations of the lunar polar satellite during far-side passes significantly reduced the predicted uncertainties for the estimated fit model. In the best case, the eighth order spherical harmonic expansion predicted uncertainties of close to three quarters of a kilometer in position and one meter per second in velocity for the orbit, hardly acceptable for future lunar missions.

Using the lunar gravity "truth" model, the satellite's "true" position and velocity were numerically integrated ahead one orbit. The true spacecraft state was then compared to the predicted state to reveal the state errors. These errors were then compared to the covariance uncertainties. Once again, the estimated fit model which included lunar far-side observations did a significantly better job of predicting the correct satellite state, although it still provided errors as large as 2.8 kilometers in position and 2.3 meters per second in velocity. In neither case did the spherical harmonic expansion fit model's covariance uncertainties come close to predicting the correct state errors, further evidence of the eighth degree and order expansion's inability to successfully predict lunar orbits for future lunar missions.

The estimated fit models were then used to plan a lunar landing deorbit maneuver. Starting on the near side of the moon in a circular low lunar inclination parking orbit, the satellite's orbit was numerically integrated to the far side of the moon where a deorbit maneuver placed it in an elliptical transfer orbit. When the spacecraft reached a specified lunar altitude, as

## LUNAR GRAVITATIONAL FIELD ESTIMATION AND SATELLITE ORBIT PREDICTION

detected by an on-board radar altimeter, it began its powered descent to the lunar surface. After planning the deorbit maneuver to reach a specific location for powered descent initiation (PDI), the deorbit maneuver was executed in the "true" lunar gravity field.

The lunar deorbit maneuver planned with the single orbiter earth-based Doppler sensing scheme estimated gravity field reached PDI altitude eight degrees in selenographic longitude and three quarters of a degree in latitude away from its target position, a surface error of over two hundred and forty kilometers. The lunar deorbit maneuver planned for the dual orbiter gravity field was only one and three quarters of a degree of longitude and one fifth of a degree of latitude off target when it reached PDI altitude. This scenario's lunar surface error was fifty-six kilometers, an error much easier to recover from during powered descent. Both cases, however, indicate that further navigation aides will be required during lunar operations, such as radio beacons at a lunar base or a global lunar navigation system.

Extremely high parameter correlations were encountered when estimating the gravity coefficients. Three different measurement schemes were investigated to see if they could reduce these parameter correlations. In the first case, the elliptical "viewing" satellite was placed in an orbital plane orthogonal to the circular "sensing" satellite's orbital plane. In the second case, earth-based interferometer measurements were added to the single orbiter, earth-based Doppler sensing scheme. Both east-west and north-south look angles were simulated in this search for a way to break the high parameter correlations. The third case simulated the Goddard Space Flight Center's proposed co-orbital laser ranging and Doppler sensing scheme [2].

The first method was able to reduce some of the high parameter correlations from the dual orbiter co-planar sensing scheme, but several of the highest parameter correlations remained. The second case significantly reduced the high parameter correlations from the single satellite earth-based Doppler-only sensing scheme, although once again the same highest parameter correlations still remained. The third case produced some different high parameter correlations. This method reduced the parameter correlations significantly from the single orbiter, earth-based Doppler sensing scheme. Although this case would reduce the parameter correlations from

the single orbiter case, it does not reduce the correlations as much as the dual orbiter coplanar and orthogonal cases.

Since none of these new observation techniques eliminated the highest parameter correlations, the spherical harmonic expansion geometry was investigated to determine why the same parameters were so highly correlated. It seems that the extremely high correlations result from using a single polar "sensing" orbit for all of the gravity field estimates. Polar ground tracks made it difficult to separate the effects of some of the sectorial and related tesseral terms. "Sensing" orbits at different orbital inclinations should break the extremely high parameter correlations and aid the lunar gravity field estimation process.

## **8.2 Recommendations for Future Research**

The research for this thesis revealed several topics for further investigation. First, a more efficient gravity field model based on a surface layer representation should be investigated. A surface layer representation would require roughly one third of the parameters than a spherical harmonic expansion to model the lunar gravity field's high frequency behavior. The surface layer representation should be able to constrain the total lunar mass and lunar center of mass. Estimated fits with this gravity field model, if it is programmed into the Planetary Ephemeris Program, can be compared to those obtained with a spherical harmonic expansion gravity field model.

Additionally, this thesis only compared the estimated fit models for two observation techniques. Because of its observability into the lunar far-side motion, the dual orbiter scheme naturally provided a better fit to the lunar gravity "truth" model. Estimated fit models should be developed for the three different observation methods investigated to break the high parameter correlations. Different Doppler observation methods, besides the bent pipe method, can be investigated, including the satellite bounce and satellite beacon methods proposed by JPL [40]. Straightforward software changes in PEP should allow simulation of these observables, and further modifications would allow the incorporation of lunar navigation aids (either

## LUNAR GRAVITATIONAL FIELD ESTIMATION AND SATELLITE ORBIT PREDICTION

lunar surface sites or navigation satellites). Additionally, two "sensing" satellites in different inclinations should be studied to verify their ability to break the high parameter correlations. Higher degree and order simulated fits should also be attempted to determine the navigation improvements that can be achieved with higher resolution spherical harmonic expansions.

For further studies, a less stringent lunar gravity "truth" model should be used. The difficult to observe mascon on the lunar far side was too large, in both surface area and total strength. The lunar center of mass should still be constrained, but the far-side mascons should be roughly the same size and strength as their near-side counterparts.

If lunar rotation moment of inertia partial derivatives in the Planetary Ephemeris Program are changed to equivalent second harmonic partial derivatives, PEP can include lunar laser corner reflector observations simultaneously with satellite observations in the estimation of the lunar gravity field. The lunar laser observations would provide very accurate determinations of the lower degree harmonics (second and even third and fourth degree [13]), while the lunar satellite observations would aid the estimation of higher degree harmonics.

Finally, the most appropriate method to estimate the lunar gravity field with real observations is to use maximum likelihood system identification. This method runs a Kalman filter on the satellite motion with noise in the dynamics due to unmodeled forces, and applies a maximum likelihood estimator to gravity, initial condition, and other parameters [31 Chapter 10].

## Appendix A

# Evaluation of Legendre Polynomials and Normalized Legendre Functions

### A.1 Legendre Polynomials

The Legendre polynomials and their first and second derivatives are required for the numerical integration of the equations for satellite motion and for the partial derivatives of satellite motion. The Legendre polynomials are used to determine the zonal harmonic gravity effects and are also used in the recursive formulas for the Legendre functions. Unnormalized zonal harmonic gravity coefficients are input to PEP since its algorithms use the unnormalized form of the Legendre polynomials. These algorithms were left unchanged, because the normalization factor in the equation

$$\bar{P}_n(z) = \sqrt{2n+1} P_n(z) \quad (\text{A.1-1})$$

does not grow too rapidly with zonal harmonic degree  $n$ , and the normal equation's automatic scaling feature works around any numerical problems (Section 5.1.6). A switch to normalized zonal harmonic coefficients  $\bar{C}_{n0}$  from  $J_n$  would also involve a sign change in several PEP subroutines.

The recursive evaluation of  $P_n(z)$ ,  $P'_n(z)$ ,  $P''_n(z)$  in subroutine LEGNDR (and the new subroutine LEGNDS) uses the relations [1, 8]

$$nP_n(z) = (2n-1)zP_{n-1}(z) - (n-1)P_{n-2}(z) \quad (\text{A.1-2})$$

$$P'_n(z) = P'_{n-2}(z) + (2n-1)P_{n-1}(z) \quad (\text{A.1-3})$$

$$P''_n(z) = P''_{n-2}(z) + (2n-1)P'_{n-1}(z) \quad (\text{A.1-4})$$

with the starting values

$$P_0(z) = 1, P_1(z) = z, P_2(z) = \frac{1}{2}(3z^2 - 1), P_3(z) = \frac{1}{2}(5z^3 - 3z) \quad (\text{A.1-5})$$

$$P'_0(z) = 0, P'_1(z) = 1, P'_2(z) = 3z, P'_3(z) = \frac{1}{2}(15z^2 - 3) \quad (\text{A.1-6})$$

$$P''_0(z) = 0, P''_1(z) = 0, P''_2(z) = 3, P''_3(z) = 15z \quad (\text{A.1-7})$$

The evaluation of the above functions starts with  $n = 2$ , since the spherical harmonic expansions in PEP start at the second degree (assuming the center of mass of the central body coincides with the origin of coordinates).

## **A.2 Normalized Legendre Functions**

The Legendre functions and their first and second derivatives are required for the numerical integration of the equations for satellite motion and for the partial derivatives of satellite motion. Legendre functions are used to determine the tesseral harmonic gravity effects. The original version of PEP converted normalized tesseral harmonic gravity coefficients ( $\bar{C}_{nm}$ ,  $\bar{S}_{nm}$ ) from the input stream into unnormalized coefficients ( $C_{nm}$ ,  $S_{nm}$ ) since its internal algorithms computed the unnormalized versions of the Legendre functions. The option was added to PEP (incorporated into the SAO version) to use normalized Legendre functions in the numerical integration process. This option was desirable since the normalization factors vary widely for high degrees  $n$ , especially as  $m$  approaches  $n$  in the equation

$$\bar{P}_{nm}(z) = \sqrt{\frac{2(2n+1)(n-m)!}{(n+m)!}} P_{nm}(z), \quad m = 1, \dots, n \quad (\text{A.2-1})$$

Define the precalculated coefficients for  $m = 1, \dots, n$  and  $n \geq 1$

$$a_{nm} = \sqrt{\frac{(2n+1)(n-m)}{(2n-1)(n+m)}} \quad (\text{A.2-2})$$

# Appendix A: Legendre Polynomials And Functions

$$b_{nm} = \sqrt{\frac{(2n)(2n+1)}{(n+1)}}, \quad m=1 \quad (\text{A.2-3})$$

$$b_{nm} = \sqrt{\frac{(2n+1)(n+m-1)}{(2n-1)(n+m)}}, \quad 1 < m < n$$

$$d_{nm} = \sqrt{(2n)(2n+1)(n+1)}, \quad m=1 \quad (\text{A.2-4})$$

$$d_{nm} = \sqrt{(n+m)(n-m+1)}, \quad 1 < m < n$$

and the following expression from the recursive formulas for the unnormalized Legendre functions

$$q = \sqrt{1-z^2} \quad (\text{A.2-5})$$

The recursive evaluation of  $\bar{P}_{nm}(z)$ ,  $\bar{P}'_{nm}(z)$ ,  $\bar{P}''_{nm}(z)$  is performed in the new subroutine LEGNDS using the relations below [1, 8]. The recursive formulas for the normalized Legendre functions are

$$\bar{P}_{11}(z) = \sqrt{3} q, \quad \bar{P}_{21}(z) = \sqrt{15} q z, \quad \bar{P}_{22}(z) = \frac{1}{2} \sqrt{15} q^2 \quad (\text{A.2-6})$$

$$\bar{P}_{n1}(z) = a_{n1} z \bar{P}_{n-1,1}(z) + b_{n1} q P_{n-1}(z), \quad n > 2 \quad (\text{A.2-7})$$

$$\bar{P}_{nm}(z) = a_{nm} z \bar{P}_{n-1,m}(z) + b_{nm} q \bar{P}_{n-1,m-1}(z), \quad m = 2, \dots, n-1 \quad (\text{A.2-8})$$

$$\bar{P}_{nn}(z) = b_{nn} q \bar{P}_{n-1,n-1}(z) \quad (\text{A.2-9})$$

The recursive formulas for the first derivative of the Legendre functions with respect to the argument  $z$  (using unnormalized Legendre polynomials) are

$$\bar{P}'_{11}(z) = \frac{-z\sqrt{3}}{q}, \quad \bar{P}'_{21}(z) = \frac{\sqrt{15}}{q}(1-2z^2), \quad \bar{P}'_{22}(z) = -z\sqrt{15} \quad (\text{A.2-10})$$

$$\bar{P}'_{n1}(z) = \frac{1}{q^2} (z \bar{P}_{n1}(z) - d_{n1} q P_n(z)) \quad (\text{A.2-11})$$

$$\bar{P}'_{nm}(z) = \frac{1}{q^2} (m z \bar{P}_{nm}(z) - d_{nm} q \bar{P}_{n,m-1}(z)), \quad m = 2, \dots, n \quad (\text{A.2-12})$$

Lastly, the recursive formulas for the second derivative of the Legendre functions with respect to the argument  $z$  (using unnormalized Legendre polynomials) are

$$\bar{P}_{11}''(z) = -\frac{\sqrt{3}}{q^3}, \quad \bar{P}_{21}''(z) = \frac{z\sqrt{15}}{q^3}(2z^2 - 3), \quad \bar{P}_{22}''(z) = -\sqrt{15} \quad (\text{A.2-13})$$

$$\bar{P}_{n1}''(z) = \frac{1}{q^2} \left( \frac{(1+z^2)}{q^2} \bar{P}_{n1}(z) + z \bar{P}_{n1}'(z) \right) - d_{n1} \left( \frac{z}{q} P_n(z) + q P_n'(z) \right) \quad (\text{A.2-14})$$

$$\bar{P}_{nm}''(z) = \frac{1}{q^2} \left( \frac{\frac{m}{q^2}(1+z^2) \bar{P}_{nm}(z) + m z \bar{P}_{nm}'(z)}{-d_{nm} \left( \frac{z}{q} \bar{P}_{n,m-1}(z) + q \bar{P}_{n,m-1}'(z) \right)} \right), \quad m = 2, \dots, n \quad (\text{A.2-15})$$

The recursive evaluation of the above functions starts with  $n = 2$  for the gravity harmonic force evaluation, since the spherical harmonic expansions in PEP start at the second degree (assuming the center of mass of the central body coincides with the origin of coordinates).



## Appendix B

### List of Constants

Primary Constant [20]	Description	Value	Units
$M_s$	Mass of the sun	1	
$\sqrt{GM_s}$	Gaussian gravitational constant	0.01720209895	AU <sup>3/2</sup> /day
CT	Coordinate Time	A.1 + 32.15 <sup>s</sup> TAI+32.184 <sup>s</sup>	day
A.1, TAI	Atomic Time Seconds	9,192,631,770	oscillations of cesium

The A.1 and TAI atomic times are kept as the average of a number of cesium atomic clocks at the national time services (particularly at the U.S. Naval Observatory). UTC time runs at the A.1 and TAI rates, and presently differs from TAI by an integral number of seconds. As required (approximately once a year), there is an increase of one second (a UTC leap second) in TAI-UTC, to keep UTC within one second of UT1 time, defined by a formula in terms of sidereal time [23]. Given a UTC observation time, CT is computed for interpolating from ephemeris files, and UT1 time and earth wobble are computed from tables published by the International Earth Rotation Service (see Appendix C.2).

# LUNAR GRAVITATIONAL FIELD ESTIMATION AND SATELLITE ORBIT PREDICTION

Auxiliary Constant [23]	Description	Value	Units
AULTSC	Astronomical Unit in Light Seconds	499.004782	seconds/AU
c	Speed of light	299,792.458	km/sec
$\frac{M_s}{M_c}$	sun/(earth + moon) mass ratio	328,900.1	
$\frac{M_c}{M_l}$	(earth + moon)/moon mass ratio	82.301	
$GM_l$	Lunar gravitational constant (PEP uses AU <sup>3</sup> /day <sup>2</sup> )	4,902.79375	km <sup>3</sup> /sec <sup>2</sup>
$\rho_l$	Lunar mean equatorial radius	1,738	km
$P_l$	Lunar period	27.322	days
gal	Unit of Acceleration	1.0	cm/sec <sup>2</sup>

## Appendix C

# Inertial Coordinate Transformations

### C.1 Transformation Between Moon Fixed and Inertial Frames

The transformation between moon-fixed (selenographic) coordinates and the inertial integration frame coordinates (the mean equinox and equator of 1950.0) is required to evaluate gravity harmonic and mascon accelerations in the numerical integration of a lunar satellite's motion. Auxiliary software also uses this transformation to analyze integration output in the selenographic frame and to prepare numerical integration input. In Equation (3.2-2) for the transformation between coordinates fixed in the moon and the integration frame coordinates, the rotation matrix  $R$  can be expressed as [6]

$$R = UVP \quad (C.1-1)$$

where

- $P$  = Earth precession matrix transforming between integration frame coordinates and coordinates referred to the mean equinox and equator of date (50 arcseconds per year).
- $V$  = Transformation between coordinates referred to the mean equinox and equator of date and coordinates referred to the mean equinox and ecliptic of date (23.4° rotation).
- $U$  = Transformation between coordinates referred to the mean equinox and ecliptic of date and coordinates fixed in the moon along the nominal principal moment of inertia axes (360° per 27.2 days).

## LUNAR GRAVITATIONAL FIELD ESTIMATION AND SATELLITE ORBIT PREDICTION

PEP uses a Taylor series expansion to calculate the earth precession matrix (P) for speed during a numerical integration [7]. If  $\epsilon_0$  is the standard expression for the obliquity of the ecliptic [20, 23], the transformation matrix between mean equatorial and ecliptic coordinates of date is

$$V = \begin{bmatrix} 1 & 0 & 0 \\ 0 & \cos \epsilon_0 & \sin \epsilon_0 \\ 0 & -\sin \epsilon_0 & \cos \epsilon_0 \end{bmatrix} \quad (C.1-2)$$

Cassini's laws plus the physical libration of the moon determine the transformation between the mean equinox and ecliptic of date and selenographic coordinates (U). The following formulas are used within PEP to calculate this transformation matrix.

Letting

**M** = Mean longitude of the moon measured in the ecliptic from the mean equinox of date to the mean ascending node of the lunar orbit and then along the orbit (27.2° day period).

**Ω** = Longitude of the mean ascending node of the lunar orbit on the ecliptic measured from the mean equinox of date (18.6 year period).

**I** = Inclination of the lunar equator to the ecliptic (1.53889°).

**σ, ρ, τ** = Physical librations in node, inclination, and longitude.

Standard polynomial expressions are used for the angles M and Ω, as well as for the angles  $\ell$ ,  $\ell'$ , F, and D which are from Brown's lunar theory [23]. PEP uses the following trigonometric series for the physical librations [28]

$$\begin{aligned} \tau = & -12.9'' \sin \ell - 0.3'' \sin 2\ell + 65.2'' \sin \ell' + 9.7'' \sin (2f - 2\ell) \\ & + 1.4'' \sin (2F - 2D) + 2.5'' \sin (D - \ell) - 0.6'' \sin (2D - 2\ell + \ell') \\ & - 7.3'' \sin (2D - 2\ell) - 3.0'' \sin (2D - \ell) - 0.4'' \sin 2D \\ & + 7.6'' \sin \Omega \end{aligned} \quad (C.1-3)$$

$$\begin{aligned} \rho = & -106'' \cos \ell + 35'' \cos (2F - \ell) - 11'' \cos 2F \\ & - 3'' \cos (2F - 2D) - 2'' \cos (2D - \ell) \end{aligned} \quad (C.1-4)$$

### Appendix C: Inertial Coordinate Transformations

$$\begin{aligned} I(\tau - \sigma) = & 108'' \sin \ell - 35'' \sin (2F - \ell) + 11'' \sin 2F \\ & + 3'' \sin (2F - 2D) + 2'' \sin (2D - \ell) \end{aligned} \quad (C.1-5)$$

where  $I$  is measured in radians.

In terms of these angles, the Euler angles for the moon rotation are

$$\begin{aligned} \psi &= \Omega + \sigma \\ \theta &= I + \rho \\ \phi &= 180^\circ + (M - \Omega) + (\tau - \sigma) \end{aligned} \quad (C.1-6)$$

The transformation matrix between selenographic coordinates fixed in the moon and those referred to the mean equinox and ecliptic of date is then [6]

$$\begin{aligned} U_{11} &= -\sin \psi \cos \theta \sin \phi - \cos \psi \cos \phi \\ U_{12} &= \cos \psi \cos \theta \sin \phi + \sin \psi \cos \phi \\ U_{13} &= -\sin \theta \sin \phi \\ U_{21} &= -\sin \psi \cos \theta \cos \phi - \cos \psi \sin \phi \\ U_{22} &= \cos \psi \cos \theta \cos \phi - \sin \psi \sin \phi \\ U_{23} &= -\sin \theta \cos \phi \\ U_{31} &= -\sin \psi \sin \theta \\ U_{32} &= \cos \psi \sin \theta \\ U_{33} &= \cos \theta \end{aligned} \quad (C.1-7)$$

To check these transformations, the earth and sun's selenographic longitude and latitude were printed out for certain dates. These positions were obtained by transforming the vectors pointing from the moon to these objects with the transformation matrix Equation (C.1-1). This check verified that PEP's values agreed with the published values in the *Astronomical Almanac*, to the number of places published ( $0.001^\circ$  for the earth,  $0.01^\circ$  for the sun).

Since this transformation's moon-fixed axes are not exactly along the moon's principal moments of inertia axes, the  $C_{21}$ ,  $S_{21}$ , and  $S_{22}$  spherical harmonic coefficients cannot be assumed to be zero. If the rotation and orbit of the moon were estimated by fitting to lunar laser corner reflector data, these second degree harmonic coefficients could be set to zero. Simultaneously processing lunar laser data with lunar orbiter data could

## LUNAR GRAVITATIONAL FIELD ESTIMATION AND SATELLITE ORBIT PREDICTION

provide the best estimate of the remaining second degree harmonic coefficients, as well as third and perhaps fourth degree coefficients.

One auxiliary program (selenang), converts satellite osculating orbital angles in the selenographic coordinate frame to angles in the integration (1950.0) frame. These angles are input to PEP to specify a desired selenographic orbital orientation for numerical integrations. Within PEP, these initial osculating elliptic orbital elements are converted to Cartesian position and velocity initial conditions for the numerical integrations.

Another auxiliary program (selenelm) converts the numerical integration output to selenographic position and velocity and to selenographic osculating elliptic orbital elements as functions of time. The selenographic osculating elliptic orbital elements, the altitude above the lunar surface, and the subsatellite selenographic longitude and latitude can then be plotted over time.

### **C.2 Transformation Between Earth Fixed and Inertial Frames**

Since earth-fixed observing sites need to be transformed to the inertial frame to process observations, the transformation matrix between earth-fixed coordinates and the inertial integration frame referred to the mean equinox and equator of 1950.0 is also required. This rotation transformation matrix  $R$  can be expressed as [8]

$$R = W S N P \quad (C.2-1)$$

where

$P$  = Earth precession matrix transforming between integration frame coordinates and coordinates referred to the mean equinox and equator of date (50 arcseconds per year).

$N$  = Earth nutation matrix transforming between coordinates referred to the mean equinox and equator of date and coordinates referred to the true equinox and equator of date (20 arcseconds).

### Appendix C: Inertial Coordinate Transformations

- S** = Earth sidereal time matrix transforming between coordinates referred to the true equinox and equator of date and coordinates with z axis along the earth pole of rotation and x axis in the meridian of Greenwich through the rotation pole (360° per 23<sup>h</sup> 56<sup>m</sup> 4.09<sup>s</sup>).
- W** = Earth wobble matrix transforming between coordinates with z axis along the earth pole of rotation and x axis in the meridian of Greenwich and coordinates with z axis along the conventional international pole and x axis in the meridian of Greenwich through the conventional international pole (0.3 arcseconds).

Since PEP uses the IAU value of the precession constant [23] in the trigonometric angles for evaluating the precession matrix, **P**, numerical integration results in the 1950.0 reference frame are transformations of integration results in the IAU J2000.0 reference frame [23].

Since observations in PEP are a function of UTC time and there is a mathematical formula relating sidereal time to UT1 time [23], the relationship between UTC and UT1 time is needed to determine the sidereal time transformation matrix, **S**. PEP determines this relationship from values published by the International Earth Rotation Service (IERS) based on very long baseline interferometry and lunar and satellite laser ranging observations.

$$UT1 - UTC = (A.1 - UTC) - (A.1 - UT1) \quad (C.2-2)$$

The IERS also publishes wobble angles based on the above-mentioned observations which are used to compute the earth wobble transformation matrix, **W**. Exact values of these quantities were not required for this thesis' simulations.





## Appendix D

### Lunar Gravitational "Truth" Model

Table D-1: 5 X 5 Spherical Harmonic Coefficient Portion of Truth Model [12]

Harmonic	$\times 10^{-6}$	Harmonic	$\times 10^{-6}$
$J_2$	202.431	$\bar{S}_{21}$	-0.00
$\bar{C}_{21}$	-0.07	$\bar{S}_{22}$	0.03
$\bar{C}_{22}$	34.49		
$J_3$	8.8897	$\bar{S}_{31}$	6.63
$\bar{C}_{31}$	21.96	$\bar{S}_{32}$	4.76
$\bar{C}_{32}$	14.14	$\bar{S}_{33}$	-2.45
$\bar{C}_{33}$	15.87		
$J_4$	-11.73	$\bar{S}_{41}$	1.91
$\bar{C}_{41}$	-4.82	$\bar{S}_{42}$	-6.76
$\bar{C}_{42}$	-8.13	$\bar{S}_{43}$	-14.43
$\bar{C}_{43}$	0.48	$\bar{S}_{44}$	-0.55
$\bar{C}_{44}$	-3.50		
$J_5$	2.388	$\bar{S}_{51}$	-1.53
$\bar{C}_{51}$	-9.66	$\bar{S}_{52}$	-2.35
$\bar{C}_{52}$	3.71	$\bar{S}_{53}$	4.91
$\bar{C}_{53}$	-0.39	$\bar{S}_{54}$	-6.58
$\bar{C}_{54}$	0.56	$\bar{S}_{55}$	11.60
$\bar{C}_{55}$	-6.69		

# LUNAR GRAVITATIONAL FIELD ESTIMATION AND SATELLITE ORBIT PREDICTION

Table D-2: Lunar Near-Side Mascons at 1638 km Radius [47]

Mass ( $10^{-6}$ Lunar Mass)	East Longitude (degrees)	North Latitude (degrees)	Mass ( $10^{-6}$ Lunar Mass)	East Longitude (degrees)	North Latitude (degrees)
Sea of Serenity			Sea of Rains		
0.101	10.5	34.0	-0.597	342.0	48.0
2.437	17.5	34.0	0.467	328.5	40.5
2.453	10.5	28.0	5.329	337.5	40.5
3.316	17.5	28.0	5.218	346.5	40.5
3.774	24.5	28.0	1.252	328.5	34.0
0.371	8.25	22.5	1.628	335.5	34.0
2.628	13.75	22.5	3.586	342.5	34.0
3.628	19.25	22.5	1.752	349.5	34.0
1.681	24.75	22.5	-0.421	328.5	28.0
0.290	12.5	17.5	2.336	335.5	28.0
0.624	17.5	17.5	2.654	342.5	28.0
0.229	22.5	17.5	Seething Bay		
Sea of Crises			0.328	347.5	12.5
0.230	52.25	22.5	1.934	352.5	12.5
1.520	57.75	22.5	0.531	347.5	7.5
0.992	52.5	17.5	1.522	352.5	7.5
2.837	57.75	17.5	Sea of Moisture		
1.836	62.5	17.5	3.091	318.75	-22.5
1.183	57.5	17.5	2.726	325.25	-22.5
0.688	62.5	12.5	0.164	321.5	-28.0
Sea of Nectar			Smyth's Sea		
0.251	27.5	-12.5	0.622	87.5	2.5
1.394	32.5	-12.5	-0.172	82.5	-2.5
1.199	37.5	-12.5	0.873	87.5	-2.5
0.602	27.5	-17.5	0.739	92.5	-2.5
4.180	32.5	-17.5	0.352	87.5	-7.5
0.663	37.5	-17.5	0.691	92.5	-7.5

Appendix D: Lunar Gravitational 'Truth' Model

**Table D-3: Lunar Far-Side Mascons at 1638 km Radius**

<b>Mass (10<sup>-6</sup> Lunar Mass)</b>	<b>East Longitude (degrees)</b>	<b>North Latitude (degrees)</b>	<b>Mass (10<sup>-6</sup> Lunar Mass)</b>	<b>East Longitude (degrees)</b>	<b>North Latitude (degrees)</b>
<b>Difficult to Observe Mascon</b>			0.829	182.5	8.0
1.836	177.5	-8.0	1.504	180.0	8.0
2.367	180.0	-8.0	1.254	177.5	8.0
1.726	182.5	-8.0	0.615	183.75	5.0
1.357	176.75	-5.0	1.391	181.25	5.0
2.929	178.75	-5.0	1.613	178.75	5.0
2.265	181.25	-5.0	0.825	176.25	5.0
0.935	183.75	-5.0	2.125	185.0	0.0
1.323	175.0	0.0	4.737	182.5	0.0
2.682	177.5	0.0	7.712	180.0	0.0
<b>Balancing Mascon</b>			1.602	213.25	-50.5
4.151	212.0	-48.0	2.534	215.75	-50.5
7.212	214.5	-48.0	5.128	213.25	-45.5
2.817	217.0	-48.0	3.713	215.75	-45.5
<b>Final Point Masses</b>			1.11385	217.6253	-63.4005
4.85×10 <sup>-6</sup>	214.93	-49.06	2.1×10 <sup>-11</sup>	203.77	-43.54



## Appendix E

### Tables of Spherical Harmonic Coefficients

On the following pages are the tables containing the spherical harmonic coefficients for the models estimated in this thesis. Also included are the spherical harmonic coefficients from degree six through ten from Alex Konopliv's 50 x 50 spherical harmonic model estimated at the Jet Propulsion Laboratory. These coefficients were used in the fit of a 10 x 10 model to observations generated by a 10 x 10 truth model. The tesseral coefficients are normalized and the zonal coefficients are unnormalized to follow the convention used in PEP-D which was modified from the SAO's version to use normalized Legendre polynomials, but not normalized Legendre functions.

# LUNAR GRAVITATIONAL FIELD ESTIMATION AND SATELLITE ORBIT PREDICTION

Table E-1: Limb Mascon Fit Model Coefficients

Harmonic	$\times 10^{-6}$	Harmonic	$\times 10^{-6}$
J <sub>2</sub>	197.7368	J <sub>3</sub>	50.7687
J <sub>4</sub>	-31.9055	J <sub>5</sub>	-69.3894
J <sub>6</sub>	1.7549	J <sub>7</sub>	43.8035
J <sub>8</sub>	-10.1643		
C <sub>21</sub>	-12.7475	S <sub>21</sub>	1.5079
C <sub>22</sub>	27.1059	S <sub>22</sub>	0.2444
C <sub>31</sub>	24.0662	S <sub>31</sub>	4.0278
C <sub>32</sub>	28.6630	S <sub>32</sub>	-1.0723
C <sub>33</sub>	14.4920	S <sub>33</sub>	-3.2666
C <sub>41</sub>	23.9593	S <sub>41</sub>	-4.4657
C <sub>42</sub>	-8.9861	S <sub>42</sub>	-4.9991
C <sub>43</sub>	-12.4622	S <sub>43</sub>	-4.5046
C <sub>44</sub>	0.4030	S <sub>44</sub>	-1.5219
C <sub>51</sub>	-14.7946	S <sub>51</sub>	1.0878
C <sub>52</sub>	-23.7583	S <sub>52</sub>	10.2963
C <sub>53</sub>	4.8944	S <sub>53</sub>	4.2337
C <sub>54</sub>	10.1329	S <sub>54</sub>	-16.9327
C <sub>55</sub>	-7.8183	S <sub>55</sub>	13.3437
C <sub>61</sub>	-24.7054	S <sub>61</sub>	5.6856
C <sub>62</sub>	5.8578	S <sub>62</sub>	-2.0959
C <sub>63</sub>	18.9141	S <sub>63</sub>	-14.0732
C <sub>64</sub>	-6.4188	S <sub>64</sub>	1.8413
C <sub>65</sub>	-2.7320	S <sub>65</sub>	6.2106
C <sub>66</sub>	-0.1282	S <sub>66</sub>	-1.7523
C <sub>71</sub>	1.2154	S <sub>71</sub>	0.7781
C <sub>72</sub>	14.2798	S <sub>72</sub>	-7.2171
C <sub>73</sub>	-4.8109	S <sub>73</sub>	3.4451
C <sub>74</sub>	-8.6970	S <sub>74</sub>	9.1036
C <sub>75</sub>	-8.6970	S <sub>75</sub>	9.1036
C <sub>76</sub>	0.2179	S <sub>76</sub>	-0.5194
C <sub>77</sub>	0.0208	S <sub>77</sub>	0.0303
C <sub>81</sub>	7.8239	S <sub>81</sub>	-1.9813
C <sub>82</sub>	1.7894	S <sub>82</sub>	-0.5271
C <sub>83</sub>	-6.3293	S <sub>83</sub>	3.9422
C <sub>84</sub>	4.5862	S <sub>84</sub>	-1.1922
C <sub>85</sub>	2.3076	S <sub>85</sub>	-5.2013
C <sub>86</sub>	-1.6316	S <sub>86</sub>	2.5572
C <sub>87</sub>	0.3903	S <sub>87</sub>	0.3041
C <sub>88</sub>	0.7639	S <sub>88</sub>	0.0524

Note: All of the C<sub>nm</sub> and S<sub>nm</sub> terms are Normalized. The J<sub>n</sub> terms are Unnormalized.

# Appendix E: Tables of Spherical Harmonic Coefficients

Table E-2: Face Mascon Fit Model Coefficients

Harmonic	$\times 10^{-6}$	Harmonic	$\times 10^{-6}$
J <sub>2</sub>	212.9685	J <sub>3</sub>	-18.2734
J <sub>4</sub>	-17.2629	J <sub>5</sub>	56.7533
J <sub>6</sub>	6.8783	J <sub>7</sub>	-33.1132
J <sub>8</sub>	1.9000		
C <sub>21</sub>	10.1197	S <sub>21</sub>	3.3802
C <sub>22</sub>	35.1938	S <sub>22</sub>	2.7565
C <sub>31</sub>	20.1172	S <sub>31</sub>	8.9737
C <sub>32</sub>	0.1584	S <sub>32</sub>	5.8036
C <sub>33</sub>	19.8874	S <sub>33</sub>	-5.5137
C <sub>41</sub>	-25.7774	S <sub>41</sub>	3.4003
C <sub>42</sub>	-2.1818	S <sub>42</sub>	-11.9870
C <sub>43</sub>	14.6293	S <sub>43</sub>	-18.4118
C <sub>44</sub>	-4.5549	S <sub>44</sub>	3.9231
C <sub>51</sub>	-7.5438	S <sub>51</sub>	-0.8299
C <sub>52</sub>	24.1943	S <sub>52</sub>	-7.5913
C <sub>53</sub>	-8.1387	S <sub>53</sub>	12.9983
C <sub>54</sub>	-11.5970	S <sub>54</sub>	-0.2905
C <sub>55</sub>	-4.6557	S <sub>55</sub>	7.4909
C <sub>61</sub>	17.6456	S <sub>61</sub>	-3.3481
C <sub>62</sub>	-0.9812	S <sub>62</sub>	1.0038
C <sub>63</sub>	-16.1761	S <sub>63</sub>	7.6098
C <sub>64</sub>	4.9624	S <sub>64</sub>	-9.3866
C <sub>65</sub>	6.4501	S <sub>65</sub>	-4.1229
C <sub>66</sub>	-0.9473	S <sub>66</sub>	3.4506
C <sub>71</sub>	1.5589	S <sub>71</sub>	-3.8029
C <sub>72</sub>	-9.6129	S <sub>72</sub>	4.0109
C <sub>73</sub>	2.9190	S <sub>73</sub>	-4.8617
C <sub>74</sub>	10.2397	S <sub>74</sub>	-4.9557
C <sub>75</sub>	-3.1597	S <sub>75</sub>	7.1339
C <sub>76</sub>	-0.5898	S <sub>76</sub>	1.1869
C <sub>77</sub>	0.1187	S <sub>77</sub>	0.0073
C <sub>81</sub>	-6.5178	S <sub>81</sub>	-0.4581
C <sub>82</sub>	-2.6772	S <sub>82</sub>	1.4211
C <sub>83</sub>	3.3579	S <sub>83</sub>	-4.3328
C <sub>84</sub>	-0.5695	S <sub>84</sub>	4.2547
C <sub>85</sub>	-5.7318	S <sub>85</sub>	2.0067
C <sub>86</sub>	3.6244	S <sub>86</sub>	-5.2175
C <sub>87</sub>	-0.4581	S <sub>87</sub>	-0.4756
C <sub>88</sub>	1.5694	S <sub>88</sub>	0.0024

Note: All of the C<sub>nm</sub> and S<sub>nm</sub> terms are Normalized. The J<sub>n</sub> terms are Unnormalized.

# LUNAR GRAVITATIONAL FIELD ESTIMATION AND SATELLITE ORBIT PREDICTION

Table E-3: 8 X 8 Single Orbiter Earth-based Doppler Fit Model Coefficients

Harmonic	$\times 10^{-6}$	Harmonic	$\times 10^{-6}$
J <sub>2</sub>	181.1456	J <sub>3</sub>	59.8185
J <sub>4</sub>	-74.6007	J <sub>5</sub>	-132.1220
J <sub>6</sub>	133.1974	J <sub>7</sub>	79.6217
J <sub>8</sub>	-16.5125		
C <sub>21</sub>	20.7759	S <sub>21</sub>	48.2268
C <sub>22</sub>	98.9974	S <sub>22</sub>	63.8880
C <sub>31</sub>	52.1951	S <sub>31</sub>	20.3043
C <sub>32</sub>	15.7778	S <sub>32</sub>	-22.4302
C <sub>33</sub>	-52.7148	S <sub>33</sub>	-87.8210
C <sub>41</sub>	16.7472	S <sub>41</sub>	12.8355
C <sub>42</sub>	-101.0443	S <sub>42</sub>	-87.6400
C <sub>43</sub>	0.9710	S <sub>43</sub>	-53.3659
C <sub>44</sub>	79.4372	S <sub>44</sub>	62.3998
C <sub>51</sub>	-80.3231	S <sub>51</sub>	11.2542
C <sub>52</sub>	-6.9808	S <sub>52</sub>	-67.9849
C <sub>53</sub>	137.9127	S <sub>53</sub>	118.1211
C <sub>54</sub>	18.6358	S <sub>54</sub>	61.9093
C <sub>55</sub>	-80.5845	S <sub>55</sub>	-35.9216
C <sub>61</sub>	-41.8646	S <sub>61</sub>	-56.2582
C <sub>62</sub>	76.5292	S <sub>62</sub>	-9.1320
C <sub>63</sub>	0.9371	S <sub>63</sub>	76.6052
C <sub>64</sub>	-140.8093	S <sub>64</sub>	-115.2748
C <sub>65</sub>	-10.4542	S <sub>65</sub>	-46.8469
C <sub>66</sub>	43.5262	S <sub>66</sub>	24.5186
C <sub>71</sub>	44.0845	S <sub>71</sub>	-26.6661
C <sub>72</sub>	15.2502	S <sub>72</sub>	72.1269
C <sub>73</sub>	-63.0660	S <sub>73</sub>	4.2952
C <sub>74</sub>	10.4385	S <sub>74</sub>	-66.4744
C <sub>75</sub>	125.9903	S <sub>75</sub>	76.7319
C <sub>76</sub>	24.5612	S <sub>76</sub>	1.5036
C <sub>77</sub>	-8.5265	S <sub>77</sub>	-0.5739
C <sub>81</sub>	15.1214	S <sub>81</sub>	15.5307
C <sub>82</sub>	-30.5354	S <sub>82</sub>	28.4645
C <sub>83</sub>	-6.4764	S <sub>83</sub>	-50.2189
C <sub>84</sub>	33.7568	S <sub>84</sub>	42.2387
C <sub>85</sub>	-22.1201	S <sub>85</sub>	36.8057
C <sub>86</sub>	-68.3081	S <sub>86</sub>	-38.0350
C <sub>87</sub>	-5.5991	S <sub>87</sub>	3.3389
C <sub>88</sub>	20.2612	S <sub>88</sub>	-1.0150

Note: All of the C<sub>nm</sub> and S<sub>nm</sub> terms are Normalized. The J<sub>n</sub> terms are Unnormalized.



Appendix E: Tables of Spherical Harmonic Coefficients

**Table E-4: Additional Coefficients for the 10 X 10 Spherical Harmonic Expansion [27]**

Harmonic	$\times 10^{-6}$	Harmonic	$\times 10^{-6}$
J <sub>6</sub>	-4.2385	J <sub>7</sub>	-6.2390
J <sub>8</sub>	-2.5920	J <sub>9</sub>	-3.5975
J <sub>10</sub>	1.6589		
C <sub>61</sub>	1.9850	S <sub>61</sub>	-3.1813
C <sub>62</sub>	-4.0909	S <sub>62</sub>	-2.2826
C <sub>63</sub>	-2.8312	S <sub>63</sub>	-3.7963
C <sub>64</sub>	0.4618	S <sub>64</sub>	-3.5250
C <sub>65</sub>	1.0906	S <sub>65</sub>	-10.6099
C <sub>66</sub>	-5.3433	S <sub>66</sub>	6.3502
C <sub>71</sub>	7.2821	S <sub>71</sub>	-0.2472
C <sub>72</sub>	-1.2317	S <sub>72</sub>	2.7566
C <sub>73</sub>	0.2624	S <sub>73</sub>	2.2896
C <sub>74</sub>	-1.4476	S <sub>74</sub>	1.2214
C <sub>75</sub>	-0.6229	S <sub>75</sub>	-0.0130
C <sub>76</sub>	-0.8231	S <sub>76</sub>	1.3403
C <sub>77</sub>	-0.9763	S <sub>77</sub>	-0.5650
C <sub>81</sub>	-0.8685	S <sub>81</sub>	1.5051
C <sub>82</sub>	3.2189	S <sub>82</sub>	-2.0279
C <sub>83</sub>	-1.3720	S <sub>83</sub>	0.6560
C <sub>84</sub>	3.9047	S <sub>84</sub>	-0.7301
C <sub>85</sub>	-0.8683	S <sub>85</sub>	2.2454
C <sub>86</sub>	-0.8443	S <sub>86</sub>	-0.3390
C <sub>87</sub>	-1.5132	S <sub>87</sub>	3.1351
C <sub>88</sub>	-3.3194	S <sub>88</sub>	1.0685
C <sub>91</sub>	1.6794	S <sub>91</sub>	-0.0034
C <sub>92</sub>	2.7144	S <sub>92</sub>	-1.5708
C <sub>93</sub>	-2.0677	S <sub>93</sub>	2.0466
C <sub>94</sub>	-2.3575	S <sub>94</sub>	-1.3200
C <sub>95</sub>	-1.9722	S <sub>95</sub>	-2.8712
C <sub>96</sub>	-2.1046	S <sub>96</sub>	-2.3382
C <sub>97</sub>	-4.8133	S <sub>97</sub>	-2.6997
C <sub>98</sub>	-1.7042	S <sub>98</sub>	-2.1130
C <sub>99</sub>	-0.2704	S <sub>99</sub>	-3.4853
C <sub>10,1</sub>	0.3840	S <sub>10,1</sub>	-0.4607
C <sub>10,2</sub>	-0.1513	S <sub>10,2</sub>	0.0074
C <sub>10,3</sub>	0.1089	S <sub>10,3</sub>	0.7679
C <sub>10,4</sub>	-3.4765	S <sub>10,4</sub>	1.8562
C <sub>10,5</sub>	1.5547	S <sub>10,5</sub>	-0.1451
C <sub>10,6</sub>	0.0773	S <sub>10,6</sub>	-3.1297
C <sub>10,7</sub>	-4.6092	S <sub>10,7</sub>	-1.6688
C <sub>10,8</sub>	-2.5105	S <sub>10,8</sub>	-6.1743
C <sub>10,9</sub>	-3.9610	S <sub>10,9</sub>	0.0054
C <sub>10,10</sub>	0.6457	S <sub>10,10</sub>	2.4016

Note: All of the C<sub>nm</sub> and S<sub>nm</sub> terms are Normalized. The J<sub>n</sub> terms are Unnormalized.

# LUNAR GRAVITATIONAL FIELD ESTIMATION AND SATELLITE ORBIT PREDICTION

Table E-5: 8 X 8 Dual Orbiter Bent Pipe Doppler Fit Model Coefficients

Harmonic	$\times 10^{-6}$	Harmonic	$\times 10^{-6}$
J <sub>2</sub>	222.3087	J <sub>3</sub>	25.5174
J <sub>4</sub>	16.0116	J <sub>5</sub>	-26.9111
J <sub>6</sub>	-3.5341	J <sub>7</sub>	9.0723
J <sub>8</sub>	6.2438		
C <sub>21</sub>	20.9141	S <sub>21</sub>	4.4952
C <sub>22</sub>	62.9024	S <sub>22</sub>	11.3343
C <sub>31</sub>	23.0231	S <sub>31</sub>	3.6164
C <sub>32</sub>	17.3213	S <sub>32</sub>	4.4079
C <sub>33</sub>	5.0245	S <sub>33</sub>	-9.5957
C <sub>41</sub>	-7.0910	S <sub>41</sub>	1.0255
C <sub>42</sub>	-15.3037	S <sub>42</sub>	-12.3986
C <sub>43</sub>	7.7601	S <sub>43</sub>	-23.7569
C <sub>44</sub>	5.5738	S <sub>44</sub>	2.7198
C <sub>51</sub>	-16.6822	S <sub>51</sub>	-8.5788
C <sub>52</sub>	3.6949	S <sub>52</sub>	-9.5117
C <sub>53</sub>	13.4951	S <sub>53</sub>	-0.4007
C <sub>54</sub>	7.6961	S <sub>54</sub>	-0.8922
C <sub>55</sub>	-28.7475	S <sub>55</sub>	-3.3561
C <sub>61</sub>	-5.4094	S <sub>61</sub>	8.9587
C <sub>62</sub>	6.5187	S <sub>62</sub>	-4.8860
C <sub>63</sub>	3.4694	S <sub>63</sub>	8.8267
C <sub>64</sub>	-7.7898	S <sub>64</sub>	-14.6763
C <sub>65</sub>	-4.3649	S <sub>65</sub>	-14.2858
C <sub>66</sub>	6.4123	S <sub>66</sub>	-2.2788
C <sub>71</sub>	6.2918	S <sub>71</sub>	5.7153
C <sub>72</sub>	-0.1180	S <sub>72</sub>	-1.3007
C <sub>73</sub>	-4.5694	S <sub>73</sub>	6.7590
C <sub>74</sub>	2.2257	S <sub>74</sub>	-13.5958
C <sub>75</sub>	30.7662	S <sub>75</sub>	22.8105
C <sub>76</sub>	5.6403	S <sub>76</sub>	-1.1883
C <sub>77</sub>	-5.6869	S <sub>77</sub>	0.9170
C <sub>81</sub>	3.4853	S <sub>81</sub>	-6.5550
C <sub>82</sub>	-2.9015	S <sub>82</sub>	11.7741
C <sub>83</sub>	-7.9046	S <sub>83</sub>	4.2567
C <sub>84</sub>	-0.2085	S <sub>84</sub>	16.0011
C <sub>85</sub>	-2.3673	S <sub>85</sub>	9.2307
C <sub>86</sub>	-9.0060	S <sub>86</sub>	1.2082
C <sub>87</sub>	-0.3801	S <sub>87</sub>	-1.1762
C <sub>88</sub>	1.0937	S <sub>88</sub>	-1.2396

Note: All of the C<sub>nm</sub> and S<sub>nm</sub> terms are Normalized. The J<sub>n</sub> terms are Unnormalized.

## References

1. Abramowitz, Milton and Irene A. Stegun, *Handbook of Mathematical Functions*, Dover Publications, New York, 1964.
2. Abshire, James B., "Lunar Scout Laser Ranging System for Lunar Gravity Measurements," Goddard Space Flight Center Briefing, October 10, 1991.
3. Akim, E.L. and Z.P. Vlasova, "Research on the Moon's Gravitational Field from Measurement Data on the Trajectories of Soviet Artificial Satellites of the Moon," *Kosmicheskie Issledovaniya*, Vol 21, No. 4, pp. 499-511, July-August 1983. Translated by Plenum Publishing Corporation, 1984.
4. Ananda, Mohan P., "Satellite Perturbed by a Lens Shaped Mass Concentration," *Celestial Mechanics*, Vol. 12, pp. 495-511, December 1975.
5. Ananda, Mohan P., "Lunar Gravity: A Mass Point Model," *Journal of Geophysical Research*, Vol 82 No 20, pp. 3049-3064, July 10, 1977.
6. Ash, Michael E., "Generation of Planetary Ephemerides on an Electronic Computer," Technical Report 391, M.I.T. Lincoln Laboratory, Lexington, MA, 2 June 1965.
7. Ash, Michael E., "Generation of the Lunar Ephemeris on an Electronic Computer," Technical Report 400, M.I.T. Lincoln Laboratory, Lexington, MA, 24 August 1965.
8. Ash, Michael E., "Determination of Earth Satellite Orbits," Technical Note 1972-5, M.I.T. Lincoln Laboratory, Lexington, MA, 19 April 1972.
9. Ash, Michael E., "Doubly Averaged Effect of the Moon and Sun on a High Altitude Earth Satellite Orbit," *Celestial Mechanics*, Vol. 14, pp. 209-238, 1976.
10. Battin, Richard H., *An Introduction to the Mathematics and Methods of Astrodynamics*, AIAA Education Series, New York, 1987.

## LUNAR GRAVITATIONAL FIELD ESTIMATION AND SATELLITE ORBIT PREDICTION

11. Bierman, Gerald J., *Factorization Methods for Discrete Sequential Estimation*, Academic Press, New York and London, 1977.
12. Bills, Bruce G., and Alfred J. Ferrari, "A Harmonic Analysis of Lunar Gravity," *Journal of Geophysical Research*, Vol. 85 No. 82, pp. 1013-1025, February 10, 1980.
13. Cappallo, Roger J., "The Rotation of the Moon," Doctoral Dissertation, M.I.T., Cambridge, MA, February 1980.
14. Comfort, Gary C., "The Determination of Gravitational Potential from the Measurement of Relative Velocity Between Satellites," T-545, C.S. Draper Laboratory, Cambridge, MA, June 1971.
15. Conte, S.D., *Elementary Numerical Analysis*, McGraw-Hill, Inc., New York, 1965.
16. Cook, Richard A., A.B. Sergeevsky, E.A. Belbruno, and T.H. Sweetser, "Return to the Moon: The Lunar Observer Mission," *AIAA Astrodynamics Conference*, Paper AIAA-90-2888, August 1990.
17. Counselman, C.C. III, H.F. Hinteregger, R.W. King, and I.I. Shapiro, "Lunar Baselines and Libration from Differential VLBI Observations of ALSEPS," *The Moon*, Vol. 8, D. Reidel Publishing, Dordrecht Holland, pp. 484-489, 1973.
18. Croopnick, Steven R. "Orbit Prediction in the Presence of Gravitational Anomalies," T-536, C.S. Draper Laboratory, Cambridge, MA, June 1970.
19. Ferrari, Alfred J., "Lunar Gravity: A Harmonic Analysis," *Journal of Geophysical Research*, Vol 82 No 20, pp. 3065-3084, July 10, 1977.
20. *Explanatory Supplement to the Ephemeris*, H. M. Nautical Almanac Office, London, 1961.
21. Gelb, Arthur (ed.), *Applied Optimal Estimation*, The M.I.T. Press, Cambridge, MA, 1974.
22. Heiskanen, Weikko A. and Helmut Moritz, *Physical Geodesy*, Freeman and Company, San Francisco, 1967.
23. "Improved IAU System," Supplement to the *Astronomical Almanac* 1984, U.S. Government Printing Office, 1983.

## REFERENCES

24. Kaula, William M., *Theory of Satellite Geodesy*, Blaisdell Publishing Co., Waltham, MA, 1966.
25. Konopliv, Alex, "Simulations of Lunar Gravity Field Determination for Lunar Observer," *AAS/AIAA Astrodynamics Specialist Conference*, August 1991.
26. Konopliv, Alex, "Preliminary Lunar Gravity Field Results with Lunar Orbiter I through V Data," Jet Propulsion Laboratory Briefing, November 3, 1992.
27. Konopliv, Alex, private communication, December 1992.
28. Koziel, K., "Libration of the Moon," *Physics and Astronomy of the Moon*, Academic Press, New York and London, pp. 31-45, 1962.
29. Lorell, J., J.D. Anderson, and W.L. Sjogren, "Characteristics and Format of the Tracking Data to be Obtained by the NASA Deep Space Instrumentation Facility for Lunar Orbiter," Technical Memorandum No. 33-230, Jet Propulsion Laboratory, California Institute of Technology, Pasadena, CA, June 15, 1965.
30. Lorell, J., "Lunar Orbiter Gravity Analysis," *Moon*, Vol. 1, D. Reidel Publishing, Dordrecht Holland, pp. 190-231, 1970.
31. Maybeck, Peter S., *Stochastic Models, Estimation, and Control*, Vol. 2, Academic Press, New York and London, 1982.
32. Michael, William H. Jr. and W. Thomas Blackshear, "Recent Results on the Mass, Gravitational Field and Moments of Inertia of the Moon," *The Moon*, Vol. 3, D. Reidel Publishing, Dordrecht Holland, pp. 388-402, 1972.
33. Michael, William H. Jr., W. Thomas Blackshear, and J.P. Gapcynski, "Results on the Mass and the Gravitational Potential of the Moon as Determined from Dynamics of Lunar Satellites," *Dynamics of Lunar Satellites*, Springer-Verlag, New York and Berlin, pp. 42-56, 1969.
34. Moulton, Forest R., *An Introduction to Celestial Mechanics*, The MacMillan Company, New York, 1914.
35. Muller, Paul M. and William L. Sjogren, "Mascons: Lunar Mass Concentrations," *Science*, Vol. 161, pp. 680-684, August 16, 1968.
36. Muller, Paul M. and William L. Sjogren, "Information from Deep-Space Tracking," *Physics Today*, Vol. 22, pp. 46-52, July 1969.

## **LUNAR GRAVITATIONAL FIELD ESTIMATION AND SATELLITE ORBIT PREDICTION**

37. Nicolaides, John D., Mark M. Macomber, and William M. Kaula, "Terrestrial, Lunar, and Planetary Applications of Navigation and Geodetic Satellites," *Advances in Space Science and Technology*, Vol. 5, Academic, New York, 1963.
38. Nordsieck, A., "On Numerical Integration of Ordinary Differential Equations," *Math. of Comp.* 16, 1962, pp. 22-49.
39. Parker, G., and K. Nock, "Lunar Observer: Scouting for a Moon Base," *Space Programs and Technologies Conference*, Paper AIAA-90-3781-CP, Huntsville AL, September 1990.
40. Ridenoure, Rex W. (ed.), "Lunar Observer - A Comprehensive Orbital Survey of The Moon: Mission and System Definition Summary," JPL D-8607, Jet Propulsion Laboratory, California Institute of Technology, Pasadena CA, April 15, 1991.
41. Sagitov, M.U., B. Bodri, V.S. Nazarenko, and Kh G. Tadzhdinov. *Lunar Gravimetry*, Harcourt Brace Jovanovich, New York, 1986.
42. Skeen, Matthew E., *Maximum Likelihood Estimation of Fractional Brownian Motion and Markov Noise Parameters*, T-1109, C.S. Draper Laboratory, Cambridge, MA, December 1991.
43. Stimson, George W., *Introduction to Airborne Radar*, Hughes Aircraft Company, El Segundo, CA, 1983.
44. Torge, Wolfgang, *Gravimetry*, Walter de Gruyter, New York, 1989.
45. Wertz, James R. and Wiley J. Larson (eds.), *Space Mission Analysis and Design*, Kluwer Academic Publishers, Boston, 1991.
46. Wilks, Samuel, S., *Mathematical Statistics*, John Wiley & Sons, Inc., New York, 1962.
47. Wong, L., G.Buechler, W.Downs, W.Sjogren, P.Muller, and P.Gottlieb, "A Surface Layer Representation of the Lunar Gravitational Field," *Journal of Geophysical Research*, Vol. 76, pp. 6220-6236, September 10, 1971.